SIMULATION OF THERMAL-MECHANICAL BEHAVIOR DURING INITIAL SOLIDIFICATION OF STEEL

BY

JON-CHRISTOPHER THAYNE PARKMAN

B.A., Lake Forest College, 1995

THESIS

Submitted in partial fulfillment of the requirements
for the degree of Master of Science in Mechanical Engineering
in the Graduate College of the
University of Illinois at Urbana-Champaign, 2000

Urbana, Illinois

Abstract

With the ever present increase in computer technology, computational modeling of mechanical behavior in a solidifying body is of great potential to the understanding of materials processing. In the continuous casting of steel it is known that the initial solidification of the shell has an important influence on the final quality of the entire slab. A two-dimensional transient stepwise-coupled finite element model has been developed which is capable of simulating a transverse section of the slab as it moves down the mold. The model is applied to various initial solidification problems to try and understand the thermal and mechanical behavior of steel for various carbon contents. The high temperature creep and plasticity of the steel is incorporated through unified constitutive equations which define the inelastic strain rates as a function of temperature, composition, accumulated plastic strain and the stress state. The unified constitutive equations are based on measurements and apply for both austenite and ferrite. They are reasonably able to account for the enhanced creep rate in δ-ferrite. The model has been successfully verified with analytical solutions and experimental data. The model is used to predict the evolution of temperature, stress, and shape of 10 mm diameter molten steel droplets solidifying against a water-cooled copper chill plate. The model can also assist in the design of mold shape (taper) to match shrinkage and provide insight into the formation of longitudinal surface cracks through the use of fracture criteria and stress analysis.

Table of Contents

List of Tables

List of Figures

Nomenclature

A	Area
[C]	Capacitance matrix
[D]	3x3 elasticity matrix for plane stress
[D']	4x4 elasticity matrix for generalized-plane strain
C_P	Heat capacity
E	Elastic modulus
F_P	Ferrostatic pressure
$\Delta F_x, \Delta F_y, \Delta F_z$	Force in the x,y and z direction
{F}	Total Force vector
$\{\Delta F_{\varepsilon T}\}$	Incremental thermal force vector
$\{\Delta F_{\varepsilon P}\}$	Incremental plastic strain force vector
$\{F_{el}\}$	Total elastic strain force vector
$\{F_{fp}\}$	Total ferrostatic pressure force vector
fsolid	Fraction of solid
g	Gravitational acceleration
H	Enthalpy
h	Heat transfer coefficient
[K]	Conductance matrix
$[K_\sigma]$	Stiffness matrix for plane strain
$[K''_\sigma]$	Stiffness matrix for generalized plane strain
k	Thermal conductivity of steel
L	Characteristic length
L_f	Latent heat of fusion
Pe	Peclet number
{Q}	Heat flow vector
Re	Reynold's number
T	Temperature
{T}	Nodal temperature
$\dot{T}$	Time derivative of temperature
T_{sol}	Solidus temperature
T_{liq}	Liquidus temperature
TLE	Thermal linear expansion

t	Current time (since start of simulation)
Δt	Time step
V_x, V_y, V_z	Velocity components
x	X coordinate
y	Y coordinate
z	Z coordinate
α	Ferrite phase
δ	Delta phase
$\boldsymbol{\varepsilon}$	Total strain vector
$\dot{\boldsymbol{\varepsilon}}$	Total strain rate vector
$\{\varepsilon\}$	Total strain components
$\{\dot{\varepsilon}\}$	Components of total strain rate
$\{\dot{\varepsilon}^T\}$	Components of total thermal strain rate
$\{\dot{\varepsilon}^P\}$	Components of total plastic strain rate
$\{\Delta\varepsilon\}$	Incremental total strain
$\{\Delta\varepsilon^P\}$	Incremental plastic strain
$\{\Delta\varepsilon\}$	Incremental total strain
γ	Gamma phase
ρ	Mass density
σ_{SB}	Stefan-Boltzmann constant
σ_Y	Yield stress
$\boldsymbol{\sigma}$	Total stress vector
$\{\sigma\}$	Total stress components
$\{\Delta\sigma\}$	Incremental stress components
$\bar{\sigma}$	Von Misses effective stress of $\{\sigma\}$

1 Introduction

Most of the steel made today is processed through continuous casting, because of its advantages in productivity, quality and thermal efficiency. A schematic of the continuous casting process is displayed in Figure 1.1. Despite the quality of the continuous cast steel, there is a significant amount of work trying to reduce the amount of surface defects. When molten metal impacts a chilled surface, it suddenly experiences many complex phenomena including rapid cooling, solidification, and thermal distortion. These phenomena control the heat transfer, microstructure, segregation, stresses, and deformation, which determine the quality of the cast product. This behavior is critical to many different metals solidification processes including continuous casting. Most of the surface defects in continuous cast steel initiate during the early stages of solidification at the meniscus in the mold. These include surface depressions, longitudinal and transverse surface cracks. Although a body of empirical knowledge and theory exists, the exact mechanisms for many of these problems are still unclear. With the use of today's computer hardware and computational techniques, numerical modeling of the initial solidification stage offers the ability to gain insight into how such defects originate.

It is well known that the contact resistance at the interface between the solidifying metal and the chill controls heat transfer during initial solidification. The amount of contact resistance is affected greatly by the size of the gap, which is controlled by the shape of the solidifying metal surface. Although many previous experimental and heat transfer modeling studies have been done, very little previous attention has been given to predicting the amount of thermal distortion during the initial stages of solidification. As the solidifying steel cools and distorts, it may lift away slightly from the substrate, creating gaps which could greatly lower the heat transfer. Changes in heat transfer could lead to surface cracks, shell breakouts, severe meniscus marks, and surface depressions the effect of which maybe sensitive to small changes in composition.

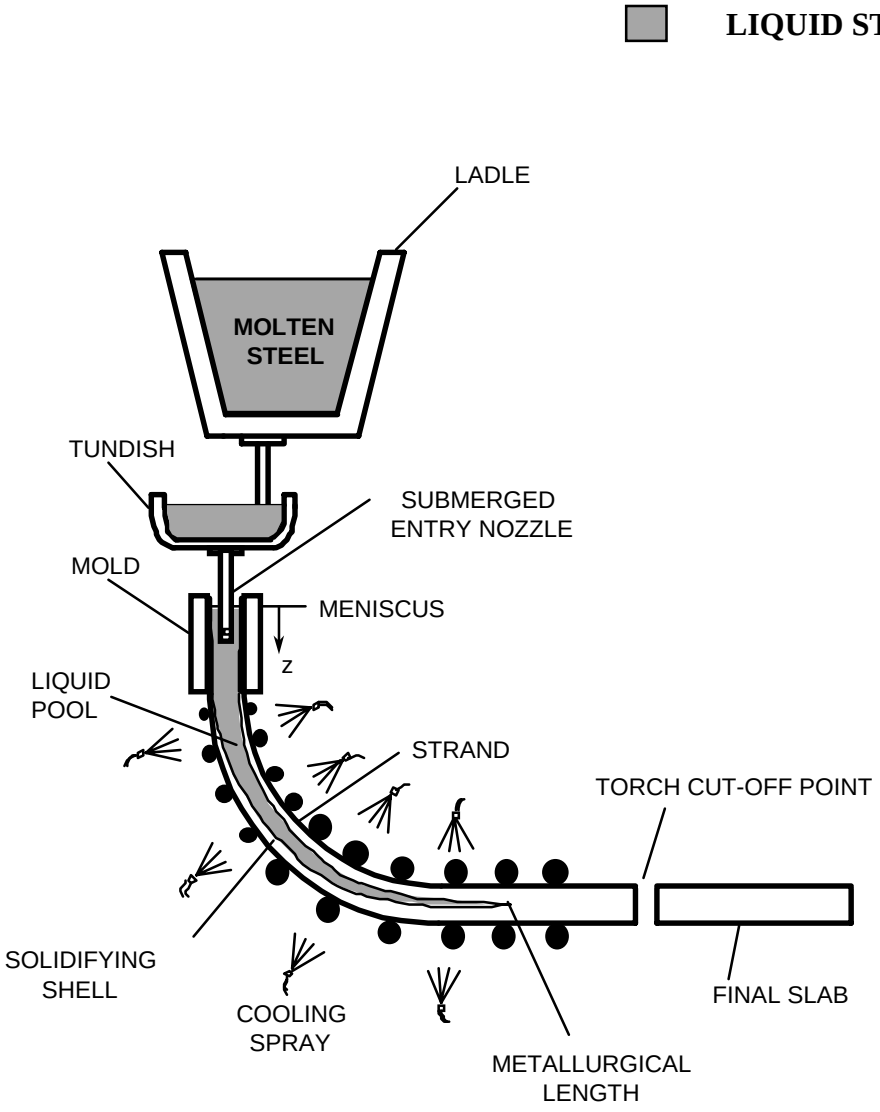

Figure 1.1. Schematic overview of the continuous casting process

2 Objectives

The primary objective of this work is to gain more understanding of the initial stages of solidification through the use of numerical simulation. This includes the investigation of the thermal-mechanical behavior of steel during the initial stages of solidification, focusing on the mechanisms of surface deformation and crack formation. The simulation will be done through the use of CON2D [1], an efficient finite-element model which utilizes new computational procedures for stress modeling of processes with solidification, emphasizing the numerical implementation of unified constitutive models for fixed-grid mechanical analysis of solidification. Previous work completed by Zhu [2] and Moitra [3] led to the development of the model. A detailed description of the model will be provided in Chapter 4, discussing both the thermal and mechanical model formulations. A significant amount of work has also been completed to validate the accuracy of the model. The validation is completed using an analytical solution of a well-established test problem, as well as comparing model predictions to various experimental solidification results. The model is used to predict the final deformation of 10 mm diameter molten steel droplets solidifying against a water-cooled copper chill plate as well as trying to predict the force required to tear apart a solidifying steel shell. The model is then applied to shell shrinkage calculations utilizing simple one-dimensional mesh domains. The results provide insight to stress / strain evolution including the prediction of cracks and ideal taper calculations.

3 Previous Work

Several studies have been made to investigate how cracks form during continuous casting of steel. It is well known that the middle carbon or "peritectic" steels containing 0.1 - 0.2 wt.%C are more prone to depressions and longitudinal surface cracks during casting than other grades [4-6]. This was initially attributed to an inherent lower ductility of these grades. However, H. Suzuki et al. [7] performed isothermal tensile tests on in-situ melted and resolidified samples that showed ductility decreases slowly but steadily with increasing carbon and residual alloy content. There was no special embrittlement problem with middle carbon steels. Embrittlement was attributed to the drop in solidus temperature caused by micro segregation of the alloying elements. Alternatively, Ye et al. [8] found that middle carbon steel shells have a 2% macroscopic strain to failure, which is greater than other steels. Thus, the increased surface cracking tendency of middle carbon steels is now attributed to the peritectic reaction, and the phase transformation contraction from delta-ferrite to austenite [9]. Clearly some confusion remains regarding the reasons for the peritectic steel behavior.

Many researchers have noted the important effect of steel carbon content on the surface roughness of continuously cast steel. Surface roughness, as indicated by the depth of depressions and oscillation marks, is also greatest for "peritectic" steel with about 0.1%C [10-14]. Ultra-low carbon steel has high roughness also [14]. Higher surface roughness is detrimental as it lowers the heat transfer and decreases the uniformity. This leads to non-uniform solidification [13] and a greater tendency for cracks and other quality problems in these grades. Thus, accurate predictions of stress and strain during initial solidification, which include the effects of both temperature and composition of the steel properties are needed.

The complicated nature of the continuous casting process makes it extremely difficult to conduct experiments within the mold to understand the initial solidification behavior of the solidifying

shell. To gain an understanding of the initial solidification process, researchers look toward more controlled solidification experiments and mathematical modeling of solidification. Together, experiments and modeling allow researchers to gain insight into both the initial heat transfer and initial stress state of the solidifying metal.

3.1 Experiments of Initial Solidification

A large amount of experimental research has been conducted on initial solidification phenomena of small molten droplets impacting a chilled substrate. Several researchers have conducted droplet experiments along with subsequent mathematical modeling of the solidification process in one form or another. Bennett and Poulikakos [15] conducted splat quench solidification experiments of molten lead, as well as developing a two-dimensional heat conduction model. Trapaga et al. [16] performed similar research on molten copper droplets and Wang and Matthys [17-19] on aluminum and nickel droplets. A limited amount of work however, exists on experiments involving the solidification of molten steel droplets.

Dong et al. [20] conducted experiments of molten steel droplets impacting a chilled surface. This work focused on the impact that carbon content and mold material, would have on determining the final droplet shape. The amount of deformation experienced by the droplets could then be used to provide insight to the thermal deformation behavior of initially solidified steel shells. Todoroki et al. [21] conducted experiments on iron and nickel droplets impacting cooled substrates. This work focused on determining the heat transfer coefficient during the first 0.5 seconds of solidification, to gain an understanding of the factors controlling strip cast surface quality.

Several other more complicated experiments focused on the initial solidification of steel have also been completed. Mizukami et al. [22], conducted experiments where a sapphire glass was

dipped into molten steel. These experiments focused on measuring the cooling curves of various grades of steel as they solidified. Other experiments have been established using "Submerged Split Chill Tensile" (SSCT) tests to simulate the strength of an initially solidified steel shell [23, 24]. SSCT experiments allow researchers to gain detailed knowledge of high temperature strength properties as a function of steel composition. Such knowledge can then be applied to predict crack formation and maximum casting speeds.

3.2 Models of Initial Solidification

The use of mathematical modeling has helped researchers to understand the underlying principles of various materials processing operations for over a decade. The continuous casting process is no exception, as it has been subjected to more mathematical models than any other process [25]. A review of such models has been composed by Thomas [26] on slab casting and by Samarasekera [27], on billet casting.

To accurately predict initial shell distortion and crack formation requires a robust mathematical model incorporating fluid flow, heat transfer, solidification and viscoplastic stress analysis. A majority of the work in modeling the thermal-mechanical solidification process is based on the use of the finite-element method. This is due to the flexibility of this method to efficiently handle arbitrary geometric shapes, as well as complex material properties and other nonlinear phenomena.

While many finite-element thermal stress models have focused on bulging below the mold, [28-32], these types of models have also played an important role in understanding the solidification behavior of the slab in the mold as well [33-42]. Such models have been applied to examine various aspects of the continuous casting process, including mold design [41, 42], off-corner depressions [39, 41, 42], and cracks [33, 35, 38, 43, 44].

Many previous solidification stress analysis models have also oversimplified several other important aspects, including the effects of mesh refinement, combined creep and plasticity, temperature dependency of the elastic modulus, phase transformations, fluid flow and two-dimensional stress state [3, 25]. The need for such a model capable of accurately handling such phenomena led to the development of CON2D [1-3]. Originally developed to model a horizontal two-dimensional slice as it moves down the mold at the casting speed, the robustness of CON2D makes it ideal for modeling initial solidification phenomena. CON2D is able to properly model the initial stress development of solidified steel due to accurate unified viscoplastic constitutive equations [45, 46] implemented into the model by Zhu [2]. Thus, the model is capable of accurately predicting the stress / strain relationship of steels between 900°C and the liquidus as will be discussed in Chapter 5.

4 Model Description

This chapter presents a description of the model, CON2D [1] developed by Zhu [2] and Moitra [3]. The model is a transient two-dimensional, step-wise coupled thermo-elasto-viscoplastic fixed-grid finite-element model, coded in FORTRAN, developed to understand the behavior of the solidifying shell within the mold region of a continuous slab casting machine. The model incorporates an efficient scheme for finite-element implementation of unified elastic-viscoplastic constitutive equations. The model has been developed to follow the thermal and mechanical behavior of a section of the solidifying steel shell, as it moves down the mold at the casting speed.

4.1 Heat Transfer and Solidification Model

The first task in the mechanical modeling of thermal processes, such as solidification, is an accurate prediction of the transient temperature history, which controls the thermal strains responsible for most of the stresses. The partial differential equation governing heat transfer in the continuous cast strand is given by the three-dimensional energy equation:

$$\frac{\partial}{\partial x}\left(k_x \frac{\partial T}{\partial x}\right)+\frac{\partial}{\partial y}\left(k_y \frac{\partial T}{\partial y}\right)+\frac{\partial}{\partial z}\left(k_z \frac{\partial T}{\partial x}\right)=\rho \cdot C_P\left(\frac{\partial T}{\partial t}+V_x \frac{\partial T}{\partial x}+V_y \frac{\partial T}{\partial y}+V_z \frac{\partial T}{\partial z}\right) \qquad (4.1)$$

For the solid portion of the domain the V_x and V_y terms are zero, and for the liquid portion of the domain their effects are taken into account through enhanced conductivity of the liquid or through boundary conditions [3] and thus can be neglected. The transport of superheat in the liquid is also implemented through separate boundary conditions. The importance of heat conduction in the casting direction (z-dimension) is negligible compared to the heat carried by the strand movement. This follows from the Peclet number (Pe), which is equal to about 500, for typical values used in the applications of this model. (ρ = 7400 Kg/m^3 , C_P = 670 J/Kg/K, V_z = 0.0166 m/min and L = 0.2 m)

$$Pe = \frac{\rho C_p V_z L}{k} \tag{4.2}$$

Thus, conduction in the vertical direction (z) can be neglected. Also, because the model adopts a Lagrangian frame of reference fixed on the strand moving at the constant velocity (same as casting speed) in the z-direction, equation (4.1) reduces to:

$$\frac{\partial}{\partial x}(k_x \frac{\partial T}{\partial x}) + \frac{\partial}{\partial y}(k_y \frac{\partial T}{\partial y}) = \rho C_p \frac{\partial T}{\partial t} \tag{4.3}$$

Applying the standard Galerkin finite-element formulation to the governing two-dimensional transient heat transfer equation (4.3) results in the following matrix relation:

$$[K]\{T\} + [C]\{\dot{T}\} = \{Q\} \tag{4.4}$$

where [K] is the conductance matrix, [C] is the capacitance matrix including the effects of solidification, and {Q} is the heat generation vector which is zero for this work. Terms in the 3x3 square [K] and [C] matrices were evaluated exactly using the standard consistent formulation [47]. The latent heat of solidification is incorporated into equation (4.4) through an effective specific heat in [C], which is evaluated using the spatial averaging technique suggested by Lemmon [48].

$$C_{p_{eff}} = \sqrt{\left(\frac{\partial H}{\partial x}\right)^2 + \left(\frac{\partial H}{\partial y}\right)^2 \Big/ \left(\frac{\partial T}{\partial x}\right)^2 + \left(\frac{\partial T}{\partial y}\right)^2} \tag{4.5}$$

Here, H(T) is the temperature-dependent enthalpy function for the steel alloy, that includes the latent heat of solidification, and is defined in terms of nodal values and element shape functions in the same manner as temperature.

The model utilizes the DuPont [49] three-level time-stepping technique, which utilizes results of two previous time steps to approximate the temperature {T} and the time derivative of temperature $\{\dot{T}\}$ as,

$$\{\dot{T}\} = \left(\frac{T_{t+\Delta t} - T_t}{\Delta t}\right) \tag{4.6a}$$

$$\{T\} = \frac{1}{4}(3T_{t+\Delta t} + T_{t-\Delta t}) \qquad (4.6b)$$

where $\{T_{t+\Delta t}\}$ are the unknown temperatures, for which the current equations are being solved, $\{T_t\}$ are the temperatures at the last time step, and $\{T_{t-\Delta t}\}$ are the temperatures at the time step before $\{T_t\}$.

Equations (4.6a) and (4.6b) are substituted into equation (4.4) and rearranged to obtain the finite-element form as:

$$\left[\frac{3}{4}[K] + \frac{[C]}{\Delta t}\right]\{T_{t+\Delta t}\} = \{Q\} - \frac{1}{4}[K]T_{t+\Delta t} + \frac{[C]}{\Delta t}\{T_t\} \qquad (4.7)$$

The material properties such as [K] and [C] are evaluated based on the temperature at time t. Equation (4.7) is solved at each time step for the unknown temperatures $\{T_{t-\Delta t}\}$ using the standard Choleski decomposition solution routine [50]. A fixed Lagrangian grid of 3-node, constant temperature-gradient triangular elements is employed to solve equation (4.7) in the finite-element domain.

4.2 Mechanical Model Formulation

Stresses arising during solidification are highly dependent on the temperature differences in the shell, the loading history and time-dependent creep. Thus, the mechanical model tracks displacements, strains, stresses, and forces as they evolve incrementally through time. Starting with stress-free liquid at the meniscus, (ε^e set at zero for $T=T_{sol}$) the model calculates the evolution of stresses, strains and displacements, within the same domain as the heat transfer model. This allows for the interpolation of the thermal loads into the stress model. The heat transfer uses 3-node triangular elements, while the stress model uses the same nodes connected into 6-node triangular elements.

By assuming small strains, small displacements and small rotation, the total strain rate tensor $\dot{\boldsymbol{\varepsilon}}$ can be decomposed into components consisting of elastic, thermal, inelastic and the flow strain rate tensors:

$$\dot{\boldsymbol{\varepsilon}}^{e} = \dot{\boldsymbol{\varepsilon}} - \dot{\boldsymbol{\varepsilon}}^{T} + \dot{\boldsymbol{\varepsilon}}^{P} + \dot{\boldsymbol{\varepsilon}}^{f} \tag{4.8}$$

where $\dot{\boldsymbol{\varepsilon}}^{e}$ is the elastic strain rate tensor, $\dot{\boldsymbol{\varepsilon}}^{T}$ is the thermal strain rate tensor, (incorporating volume changes from both temperature changes and solid-state phase transformations), $\dot{\boldsymbol{\varepsilon}}^{P}$ is the inelastic strain rate tensor, (incorporating both plastic and creep strain), and $\dot{\boldsymbol{\varepsilon}}^{f}$ is the pseudo flow strain rate tensor (incorporating the volume changes due to fluid flow of the liquid phase).

The stress tensor $\boldsymbol{\sigma}$ is obtained from the generalized form of Hooke's law,

$$\boldsymbol{\sigma} = \mathbf{D} : \boldsymbol{\varepsilon}^{e} \tag{4.9}$$

in which **D** is a fourth-order isotropic elastic tensor with components:

$$D_{ijkl}(T) = \lambda(T)\delta_{ij}\delta_{kl} + \mu(T)(\delta_{ik}\delta_{jl} + \delta_{il}\delta_{jk}) \tag{4.10}$$

where $\lambda(T)$ and $\mu(T)$ are temperature-dependent Lamé constants and δ_{ij} are components of the Kronecker delta, δ. Differentiating equation (4.9) yields the corresponding rate form of the constitutive relation written as:

$$\dot{\boldsymbol{\sigma}} = \mathbf{D}:(\dot{\boldsymbol{\varepsilon}}^{e}) + \dot{T}\frac{\partial \mathbf{D}}{\partial T}:\dot{\boldsymbol{\varepsilon}}^{e} \tag{4.11}$$

In the second term of the above equation, the changes in the elastic tensor caused by temperature variation are seen to contribute to the stress rate. Although this term is neglected (set to zero), the most significant portion is due to the solid / liquid transformation, which is handled in the model in a different manner to be discussed later.

The above equations describe the general three-dimensional framework for modeling the mechanical behavior of systems with temperature and rate-dependent material behavior. The

current model simulates a two-dimensional slice through a typical casting process. In two dimensions, the rate form of equation (4.9), or Hooke's law, in matrix notation is

$$\{\dot{\sigma}\} = [D]\{\dot{\varepsilon}^e\} \tag{4.12}$$

$$[D] = \frac{E(T)}{(1+\nu)(1-2\nu)} \begin{bmatrix} 1-\nu & \nu & 0 & \nu \\ \nu & 1-\nu & 0 & \nu \\ 0 & 0 & \frac{(1-2\nu)}{2} & 0 \\ \nu & \nu & 0 & 1-\nu \end{bmatrix} \tag{4.13}$$

$$\{\dot{\sigma}\} = \{\dot{\sigma}_x, \dot{\sigma}_y, \dot{\sigma}_{xy}, \dot{\sigma}_z\}^T \tag{4.14}$$

$$\{\dot{\varepsilon}^e\} = \{\dot{\varepsilon}^e_x, \dot{\varepsilon}^e_y, \dot{\varepsilon}^e_{xy}, \dot{\varepsilon}^e_z\}^T \tag{4.15}$$

Four different two-dimensional assumptions including plane-stress, plane-strain, generalized-plane-strain and plane-deformation conditions have all been implemented into CON2D [1]. When modeling a 2D slice through a typical casting, the best approximation is usually generalized plane strain, which allows translation of the 2D plane section [3].

The basic governing differential equations for the 2D generalized plane strain model are the mechanical equilibrium equations:

$$\frac{\partial \dot{\sigma}_x}{\partial x} + \frac{\partial \dot{\tau}_{xy}}{\partial y} = \dot{F}_x \tag{4.16a}$$

$$\frac{\partial \dot{\tau}_{xy}}{\partial x} + \frac{\partial \dot{\sigma}_y}{\partial y} = \dot{F}_y \tag{4.16b}$$

$$\int \dot{\sigma}_z dA = \dot{F}_z \tag{4.16c}$$

$$\int x\dot{\sigma}_z dA = \dot{M}_x = 0 \tag{4.16d}$$

$$\int y\dot{\sigma}_z dA = \dot{M}_y = 0 \tag{4.16e}$$

which relate the stress rates to external force rates, and the compatibility equations, which relate total strain rates to displacement rates:

$$\dot{\varepsilon}_x = \frac{\partial \dot{u}_x}{\partial x} \tag{4.17}$$

$$\dot{\varepsilon}_y = \frac{\partial \dot{u}_y}{\partial y} \tag{4.18}$$

$$\dot{\varepsilon}_{xy} = \frac{1}{2}\left(\frac{\partial \dot{u}_y}{\partial x} + \frac{\partial \dot{u}_x}{\partial y} \right) \tag{4.19}$$

$$\varepsilon_z = a + bx + cy \tag{4.20}$$

Generalized-plane-strain, assumes strain in the z-direction is constant (ε_z=a) over the entire simulation domain. For the current applications to continuous casting, and 2D solidification, the two-fold symmetry assumptions make the terms (b=c=0), which prevents any rotation of the plane and makes equations (4.16d) and (4.16e) vanish. Hence, a constant value for the ε_z strain over the entire domain needs to be solved during each time step. The current model solves for the ε_z strain at once, by adding one extra node to the finite-element mesh, because it has been found to be more efficient than iterating for the z-strain [3].

Applying the Galerkin finite-element formulation to the equilibrium equations (4.16), along with the strain displacement equations (4.17 - 4.20) and stress-strain equations (4.12) results in a set of simultaneous equations:

$$[K'_\sigma]\{\delta\} = \{\Delta F_{\varepsilon T}\} + \{\Delta F_{\varepsilon P}\} + \{F_{fp}\} + \{F_{el}\} \tag{4.21}$$

to be solved at each time step. In the above relation $\{\delta\}$ contains the incremental in-plane displacements and the incremental out-of-plane strain. The loads then arise from the thermal strains, $\{\Delta F_{\varepsilon T}\}$, the inelastic strains, $\{\Delta F_{\varepsilon P}\}$, ferrostatic pressure and mold interactions,$\{F_{fp}\}$, and a correction term from the elastic strain accumulated up to the previous time step. It is apparent to note that thermal and plastic loads are based on incremental strains where the ferrostatic

pressure and residual loads are based on total formulation. A detailed formulation of the terms of the stiffness matrix for generalized plane strain $[K'_{\sigma}]$, are described in Appendix B of Moitra [3].

4.2.1 Elastic Strain

Elastic strain is caused solely by elastic strain, related through the elastic modulus and Poison's ratio, as shown by equations (4.12 - 4.15). The temperature dependent elastic modulus data is discussed in Section 4.4.5.

4.2.2 Thermal Strain

Thermal strains arise from volume changes caused by both temperature and differences and phase changes (including both solidification and solid state transformations). They are calculated from the temperatures determined in the heat transfer analysis, {T}, and the thermal linear expansion (TLE) of the material.

$$\varepsilon^{T} = (TLE(T) - TLE(T_0)) \tag{4.22}$$

The thermal strain rate $\dot{\varepsilon}^{T}$, during time interval [t, t+Δt] is taken in a backward-difference form of thermal strain as:

$$\dot{\varepsilon}^{T} = \frac{[TLE(T_{t+\Delta t}) - TLE(T_t)]}{\Delta t} \tag{4.23}$$

$$\dot{\boldsymbol{\varepsilon}}^{T} = \dot{\varepsilon}^{T}\{1,1,0,1\}^{T} \tag{4.24}$$

By storing the contraction information directly into the state function TLE, strains due to both phase changes and temperature changes will be incorporated. The formulation of the TLE state function is discussed in Section 4.3.4.

4.2.3 Flow Strain

The flow or pseudo strain is the amount of strain that takes place in the liquid domain of the model. The model assumes that when liquid is present, fluid flow will occur to exactly match the shrinkage. Elements are treated as liquid when any node in the element is above the specified coherency temperature (set to solidus). Liquid elements are set to have no elastic strain, and consequently develop no stress. This also assures that the liquid elements will solidify stress free. The difference between the total strain and thermal strain in liquid elements is made up by the flow strain. By accounting for the flow strain, the model is able to balance the total strain into each of its components. In the model the accumulation of flow strain is only summarized for convenience purposes, as it is not used for any model calculations. This method allows easy tracking of various fracture criteria. For example, a large flow strain when the solid fraction is high indicates high cracking potential. Fracture criteria details and results are discussed more in Chapter 6. The tracking of flow strain is also needed for future macro segregation calculations.

4.2.4 Inelastic Strain

Inelastic strain includes strain in the solid arising from both creep and plastic yielding. At high temperatures, important to stress development during solidification, the inelastic strain is dominated by creep, which is very sensitive to strain rate. Creep is significant even during tensile test and cannot be distinguished from plastic strain. Thus, "unified" constitutive models have been developed to treat inelastic strain as a single function, whose instantaneous rate of change, $\dot{\boldsymbol{\varepsilon}}^{P}$, depends on the current stress, temperature, structure, and rate of phase transformation.

Through assuming associated plastic flow, the inelastic strain rate $\dot{\boldsymbol{\varepsilon}}^{P}$, is given by the Prandtl-Reuss relations [51]:

$$\dot{\boldsymbol{\varepsilon}}^{P} = \sqrt{\frac{3}{2}}\dot{\bar{\varepsilon}}^{P}\mathbf{N} \tag{4.25}$$

This approach ignores spatial anisotropy due to the inherent directional properties of crystals and their orientations. This assumption becomes more critical when the modeling scale is on the same order of grain size. Hence this work is good for macroscopic behavior relative to the grain column.

In equation (4.22) above, **N** represents the unit direction tensor of the inelastic strain rate, which is defined as

$$\mathbf{N} = \sqrt{\frac{3}{2}}\frac{\boldsymbol{\sigma}'}{\bar{\sigma}} \tag{4.26}$$

Here the deviatoric stress tensor $\boldsymbol{\sigma}'$, the Von Mises effective stress $\bar{\sigma}$, and the equivalent inelastic strain $\bar{\varepsilon}^{P}$ are defined by:

$$\boldsymbol{\sigma}' = \boldsymbol{\sigma} - \frac{1}{3}\mathrm{tr}(\boldsymbol{\sigma})\boldsymbol{\delta} \tag{4.27}$$

$$\bar{\sigma} = \sqrt{\frac{3}{2}\boldsymbol{\sigma}'\cdot\boldsymbol{\sigma}'} \tag{4.28}$$

$$\bar{\varepsilon}^{P} = \sqrt{\frac{2}{3}\boldsymbol{\varepsilon}^{P}\cdot\boldsymbol{\varepsilon}^{P}} \tag{4.29}$$

respectively. The equivalent inelastic strain rate is a function of the current effective stress and the structure parameter

$$\dot{\bar{\varepsilon}}^{P} = f(\bar{\sigma},\ s) \tag{4.30}$$

in which s represents a scalar structure parameter or "internal variable." The evolution equation of s takes the form

$$\dot{s} = g(\bar{\sigma},\ s) \tag{4.31}$$

The single-internal-variable unified constitutive model is used to describe the equivalent inelastic strain rate, which represents both time-dependent creep and time-independent plasticity. This

approach is natural because creep strain is significant during tensile tests at high temperature and cannot be distinguished from plastic strain. The current model employs the equivalent inelastic strain $\bar{\varepsilon}_P$ as the single structure parameter s in a rate-dependent constitutive equation. Various constitutive relations follow this approach [46, 52-55].

Equations (4.27) and (4.28) generally are strongly nonlinear ordinary differential equations and may be mathematically "stiff" in some regions. Hence special attention is required in their numerical integration. During solidification and other phase changes, the structure parameter may suddenly change, according to the changes in microstructure. When changes occur, the structure variable should be reset to an appropriate initial value for the new phase. Thus, for a strain-hardening viscoplastic constitutive model, inelastic strain accumulated in the old phase (e.g., liquid phase) should not contribute directly to material behavior in the new phase range (e.g., solid phase). With this type of treatment, completely fictitious material behavior may be involved for computational convenience in the liquid-phase region without necessarily creating inaccuracy in another [2].

Knowing the state variables (σ, s) at time t, these variables are determined at time $t+\Delta t$ through integration of the evolution equations (4.18) and (4.28). Thermal strain rate is known from prior analysis. Zhu showed that of several time integration schemes the best was found to be an operator-splitting technique, which alternates between implicit and explicit forms of total strain rate and inelastic strain rate during integration. Glowinski and Talle [56] used this scheme to integrate a viscoplastic model without hardening effects. The following section discusses how the model algorithm numerically integrates the constitutive equations over the time step.

4.2.5 Time-Integration Scheme for Implementation of Unified Temperature-Dependent Elastic-Viscoplastic Constitutive Models

Transient finite-element analysis involving rate-dependent nonlinear material behavior is performed in a discrete sequence of time increments using a time-marching method starting form given initial conditions. In a time-integration procedure, the rate-dependent constitutive model is transformed into a rate-independent algebraic formula in terms of the state variables stress, strain, inelastic strain and internal structure at the end of the time increment. Such a formula is called an algorithmic constitutive model, to distinguish it from the rate form of the constitutive model. Thus, besides the data that are known at the beginning of the time increment, the stress with respect to the strain increment also depends on the time-integration scheme and the related forms of inelastic strain rate. Numerical calculations on both the global level and the local level are usually involved in the large-scale computation with the material non-linearity described by this kind of algorithmic constitutive model [2].

Several robust and efficient numerical techniques have been implemented into finite-element calculations of unified, isotropic, temperature-dependent elastic-viscoplastic models. The model currently utilizes the alternating implicit-explicit scheme based on the operator-splitting technique implemented by Zhu [2]. This method involves transforming the tensor-algorithm constitutive models for isotropic materials into two scalar equations to solve at each spatial integration point. Zhu [2] then showed using the bounded Newton method to solve for the unknowns (the stress magnitude and the inelastic strain magnitude) was the most robust, accurate and efficient method. This time integration scheme is similar to that of one utilized by Lush et al. [57].

In the first or "local" step, stress and inelastic strain rate are estimated through implicit time integration at each material point, given the total strain rate at time t from the previous time step:

$$\hat{\boldsymbol{\sigma}}_{t+\Delta t} = \mathbf{D}_{t+\Delta t}:[\boldsymbol{\varepsilon}_t - \boldsymbol{\varepsilon}_t^T - \boldsymbol{\varepsilon}_t^P + (\dot{\boldsymbol{\varepsilon}}_t - \dot{\boldsymbol{\varepsilon}}_{t+\Delta t}^T - \hat{\dot{\boldsymbol{\varepsilon}}}_{t+\Delta t}^P)\Delta t] \tag{4.32}$$

In the second half-step, the global system of equations is solved for stress and total strain through implicit spatial integration using the finite-element method, based on explicit time integration using the inelastic strain rate from the first step:

$$\boldsymbol{\sigma}_{t+\Delta t} = \mathbf{D}_{t+\Delta t}:[\boldsymbol{\varepsilon}_t - \boldsymbol{\varepsilon}_t^T - \boldsymbol{\varepsilon}_t^P + (\dot{\boldsymbol{\varepsilon}}_t - \dot{\boldsymbol{\varepsilon}}_{t+\Delta t}^T - \hat{\dot{\boldsymbol{\varepsilon}}}_{t+\Delta t}^P)\Delta t] \tag{4.33}$$

For the above equations, ˆ represents intermediate, estimated terms. By substituting the above equations with equations (4.25 - 4.30), the terms can be rewritten as:

$$\hat{\boldsymbol{\sigma}}_{t+\Delta t} = \mathbf{D}_{t+\Delta t}:[\boldsymbol{\varepsilon}_t - \boldsymbol{\varepsilon}_t^T - \boldsymbol{\varepsilon}_t^P + (\dot{\boldsymbol{\varepsilon}}_t - \dot{\boldsymbol{\varepsilon}}_{t+\Delta t}^T - \sqrt{\tfrac{3}{2}}\, f(\hat{\bar{\sigma}}_{t+\Delta t},\, \hat{\bar{\varepsilon}}_{t+\Delta t}^P,\, T)\hat{\mathbf{N}}_{t+\Delta t})\Delta t] \tag{4.34}$$

$$\hat{\bar{\varepsilon}}_{t+\Delta t}^P = \bar{\varepsilon}_t^P + f(\hat{\bar{\sigma}}_{t+\Delta t},\, \hat{\bar{\varepsilon}}_{t+\Delta t}^P,\, T)\Delta t \tag{4.35}$$

$$\boldsymbol{\sigma}_{t+\Delta t} = \mathbf{D}_{t+\Delta t}:[\boldsymbol{\varepsilon}_t - \boldsymbol{\varepsilon}_t^T - \boldsymbol{\varepsilon}_t^P + (\dot{\boldsymbol{\varepsilon}}_{t+\Delta t} - \dot{\boldsymbol{\varepsilon}}_{t+\Delta t}^T - \sqrt{\tfrac{3}{2}}\, f(\hat{\bar{\sigma}}_{t+\Delta t},\, \hat{\bar{\varepsilon}}_{t+\Delta t}^P,\, T)\hat{\mathbf{N}}_{t+\Delta t})\Delta t] \tag{4.36}$$

In the first step, total strain rates based on the known incremental displacement field calculated in the previous time step are used to update the current stress and inelastic strain at each material point. Equations (4.34 - 4.35) and (4.25 - 4.30) thus constitute a system of nonlinear equations with 15 unknowns (two tensors and three scalars) to find at every material point of a three-dimensional analysis.

In the second step, the inelastic strain rate is assumed to equal the estimate in the first step. Thus, equation (4.36) can be regarded as a simple elastic constitutive equation with an initial strain or initial stress. The current total strain rate is found by solving the elastic constitutive equation and the system equilibrium equations using a global numerical method for spatial integration which in this work, was the finite-element method [2].

It should also be noted that $\hat{\boldsymbol{\sigma}}_{t+\Delta t}$, used to calculate the increment inelastic strain in the second step of the algorithm, does not satisfy the finite-element equilibrium equations at either time $t+\Delta t$ or time t.

Defining the estimated incremental strain as $\Delta\hat{\varepsilon}$, equations (4.34 - 4.36) are written as

$$\boldsymbol{\sigma}_{t+\Delta t} = \mathbf{D}_{t+\Delta t}:[\boldsymbol{\varepsilon}_t - \boldsymbol{\varepsilon}_t^T - \boldsymbol{\varepsilon}_t^P + \Delta\hat{\varepsilon} - \dot{\boldsymbol{\varepsilon}}_{t+\Delta t}^T \Delta t - \sqrt{\tfrac{3}{2}}\, f(\bar{\sigma}_{t+\Delta t},\, \bar{\varepsilon}_{t+\Delta t}^P,\, T)\hat{\mathbf{N}}_{t+\Delta t}\Delta t] \tag{4.37}$$

$$\bar{\varepsilon}_{t+\Delta t}^P = \bar{\varepsilon}_t^P + f(\bar{\sigma}_{t+\Delta t},\, \bar{\varepsilon}_{t+\Delta t}^P,\, T)\Delta t \tag{4.38}$$

For brevity, the intermediate stress and the inelastic strain corresponding to the estimated incremental strain $\Delta\hat{\varepsilon}$ are simply expressed as $\boldsymbol{\sigma}_{t+\Delta t}$, $\boldsymbol{\varepsilon}_{t+\Delta t}^P$ for this section. Equations (4.37) and (4.38) constitute a system of nonlinear equations with 14 scalar unknowns (two tensors and two scalars) in a three dimensional analysis. For the present model these equations are transformed into two unknown equations following a method similar to that of Lush [2, 57].

Substituting equation (4.10) into equation (4.37) produces

$$\boldsymbol{\sigma}_{t+\Delta t} = \sigma_{t+\Delta t}^* - \sqrt{6}\,\mu_{t+\Delta t} f(\bar{\sigma}_{t+\Delta t},\, \bar{\varepsilon}_{t+\Delta t}^P,\, T)\mathbf{N}_{t+\Delta t}\Delta t \tag{4.39}$$

where,

$$\sigma_{t+\Delta t}^* = \mathbf{D}_{t+\Delta t}:[\boldsymbol{\varepsilon}_t - \boldsymbol{\varepsilon}_t^T - \boldsymbol{\varepsilon}_t^P + \Delta\hat{\varepsilon} - \dot{\boldsymbol{\varepsilon}}_{t+\Delta t}^T \Delta t] \tag{4.40}$$

By taking the deviatoric part of equation (4.39) and substituting $\sigma'_{t+\Delta t} = \sqrt{\tfrac{2}{3}}\bar{\sigma}_{t+\Delta t}\mathbf{N}_{t+\Delta t}$, one finds

$$\sigma_{t+\Delta t}^{*'} = (\sqrt{\tfrac{2}{3}}\bar{\sigma}_{t+\Delta t} + \sqrt{6}\,\mu_{t+\Delta t} f(\bar{\sigma}_{t+\Delta t},\, \bar{\varepsilon}_{t+\Delta t}^P,\, T)\Delta t)\mathbf{N}_{t+\Delta t} \tag{4.41}$$

which means that $\mathbf{N}_{t+\Delta t}$ and $\sigma_{t+\Delta t}^{*'}$ have the same direction. Thus,

$$\mathbf{N}_{t+\Delta t} = \sqrt{\tfrac{3}{2}}\,\frac{\sigma_{t+\Delta t}^{*'}}{\bar{\sigma}_{t+\Delta t}^*} \tag{4.42}$$

and

$$\sigma'_{t+\Delta t} = \bar{\sigma}_{t+\Delta t}\,\frac{\sigma_{t+\Delta t}^{*'}}{\bar{\sigma}_{t+\Delta t}^*} \tag{4.43}$$

Combining equations (4.41) and (4.43) produces

$$\bar{\sigma}_{t+\Delta t} = \bar{\sigma}_{t+\Delta t}^* - 3\mu_{t+\Delta t} f(\bar{\sigma}_{t+\Delta t},\, \bar{\varepsilon}_{t+\Delta t}^P,\, T)\Delta t \tag{4.44}$$

Equations (4.44) and (4.38) form a pair of nonlinear scalar equations with two unknowns $\bar{\sigma}_{t+\Delta t}$, and $\bar{\varepsilon}^{P}_{t+\Delta t}$.

The problem in solving for $\bar{\sigma}_{t+\Delta t}$, and $\bar{\varepsilon}^{P}_{t+\Delta t}$ is very similar to a uniaxial problem with prescribed strain rate which might be integrated by the implicit backward-Euler scheme. Hence, a solution strategy must be developed to solve for these nonlinear equations. Zhu [2] shows that the bounded Newton-Raphson method best accomplishes this in order to overcome convergence and efficiency problems associated with other methods. The detail of which the bounded Newton-Raphson method is implemented into the model is described in Section 3.4.4 of Zhu [2].

One issue of the algorithm not described by Zhu [2] has to do with how the directions of $\bar{\sigma}$ and $\bar{\varepsilon}^{P}$ are computed. This becomes of particular importance under complex loading conditions. Under such conditions it is very important to properly supply the directions of stress, inelastic strain and inelastic strain rate to the constitutive equations. Therefore, the direction of $\bar{\sigma}$ is determined by the direction of the component (σ_x, σ_y, or σ_z) with the greatest absolute value. Similarly the same method is used to determine the direction of effective inelastic strain. The direction of $\bar{\varepsilon}^{P}$ is determined by the direction of the greatest absolute value of either (ε_x, ε_y, or ε_z). Care then has to be taken to ensure the directions of both $\bar{\sigma}$ and $\bar{\varepsilon}^{P}$, are properly accounted for when trying to solve equation (4.44) with the bounded Newton-Raphson method.

The previous discussed techniques allow the model to incorporate isotopic temperature-dependent elastic-viscoplastic constitutive equations. Several different types of constitutive equations have been implemented into the model. The present work utilizes two such constitutive equations, which have been incorporated into the model. These equations are discussed in more detail in Chapter 5.

4.2.6 Treatment of Liquid Elements

The present model uses a "fixed grid" approach in which the model domain contains both liquid and solid. Hence special treatment of the liquid must be taken to avoid generating unnecessary stresses in this region. This is accomplished by reducing the elastic modulus E by several orders of magnitude as temperature increases from the solidus to the liquidus temperature. The bulk modulus K and Lamé constant μ are related to elastic modulus and Poisson ratio ν by:

$$K = \frac{E}{1 - 2\nu} \tag{4.45}$$

$$\mu = \frac{E}{2(1 + \nu)} \tag{4.46}$$

This treatment means the liquid is easily deformed (small μ) and compressible (small K). Thus any mechanical influence of the liquid on the solid is avoided. Therefore, any effects of ferrostatic pressure must be applied as an internal constraint condition to the appropriated nodes near the solid / liquid interface [25].

With this implementation the elastic strain and inelastic strains at temperatures above the coherency temperature (set to solidus) are set to zero. This is accomplished with the use of flags set up in the program. This procedure assures that the elements solidify stress free. However, the thermal strain in the liquid is not zeroed out as it is used for calculations in tracking flow strain. Thus, only thermal and flow strain are present in the liquid region and are used for tracking purposes only.

4.2.7 Treatment of Shell / Mold Contact Using Gap Elements

To model the proper mechanical behavior between the shell and mold contact, further mechanical boundary conditions need to be used. One of the most difficult tasks is to properly account for the restraining effect of the mold on the thin shell, which is bulging due to creep

deformation driven by the ferrostatic pressure. In the present model, the penetration of the shell into the mold is prevented by the use of "spring elements" along the surface. This is accomplished by tracking the size of the gap between the mold and the shell. The magnitude of the gap is based on the best available estimate of the surface node displacement perpendicular to the mold wall. For most cases this is determined by u_x for the narrow face and u_y for the wide face. Nodes with a negative gap exceeding the allowable limit of δ (1.0×10^{-6} m for present work) are considered to have penetrated the mold. The normal displacement of these nodes is then fixed to a new position by the next time step. Fixing each nodal displacement is accomplished approximately by adding a "spring element" to pull that node towards its intended destination. Implementation of the "spring elements" into the model is described further on page 46 of Moitra [3].

4.3 Thermal-Mechanical Property Data

One of the main aspects for a successful model is accurate material property data. Therefore, careful selections were made for the property data used in these simulations. Most of the work performed in this paper has been on plain-carbon steel, using property data for from Harste [58].

4.3.1 Phase Composition

The accuracy of the model depends greatly on the ability to accurately predict the phase composition of the steel based on temperature and carbon content. Figure 4.1 shows the equilibrium phase diagram used in the model. The property data for the model is based on work by Harste and Jablonka [58, 59]. Figure 4.2 shows a more detailed region of the peritectic region important to this work. The method by which the phase diagram is implemented into the model allows for variation, as nonequilibrium phase diagrams are planned for future work.

4.3.2 Thermal Conductivity

The temperature-dependent thermal conductivity function used in the model is shown in Figure 4.3, for various carbon contents [58].

4.3.3 Enthalpy

The enthalpy H, which represents the total heat content is displayed as a function of temperature for various plain carbon steels in Figure 4.4 [58].

4.3.4 Thermal Linear Expansion

The thermal linear expansion (TLE) function used in the model is found from the temperature-dependent mass density. In mixed phase regions, TLE is found from a weighted average using the TLE curves for each of the individual phases present, based on their volume fractions. TLE is calculated by the following equations:

$$\rho_{tot} = \%\alpha \cdot \rho_{\alpha} + \%\partial \cdot \rho_{\partial} + \%\gamma \cdot \rho_{\gamma} + \%l \cdot \rho_{l} \tag{4.47}$$

$$TLE = \left(\rho_o / \rho_{tot}\right)^{1/3} - 1 \tag{4.48}$$

The TLE functions and phase fractions are calculated as a function of temperature and carbon content. The model adopts TLE functions for plain carbon steel, as seen in Figure 4.5 and Figure 4.6, based on solid phase density data by Harste et al. [58, 59] and liquid density data from Jimbo and Cramb [60]. Phase fractions are estimated using the equilibrium Fe-C phase diagram, so nonequilibrium undercooling due to slow nucleation kinetics are neglected. The slope of the TLE function represents α, which on average is 2.3×10^{-5} K^{-1} for this work.

4.3.5 Elastic Modulus

The elastic modulus function, based off data from Mizukami et al. [61], for various carbon contents is displayed in Figure 4.7. Liquid elements as defined by the specified coherency temperature (set to solidus) and are set to have a very small elastic modulus of 10 MPa as previously discussed.

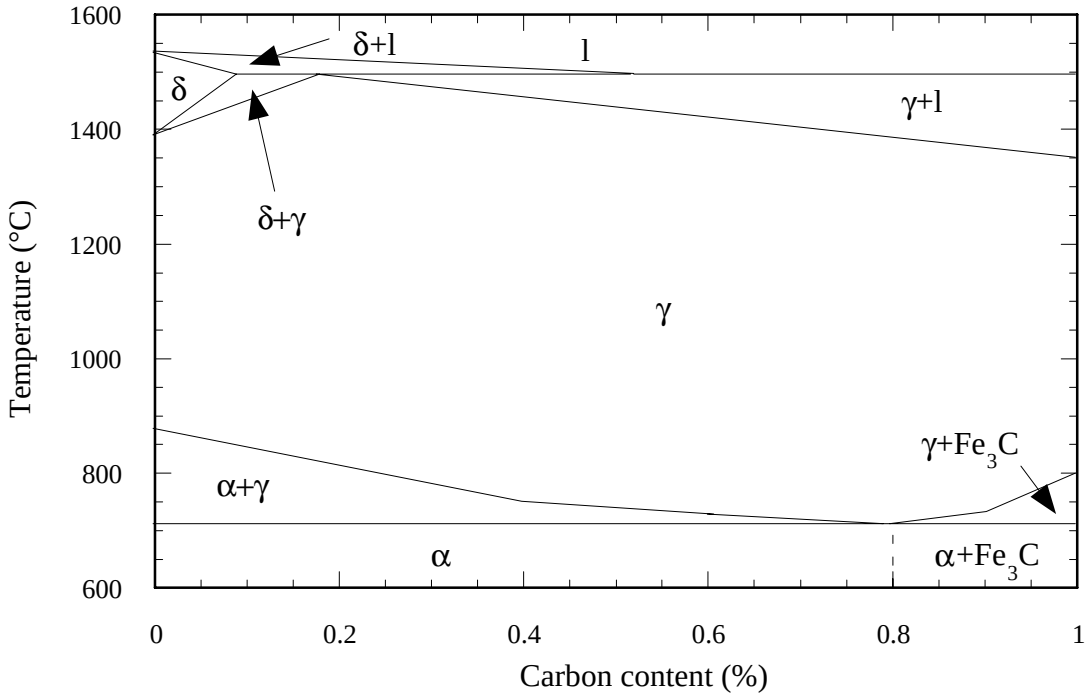

Figure 4.1. Phase diagram for plain-carbon steel used in the model

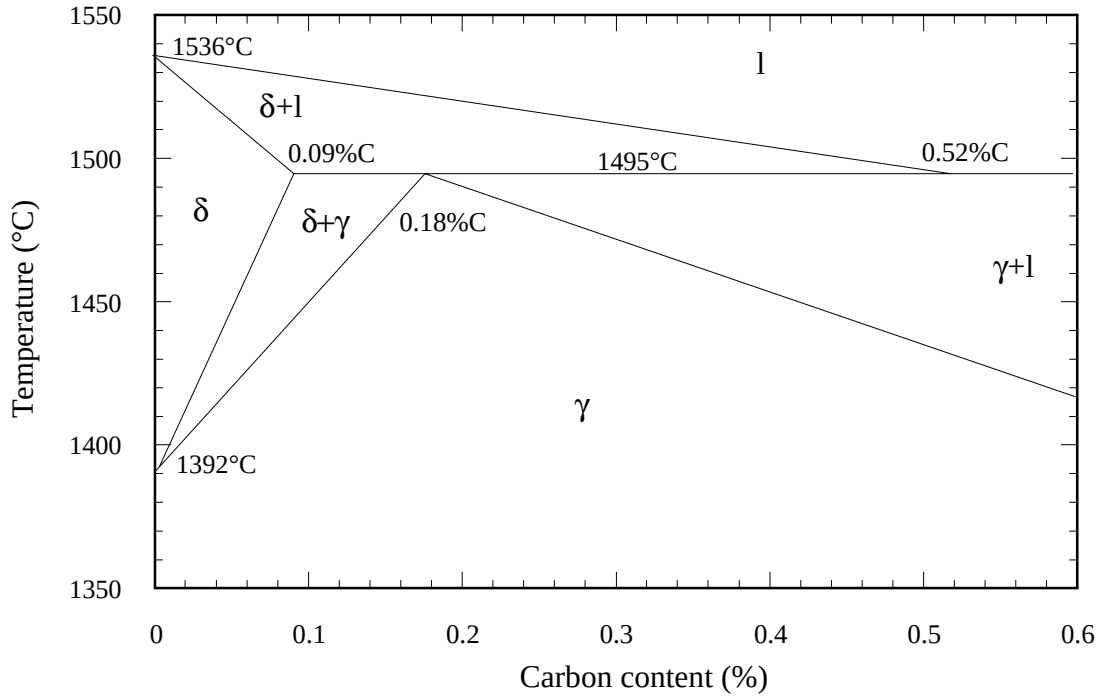

Figure 4.2. Phase diagram displaying details of high temperature region

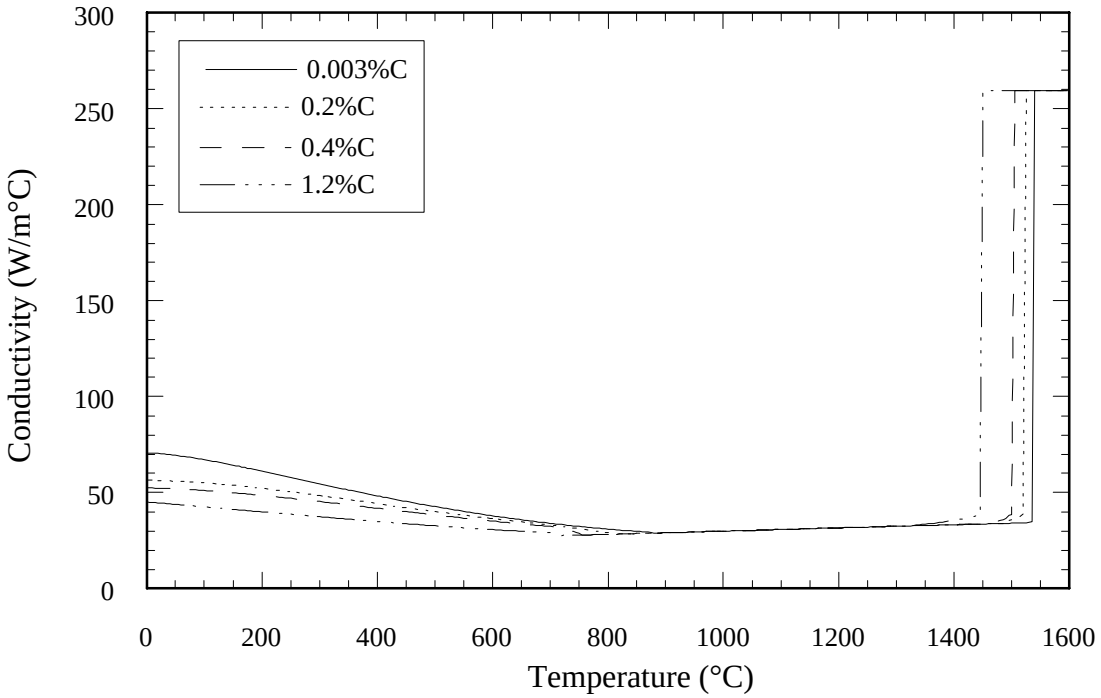

Figure 4.3. Thermal conductivity of plain carbon steels as a function of temperature

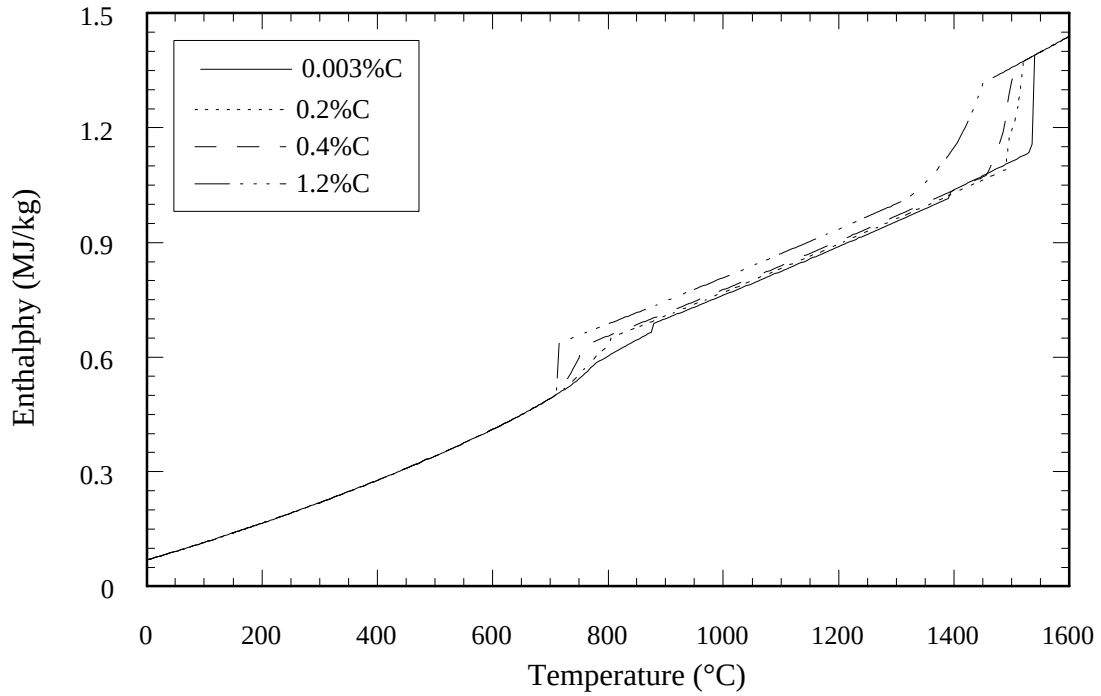

Figure 4.4. Enthalpy of plain carbon steels as a function of temperature

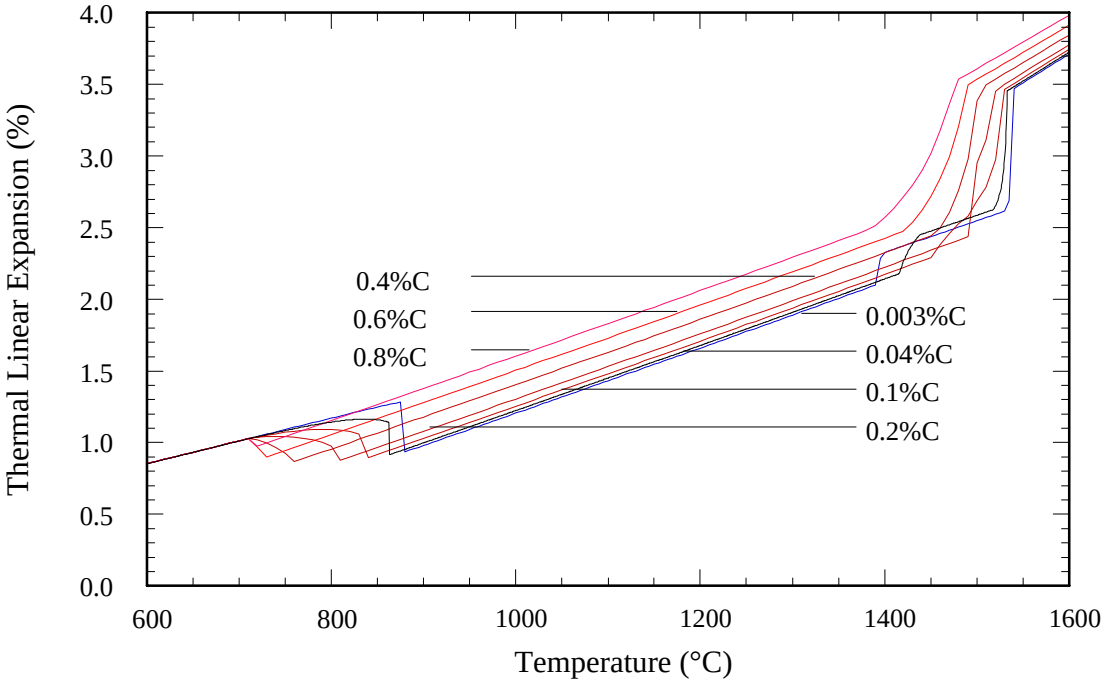

Figure 4.5. TLE of steel for various carbon content

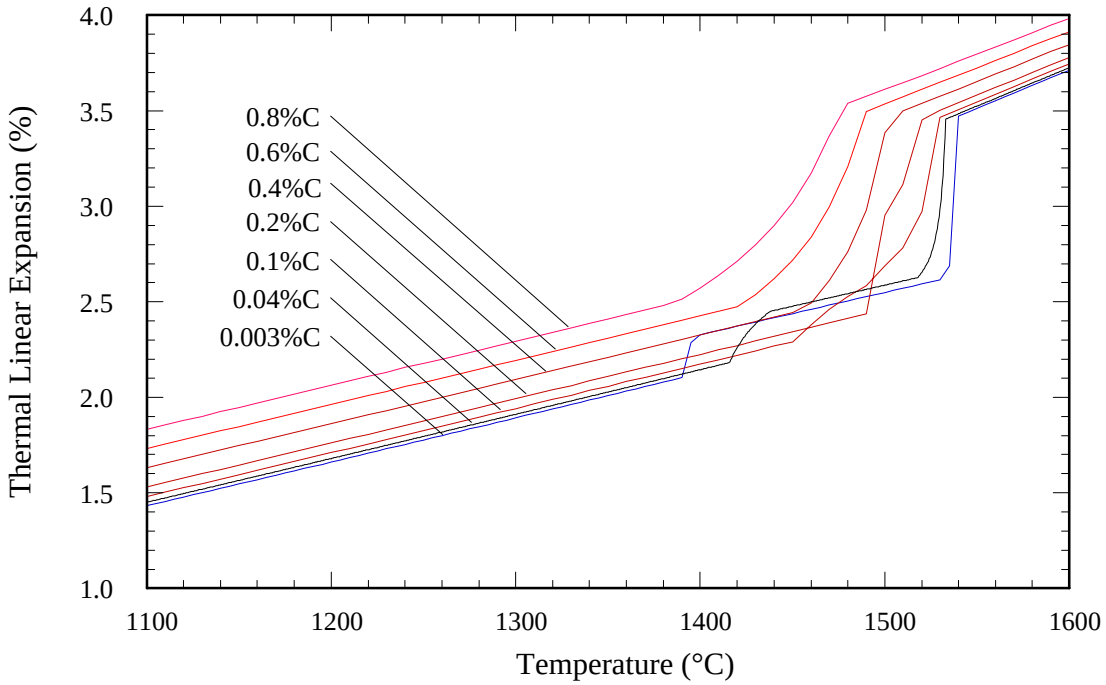

Figure 4.6. TLE displaying details of high temperature region

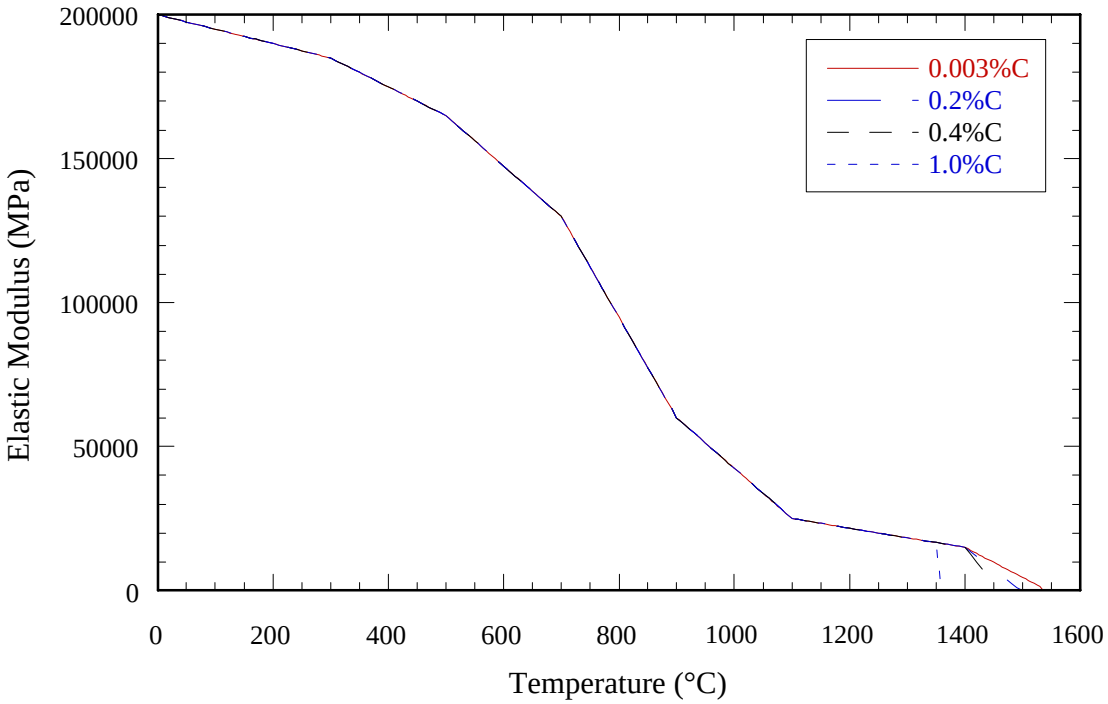

Figure 4.7. Elastic modulus of steel for various carbon content

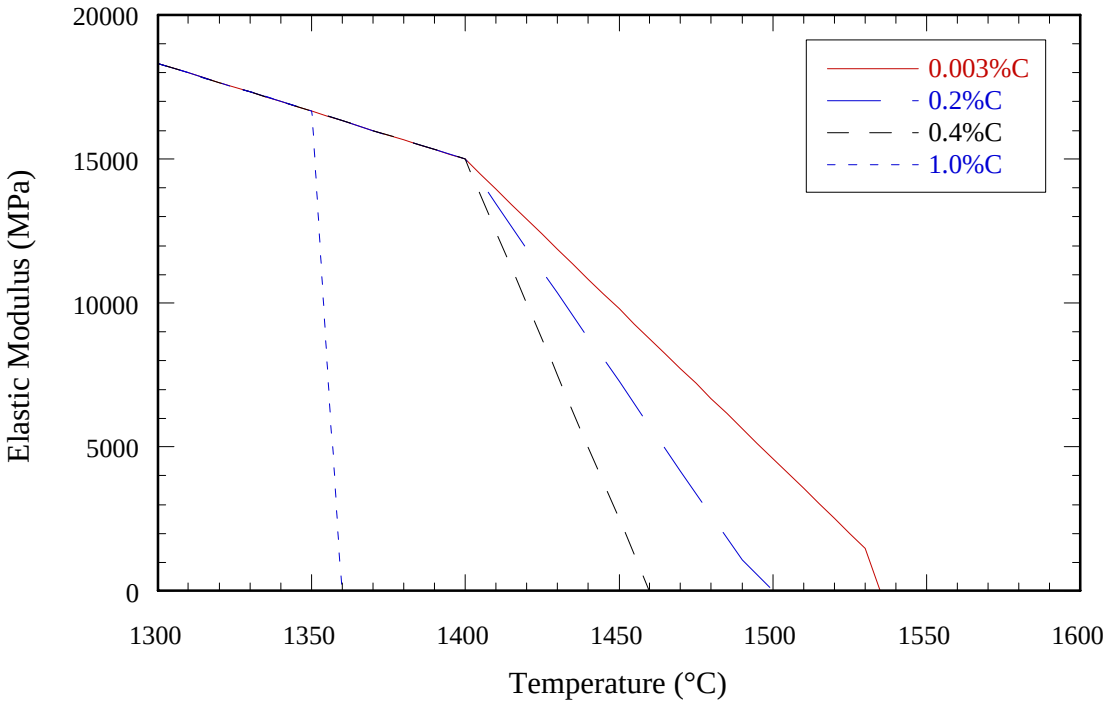

Figure 4.8. Elastic modulus displaying details of high temperature region

5 Model Validation

Computer modeling of mechanical behavior in processes involving solidification requires treatment of many complex phenomena, which can present numerical difficulties. In order for the results of computer modeling produced through the use of CON2D to be applicable, the validity of the model and the mathematical techniques it embodies must be verified. This is done by using the model to simulate steel solidification phenomena in which the end results are known, either through analytical solutions or experimental results. This chapter discusses several applications in which the model has been applied and compared to such results.

An extensive amount of work by Zhu [2] was completed to validate the mathematical techniques used by the model. An analytical solution of stress development in a solidifying body has been developed by Boley and Weiner [62]. Although the analysis oversimplifies the complex physical phenomena associated with solidification, it is useful in providing a benchmark for verification of the numerical models. Boley and Weiner [62] developed an exact analytical solution of thermal stresses during one-dimensional solidification of a slab with a temperature-dependent, rate-independent, elastic-perfectly-plastic material behavior. For this case the problem was transformed into a challenging test problem for thermal-mechanical analysis of solidification using an elastic-viscoplastic constitutive equation.

5.1 Analytical and Numerical Solution Comparison

Analytical Solution

As shown in Figure 5.1, the problem consists of one-dimensional solidification, in the x-direction, of a semi-infinite domain. The domain liquid has an initial temperature equal to the solidification temperature, T_s. At time t=0, the surface (x=0) is suddenly chilled to T_f. Figure

5.2 shows the elastic-perfectly-plastic constitutive behavior, it includes a yield stress σ_Y, which decreases linearly from 20 MPa (T_f) to zero at T_s. The other thermal and mechanical properties are set equal to constants, which are based on steel properties used by Kristiansson [44]:
ρ = 7400 kg/m^3, C_p = 700 J/KgK, K = 33 W/mK, L_f = 272 kJ/kg, T_s = 1468°C, T_f = 1300°C,
ν = 0.35, α = 2.0 x 10^{-5} K^{-1}, E = 40 GPa.

Numerical Solution

CON2D [1] was then used to analyze this one-dimensional solidification problem using a two-dimensional domain and mesh as observed in Figure 5.3. The problem was solved using generalized plane strain in both the y and z directions. This condition was implemented for the y direction by forcing the constraint, that the vertical displacements (u_y) are all equal to each other along the topside of the mesh.

The constitutive model for the present problem was transformed from elastic-perfectly-plastic into an elastic-viscoplastic model using the nonlinear rate equation for the inelastic strain rate:

$$\dot{\bar{\varepsilon}}^p = f(\bar{\sigma}, s) = A[\max(\bar{\sigma}, \sigma_Y) - \sigma_Y]^n \qquad (5.1)$$

where A = 1.0 x 10^8, n = 5.0. This equation operates as a penalty function to ensure that rapid inelastic strain occurs until the proper stress is achieved. This setup is a rigorous test of the numerical algorithms, due to the severe nonlinear nature of equation (5.1).

The mesh domain (8.0 x 0.4 mm) was used to model 10 seconds of solidification, with a time step of 0.1s using 40 six node triangular elements, as shown in Figure 5.3. Figure 5.4 shows the results from the model and the analytical solution of the temperature distribution through the slab at 2 second intervals. Figure 5.5 displays the σ_z stress distribution at 10 seconds for both the analytical and the numerical solutions. The relative error is less than 4% for the final calculation

at 10 seconds. Figure 5.5 shows that the slab goes into compression near the surface. This is because the surface layer solidifies and cools stress free. As each inner layer solidifies, it cools and tries to shrink while the surface temperature remains constant. Because the slab is constrained to remain planar, complementary subsurface tension and surface compression stresses are produced.

5.2 Constitutive Equations

The constitutive equations used to model the mechanical behavior of casting have great influence on the predicted stress due to coupling of the elastic and inelastic strains. It is therefore important to find general constitutive equations that are accurate for the range of mechanical conditions encountered in the entire solidification process. There has been a great deal of work done in order to mathematically model such mechanical behavior.

5.2.1 Kozlowski Model III

Kozlowski and Thomas [45, 46] have developed several sets of constitutive equations to model the mechanical behavior of plain carbon steel in the austenite temperature region. Several of the proposed models by Kozlowski have been implemented into CON2D [1]. However, the strain-hardening model, known as Model III [45, 46] is the best overall compromise due to the numerical stability of the model and the ability of the model to fit test data and perform under complex loading conditions. (Note subscripts are used to designate inelastic strain and strain rate)

$$\dot{\varepsilon}_P = f(\bar{\sigma}, s) = D \exp(-\frac{Q}{T}) [\sigma - a_\varepsilon \varepsilon_P^{n_\varepsilon}]^n, \tag{5.2}$$

$$D = 46{,}550 + 71{,}400\ (\%C) + 12{,}000\ (\%C)^2,$$

$$Q = 44,650\ K^{-1}$$

$$a_\varepsilon = 130.5 - 5.128 \times 10^{-3} T,$$

$$n_\varepsilon = -0.6289 + 1.114 \times 10^{-3} T,$$

$$n = 8.132 - 1.54 \times 10^{-3} T$$

Figure 5.6 shows tensile test curves calculated with Model III and Wray [63] data for various carbon contents. The figure demonstrates the mechanical behavior of the model in predicting stress / strain relations for a range of carbon contents. The fit is tolerable for a range of 0.5% to 2% strain, but discrepancies exist at very small strains (below 0.2%). This is due to the fact that all of the real steels have very similar initial behavior, and their later divergence cannot be modeled with equation (5.2).

Figure 5.7 displays the ability of Model III to reasonably accommodate mechanical property with variations in temperature, even for small strains. Figure 5.8 shows that Model III, to a limited extent, is able to characterize stain-rate variations. The inaccuracy results from the inability of this model formulation, equation (5.2), to change the slope of the integrated stress-strain curve as a function of strain rate.

Figure 5.9 displays a creep curve for the model at a temperature of 1300°C compared with data from Suzuki [7]. The figure demonstrates that the model can reproduce only the primary creep behavior. For long times, as the inelastic strain rate approaches the total strain rate, the calculated inelastic strain approaches an asymptote, since all of the variables in equation (5.2) become constant. Hence, Model III cannot accurately simulate steady-state creep and so has an inherent under prediction of strain for long times (relative to the stress level). However, the model does produce acceptable behavior at small strains and short times.

The ability of the model to reproduce experimental data under standard tensile or creep test conditions has been demonstrated above. However, conditions that arise in continuous casting are neither constant strain rate nor constant stress. The actual loading encountered in the casting process will vary between these two extremes. It involves constant changes in temperature, stress, and strain rate over wide ranges. Kozlowski et al. evaluated the ability of the constitutive equations to reproduce behavior under six different complex loading conditions, which were chosen to represent extremes of the conditions actually encountered during casting [45, 46]. Here, the focus is placed on two of these conditions, stress relaxation and cyclic loading with stress reversal. These conditions establish the mathematical ability of the model to predict complex loading behavior.

For stress relaxation model comparison, conditions were chosen to duplicate tensile tests performed by Maehara et al. [64] on plain 0.18%C steel. Monotonic loading was initially imposed at a constant slow strain rate to 1% strain. Then, the total strain was fixed by forcing the total strain rate to zero, as the stress was allowed to relax for 180 seconds due to creep. This procedure is repeated several times with the application of additional loads to increase strain by 1% in each step. Figure 5.10 displays the stress-time curve calculated using Model III for the measured stress relaxation curve at 900°C with the experimental data.

The stress-strain response of Model III to cyclic loading conditions is demonstrated in Figure 5.11. Model III has a stable cyclic behavior since it depends on strain alone to characterize the material structure. The test is performed by reversing the strain rate whenever ± 1.2% strain is achieved. The cyclic loading test of the model was performed in both 0-dimensional integration simulations and on a simplified mesh using CON2D. The test on the simplified mesh validates that CON2D was properly evaluating the signs of the effective stress and of the effective plastic strain.

Model III does very well in predicting the behavior for plain carbon steel in the austenite temperature region. However, the model does not predict the behavior for the enhanced creep rate in the delta ferrite range. In order to correctly model the mechanical behavior of steel in this range the inelastic plastic strain rate needs to be substantially increased to simulate the weak delta steel. One way to accomplish this is to multiply the term that determines the inelastic strain rate by a large constant. Because of the mathematical nature of Model III, this modification does not produce desirable effects. A simple constant inserted into Model III will force the equations to more closely resemble the steel in the delta ferrite region, however the model becomes insensitive to strain rate. Hence, in order to accurately model the delta region behavior, with this type of approach, a different set of constitutive equations needs to be used. This led to the implementation of a power law based constitutive equations into the model.

5.2.2 Power Law Model

Starting with a general power law type constitutive equation, Zhu developed constants forcing the power law equation to fit Wray data [63]. The following power law equation was then implement into CON2D.

$$\left(\frac{\sigma}{\sigma_o}\right) = \left(\frac{\%C}{\%C_o}\right)^{n_1} \left(\frac{T}{T_o}\right)^{n_2} \left(\frac{\dot{\varepsilon}_P}{\dot{\varepsilon}_{Po}}\right)^{(aT+b)} \left(\frac{\varepsilon_P}{\varepsilon_{Po}} + 1.0\right)^{(cT+d)} \tag{5.3a}$$

Rearranging in terms of inelastic strain rate:

$$\dot{\varepsilon}_P = \dot{\varepsilon}_{Po}\left[\left(\frac{\%C}{\%C_o}\right)^{-n_1} \left(\frac{T}{T_o}\right)^{-n_2} \left(\frac{\sigma}{\sigma_o}\right)\left(\frac{\varepsilon_P}{\varepsilon_{Po}} + 1.0\right)^{-(cT+d)}\right]^{\frac{1}{(aT+b)}} \tag{5.3b}$$

$\varepsilon_{Po} = 0.1\ \%$, $\dot{\varepsilon}_{Po} = 5\times10^{-6}\ s^{-1}$, $\sigma_o = 13{,}678$ MPa

$\%C_o = 1\ \%$, $T_o = 300$ K

$a = 1.617\times10^{-4}$, $b = -0.06166$

$c = -9.4156\times10^{-5}$, $d = 0.349501$

$n_1 = -0.0556$, $n_2 = -5.52$

In order to model the lower strength of the delta ferrite region, a large constant is inserted into the right hand side of equation (5.3b), which enhances the plastic creep rate accounting for the weakness associated with the steel in this phase.

$$\dot{\varepsilon}_P = f_\delta \dot{\varepsilon}_{Po}\left[\left(\frac{\sigma}{\sigma_o}\right)\left(\frac{\%C}{\%C_o}\right)^{-n_1}\left(\frac{T}{T_o}\right)^{-n_2}\left(\frac{\varepsilon_P}{\varepsilon_{Po}}+1\right)^{-(cT+d)}\right]^{\frac{1}{(aT+b)}} \tag{5.4}$$

$$f_\delta = 2.0\times10^4$$

This simple procedure reproduces behavior that accurately models the delta phase without losing strain rate sensitivity. However, in the austenite temperature region the power law is less accurate than Model III in matching complex loading situations. Therefore, the model uses both types of constitutive equations. The criteria for determining which set of constitutive equations to use is based on the fraction of delta ferrite, as determined by the phase diagram. For the present work, if the fraction of delta ferrite was greater than 10% and the temperature is less than the coherency temperature (set to solidus) then, the power law (δ phase) equations are used. Otherwise, Model III will be used. This small fraction was chosen because only a small amount of a weaker phase can weaken the whole structure if that phase is continuously perpendicular to the direction of the applied load, which is believed to be the case. Figure 5.12 compares stress values (ε=0.05) from Wray data [63] with Model III and the power law (δ phase) over a range of temperatures for two strain rates.

The power law predicts the mechanical behavior for steels in the austenite temperature range fairly well when compared with experimental data. Figure 5.13 compares the power law with data from Wray [63] for variations in strain rate. Figure 5.14 displays creep test results comparing the power law with data from Suzuki [7]. These results suggest the power law is fairly close in ability with Model III to matching experimental data. However, the power law is less accurate when it comes to handling complex situations such as cyclic loading. Figure 5.15 shows the behavior of the power law for the same cyclic loading conditions as discussed above

for Model III. In this case it is evident that the power law forces the equations into a symmetrical behavior which is not characteristic of real steel behavior. This result is due to the way the power law equations calculate the stress. When either term below,

$$(\frac{\varepsilon_P}{\varepsilon_{Po}} + 1.0) \text{ or } \dot{\varepsilon}_P$$

is negative, absolute values functions must be used around these terms in order to avoid numerical errors. However, the direction of the stress is still determined by the product of these two terms prior to the application of absolute value functions. The need for these absolute value functions forces the symmetrical behavior of the model. The symmetrical behavior could be avoided with other modifications to the power law, for instance resetting the ε_{Po} and or $\dot{\varepsilon}_{Po}$ constants based on the change of direction of either inelastic strain or inelastic strain rate. Such modifications however, would greatly increase the complexity of the model. Model III avoids this symmetric behavior because stress is based on the summation of $\dot{\varepsilon}_P$ and ε_P terms and not the product.

Although the power law has this inexact behavior for cyclic loading, it is still the best choice of constitutive relation to be used in the delta ferrite region. The inability of the model to accurately predict the behavior under cyclic loading conditions should be insignificant in the delta ferrite region, due to the large amount of positive inelastic strain that occurs in this very weak phase.

5.3 Submerged Split Chill Tensile Testing

Another application the model can be used to predict the behavior of, is a more realistic solidification process known as the "Submerged Split Chill Tensile" (SSCT) test. The SSCT test has been developed to help researchers gain insight of high temperature strength properties as a function of steel composition. The SSCT test simulates shell straining by tensile force perpendicular to the main dendrite growth axis [23].

The SSCT is performed with a cylindrical chill body split into two halves. The chill is made with either copper (water cooled) or steel (without inner cooling). The chill is then submerged into liquid steel and held for a few seconds while a steel shell begins to form. Then, the lower half of the chill is moved by a hydraulic ram downward to strain the solid shell as it continues to solidify. The chill surface is coated with alumina of varying thickness for heat flux control and facilitating the shell removal from the chill after testing is completed. Figure 5.14 shows a typical diagram of an SSCT apparatus and how the solidifying shell gets pulled apart. During the test the heat flux is derived from immersed thermocouples which can be used to calculate shell growth, solid fraction and temperature gradient.

Figure 5.17 shows the measured change of position of the lower chill-half versus time for a 0.25%C SSCT test [23]. This particular test was performed using uncooled steel bodies with an alumina coating of less than 1 mm. The recording starts, when the chill moves downward. During the entire submergence and holding time, thermal expansion of the upper half of the chill will lead to forces trying to separate the two halves. Also, solidification shrinkage of the shell surface adds to this force. Hence, the lower half moves downward, while the applied force measured at the load cell remains at zero. This is achieved through force control of the chill. At the end of the holding time, the test switches from force control to position control. At the beginning of the tensile test (after 12 seconds of holding) the lower half is moved downward with controlled velocity. When movement starts, the force is redefined to be zero.

The SSCT test was simulated using a thin mesh (0.5 mm x 25 mm). The mesh represents a two-dimensional slice (in x and y direction) through the solidifying shell. Figure 5.18 shows a schematic of the model domain and the boundary conditions applied. The heat flux applied to the chill / steel interface is based on thermocouple measurements and is adjusted so that shell growth between the test and experiment are almost equivalent. The boundary conditions along the upper side of the mesh are constrained such that the vertical displacements u_y are all equal to

each other along the top side of the mesh. Boundary conditions are also applied to the mesh to try and mimic the position versus time curve. Three separate constant strain rate boundary conditions are applied to the mesh at various times. The strain rates are approximated from the position versus time graph as displayed in Figure 5.17. The initial 12 second holding time is broken into two regions of approximately constant strain. The first region lasts about 2.7 seconds after submergence. During this time, the measured position changed by 0.23 mm. Knowing the height of the chill (37 mm) a strain rate of 0.0023 s^{-1} is calculated. Similarly, a strain rate of 0.0004 s^{-1} is calculated for the second part of the region. The strain rate applied to the tensile test region is calculated at 0.046 s^{-1}. This approach, provides a good estimate of the strain rate during the test. To more accurately model the solidification, the position data from the SSCT could be applied directly as the mechanical boundary condition.

Figure 5.19 displays the force versus time curves for both the measured and simulated results. The true force on the shell was not measured prior to the hold time (12 seconds) so, for comparison purposes, the axis of measurement is offset from the calculation. Similarly, the time of applied load is offset to measure from the time of initial submergence in both cases. At the present time, it is unclear why the modeled data oscillates. The behavior is believed to be a problem within the post data processing routine and not originating from the model.

The measured results show a steep force increase, after the tensile force begins, which quickly goes to a constant before declining right before the test terminates. Before the test officially starts, the model predicts force growing during the hold time. This is reasonable, because an ever increasing force on the shell is required to prevent its contraction. At the beginning of the tensile test, a sharp increase in force is observed before the force continues to rise at a nearly constant rate. It is not certain whether this could be detected by the measurement procedure or not, as it occurs during the transition from load to velocity control. With all the simplifications, the model does well in predicting the principle aspects of the phenomena. For the first couple of

seconds after the tensile test begins, the data and simulation have very similar positive slopes. After the measured maximum, it is likely the shell has begun to fail due to strain localization as a result of non-uniform necking. This is not simulated, so the model is unable to predict the subsequent mechanical behavior of the thin shell. Overall, the model gives a reasonable prediction of this extreme real life solidification process and does well in predicting the behavior of the shell through the early part of the tensile test.

5.4 Molten Liquid Steel Droplet Prediction

In order to gain further insight into steel solidification phenomena and to ensure model validity, simulations were attempted to predict deformation of a molten steel droplet based on comparison with experimental measurement by Dong et al. [20]. This work provides insight into the early phases of steel solidification as well as to serve as validation for inelastic constitutive models and to provide information on the role of carbon content during initial solidification.

This problem also focuses on the ability to predict realistic heat transfer boundary conditions. Much research has been done on trying to determine how the heat transfer coefficients vary in small solidifying droplets [15, 16, 18, 19, 21, 65-67]. Most of this research has been geared to how very high heat transfer coefficients are going to lead to thermal undercooling and furthermore, how this may effect the final microstructure [15, 19, 67].

For this work, nonequilibrium undercooling was assumed to be insignificant to the final droplet shape. Several other important phenomena will also be ignored in the scope of the droplet prediction. CON2D currently does not account for segregation or microstructure throughout the solidified steel. However, since the model domain represents such a small sample size, undercooling should not be that significant and the effects of segregation on droplet deformation should be minimal.

The experiment established by Dong et al. [20] consists of a 4 to 8 gram size droplet of steel falling a distance of approximately 35 mm and solidifying on a copper chilled surface as seen in Figure 5.20. After being dropped onto the mold the sample forms a button shape, with an approximate diameter of 10 mm for a 4 gram sized droplet. After solidification and cooling to room temperature, the curvature is measured using a digital gauge with a precision of 0.003 mm. The amount of curvature varies greatly with small changes in steel carbon content. For example, in the large 8 gram droplets it is observed for low (0.01%C), medium (0.10%C) and high carbon contents (4.23%C), that the bottom curvature is convex toward surface chill. For steels (0.76%C and 1.37%C) the sample deformed concave toward surface chill [20]. Figure 5.21 shows representative sketches of the final droplet shape. For the smaller droplets (around 4 grams), only ultra-low to mid values of carbon content were measured, less than 0.23%C. All these droplets had final convex shapes, although the amount of deformation varies significantly with carbon content.

It has been shown [20] that the amount of concave or convex deformation can be fitted to a parabolic shape (by the least square method) with a very high accuracy:

$$w = N_d r^2 \tag{5.3}$$

Where w is the bottom surface height (Z-displacement), r is the radius (measured from center of droplet), and N_d the coefficient giving the magnitude of deformation. Thus, the final bottom shape and droplet deformation simplifies to a single value, N_d [m^{-1}].

5.4.1 Estimation of Deformation

A simple analytical model for the physics on the problem has been proposed by Dong et al. [68] with application to pure materials. After the liquid sample is dropped on the chill, solidification starts from the bottom uni-directionally upwards, eventually reaching the top surface. The entire

sample then eventually cools to room temperature. Because the initial solid shell is very thin, it is suppressed by the weight of the sample and kept flat by plastic deformation. At a certain thickness S_c, the shell is able to support the weight and the sample starts deforming thermoelastically with the decrease of the temperature gradient present. Assuming a linear temperature gradient and a constant thermal expansion coefficient α, the growing solid shell will be free of stress all the time. Hence the final deformation, N_d, will depend only on the temperature gradient G_{Sc}, at the start of thermoelastic deformation. This model can be approximately identified with a problem of an elastic plate with free boundaries. Initially, there is no stress or displacement in the plate, but there is a temperature distribution, given by:

$$T = T_i + G_{Sc} Z \tag{5.4}$$

From stress-strain relations, the Z-displacement of the plate has been shown to be [69]:

$$w(r, Z) = \alpha G r^2/2 - \alpha(ZT_i + GZ^2/2) \tag{5.5}$$

Because only the bottom deformation is of interest, by letting Z=0 in the above equation and from substitution of equations (5.3) and (5.4):

$$N_d r^2 = \alpha G r^2/2 \tag{5.6}$$

$$N_d = G_{Sc} \alpha/2 \tag{5.7}$$

This model was developed for application to pure materials, and therefore only gives us insight as to what is happening in materials that do not go through phase changes. This model also does not provide the criterion for the onset of deformation that defines G_{Sc}. Explanation of this and what is occurring in steel grades with various percentages of carbon content will be discussed later in this section, based on simulations with the present numerical model.

Simple heat transfer results were then derived using CON2D on an ultra-low carbon steel. This was done by assuming a constant heat transfer coefficient equal to 2.0×10^4 $Wm^{-2}K^{-1}$, typical for molten steel on copper, a constant chill temperature of 35°C, and a 4 gram sample size at

liquidus temperature. From the CON2D heat transfer results, initial temperature gradients (G_{Sc}) could be calculated at various times. Assuming a constant α equal to 2.0 x 10^{-5} K^{-1}, estimates of N_d for various time estimates are given in Table 5.1. Because these results are based on a constant heat transfer coefficient the temperature gradient through the solid shell is going to continually decrease. Hence, earlier times for (G_{Sc}) will produce more deformation.

Time	0.01 s	0.02 s	0.035 s	0.05 s
G_{Sc}	7.58E5 Km^{-1}	6.83E5 Km^{-1}	5.89E5 Km^{-1}	5.78E5 Km^{-1}
N_d	7.58 m^{-1}	6.83 m^{-1}	5.89 m^{-1}	5.78 m^{-1}

Table 5.1. Values of degree of deformation calculated for various start times

5.4.2 Interfacial Heat Transfer

In addition to initial calculations for deformation, research was also performed to understand the heat transfer phenomena at the copper / steel interface. This type of heat transfer problem however can be very difficult to solve. The conduction of heat from the splat into the substrate starts out one-dimensional, but increasingly becomes two-dimensional as heat penetrates deeper into the substrate. However, these two-dimensional effects seem not to predominate very early in the solidification process and a one-dimensional approach should suffice [15]. The main emphasize comes in determining the heat transfer coefficients between cooper and steel as the droplet solidifies. For splat cooling the heat transfer coefficient varies between 1 x 10^4 to 5 x 10^6 $Wm^{-2}K^{-1}$ [70].

Todoroki and Cramb [21] solidified stainless steel droplets on a water-cooled copper plate and measured temperatures both in the copper and at the steel interface. Although their droplets were about the same size (3.5 g), the liquid was ejected under 2 atm pressure and more spreading was observed. The heat transfer coefficient was determined to rise quickly (during the first 0.01

seconds) to a maximum of 4 x 10^3 $Wm^{-2}K^{-1}$ to greater than 1.2 x 10^4 $Wm^{-2}K^{-1}$, and then usually fall to less than 2 x 10^3 $Wm^{-2}K^{-1}$ to 5 x 10^3 $Wm^{-2}K^{-1}$ after 0.5 seconds. The bottom shapes in this work were wavy with mean amplitude (roughness) of 20 to 40 μm. Increasing superheat greatly increases the maximum heat transfer coefficient [18, 21] and decreases the final roughness [21].

Once the droplet begins to solidify at some point it is going to begin to deform away from the copper chill. At this time, the heat transfer coefficient is going to decrease dramatically due to the thermal resistance of the air gap. The heat transfer coefficient after deformation is expected to become lower than 5.0 x 10^4 $Wm^{-2}K^{-1}$ [20]. Thus, at least two distinct values for heat transfer coefficient need to be used. Liu et al. [17] use this approach to successfully match temperature predictions with experiments on nickel droplets solidifying on metal substrates. They also predict that the heat transfer coefficient may decrease by an order of magnitude once the droplet starts to solidify. The heat transfer coefficient then becomes a function of time with three critical parameters: the initial heat transfer coefficient (h_1), the lower value heat transfer coefficient (h_2), and the corresponding transition time (t_h).

Based on this research and experience, a heat transfer value of 2.0 x 10^4 $Wm^{-2}K^{-1}$ is assumed for the initial start of solidification, h_1. Dong and other researchers have used similar values [20, 67]. The heat transfer coefficient is then assumed to drop to 5.0 x 10^3 $Wm^{-2}K^{-1}$ (h_2) or less once the droplet starts to pull away from the chill near 0.05 seconds, t_h.

5.4.3 Chill Temperature Estimation

During solidification, the copper chill experiences a temperature change near the surface. In order to roughly estimate how much the copper surface heats up, preliminary droplet heat transfer results from CON2D were used. Heat transfer simulations were performed assuming an

h_1 equal to 2.0 x 10^4 $Wm^{-2}K^{-1}$, h_2 equal to 2.0 x 10^3 $Wm^{-2}K^{-1}$, and t_h equal to 0.05 seconds and a constant chill temperature of 35°C solidifying a 0.003%C droplet with an initial temperature of 1536°C. The results of the surface temperature of the droplet were then used to calculate a corresponding temperature response on the copper chill. For short lengths of time (i.e. the center of the slab has not yet felt the effects of the changing temperature field) the copper chill can be represented as a semi-infinite plate. Poirier and Geiger [71] show for this situation the temperature can be roughly estimated by the following equation:

$$\frac{T - T_i}{T_f - T_i} = \operatorname{erfc}\left[\frac{x}{2\sqrt{\alpha t}}\right] - e^{\gamma}\operatorname{erfc}\left[\frac{x}{2\sqrt{\alpha t}} + \frac{h}{k}\sqrt{\alpha t}\right] \qquad (5.5)$$

$$\text{where, } \gamma = \frac{h}{k}\sqrt{\alpha t}\left[\frac{x}{2\sqrt{\alpha t}} + \frac{h}{k}\sqrt{\alpha t}\right]$$

Here T_i is the initial temperature of the chill and the surface temperature of the droplet is substituted in for T_f along with the heat transfer coefficient function for h. Figure 5.22 displays preliminary results of the surface temperature of the droplet along with the heat transfer coefficient function. Figure 5.23 shows the calculated temperature effects on the surface (x=0) of the copper chill using equation (5.5).

The temperature of the copper is estimated to reach a maximum of around 200°C. Todoroki and Cramb predict a maximum temperature near 100°C, from thermocouple measurements 1 mm below the surface of the copper chill [21] from experiments similar to Dong et al. [20]. A temperature of 35°C is accurate at the critical initial stage, and 200°C is accurate later. Relative to the droplet surface temperature near 1400°C, this is not much different from the initial temperature of 35°C. Thus, the simulations will assume a constant substrate temperature of 35°C, and the heat transfer will be primarily driven by the magnitude of the heat transfer coefficient. The amount of heat transfer will be controlled solely by the heat transfer coefficient function. This assumption will help simplify the analysis as the heat transfer coefficient function will vary between grades.

5.4.4 Model Approach

To best model the problem will require the ability to model stress, strain, heat transfer and solidification. The model domain consists of a two-dimensional center slice of the sample. It is assumed the surroundings are adiabatic and only uni-directional cooling will occur between the droplet and the chill.

The model domain will consist of one-half of the droplet size, as observed in Figure 5.24. This situation requires the nodes along the symmetry plane to be fixed in the r direction. Furthermore, to prevent rigid body motion, the corner node in the plane is fixed in the Z direction. For modeling purposes, the real world Z (solidification) direction is equivalent to x, and hence the notation Z[x] is used to refer to the solidification direction. Similarly, the same notation is used for the real world radial direction r[y]. A pressure boundary condition is applied along the top surface of the mesh to mimic the effects of gravity and momentum. The use of gap elements along the bottom prevents the droplet from penetrating into the copper mold. The mold itself is assumed to be flat and a constant 35°C.

For the heat transfer boundary conditions the three outside surfaces are assumed to be adiabatic. The copper chill is replaced by the heat transfer coefficient function and an ambient temperature of 35°C. Figure 5.25 displays the mesh and heat transfer boundary conditions used to model the steel droplet. The (5 x 6 mm) mesh consists of 5400 heat transfer elements and 1350 stress elements. The mesh has a linear grade applied to the elements in the Z[x] direction. This grading allows for a finer mesh size during the initial part solidification, which will have the most effect on final droplet deformation. The magnitude of the ferrostatic pressure boundary condition is equivalent to the 6 mm head of liquid steel and applied on the solidification front. The application of the ferrostatic pressure and gap elements is applied once the steel shell is at

least one element thick to ensure the steel has strength. For all the work presented here, this time was 0.01 seconds into the simulation.

The time step size is also varied to allow for a very small initial time step. Figure 5.26 displays the time step size as a function of simulation time. By periodically doubling the time step size from the initial size of 0.1 ms, the accuracy needed with small initial steps is achieved and total computation time for the simulation is manageable. Care was also taken not to have time step changes occur near phase-transformations. For most simulations, depending on the heat transfer coefficients, the surface temperature of the droplet cools to around 100°C by 20 seconds into the simulation. Simulations of this length (approximately 3600 time steps) take about 24 hours running on an IBM RS6000-370.

Because of the nature of solidification, it is very difficult to predict the heat transfer coefficient function accurately. When the droplet first hits the chill, the bottom surface will flatten out and a high heat transfer will ensue between the steel and the copper. Then at some point after solidification, the droplet will be able to support itself and start to pull away from the chill, thereby reducing the heat transfer coefficient. Thus, determining when the heat transfer coefficient drops will be decided from trial and error simulations. To do this, simulations are first performed with a constant initial heat transfer coefficient, to help determine when the shell begins to pull away from the chill.

5.4.5 Droplet Results

Overall, the results of the droplet simulation are very encouraging. Much of the initial modeling work was completed on ultra low-carbon steels, particularly 0.003%C. The work completed on this grade provided a basis for simulation of the higher carbon contents.

The heat transfer coefficient plays a large part on how the droplet forms. The heat transfer coefficient function has a direct effect on how the temperature gradients of the droplet develop. Figures 5.27 and 5.28 show the temperature gradients throughout the droplet for various times with a constant heat transfer coefficient. Figure 5.27 shows the temperature gradient decreasing as the droplet cools. Hence, from the theoretical model prediction less surface deformation should take place if the heat transfer coefficient is dropped at a later time.

One of the initial difficulties in the droplet simulation, was to establish at what time to decrease the heat transfer coefficient. This is one of the major problems associated with modeling coupled phenomena. The heat transfer coefficient at solid shell / chill interface is affected by the deformation of solid shell and, the change of heat transfer coefficient at the interface will influence the shell deformation. Therefore, careful judgment must be made in justifying why and when h should be decreased. The decrease in heat transfer should occur when the droplet begins to pull away from the chill. As the droplet begins to deform, its bottom surface will attain a parabolic shape. Instead of constantly examining this entire surface shape, the focus is shifted to the outermost corner node on the bottom surface as seen in Figure 5.21a. The amount of Z-direction displacement experienced by this node is a good indicator of the amount of deformation experienced by the entire bottom surface.

5.4.5.a Effect of Pressure and Gap Boundary Conditions

Initial simulations were performed to examine the combined effects of the pressure and gap elements on deformation of the solidifying shell. Figure 5.29 compares simulations with and without these boundary conditions using a constant heat transfer coefficient. Both curves show the droplet surface breaks away from the chill very early into the simulation and adopts the curved shape shown in Figure 5.21a. The graph displays the corner node displacement, in the Z direction away from the chill, as a function of time along with the surface temperature of the

droplet. The restriction of the ferrostatic pressure and mold constraints, forces the shell initially to remain flat and represents a more realistic approach of what is happening to the droplet. Both simulations begin to deform in a concave manner at nearly the same time. However, because the pressure conditions do not allow penetration into the mold, this case lifts away from the chill surface slightly earlier. Because determining the time the droplet lifts away from the chill is a crucial parameter in the heat transfer analysis, all the subsequent droplet simulations use both the pressure and gap mechanical boundary conditions, as they represent more realistic physical behavior.

5.4.5.b Effect of Decreasing the Heat Transfer Coefficient

The heat transfer coefficient during initial solidification can vary greatly. Its effect on droplet deformation is explored parametrically. Even with a constant heat transfer coefficient, Figure 5.30 displays the corner node displacement, in the Z direction away from the chill, as a function of time, along with the corresponding surface temperature, for a constant h of 2.0×10^4 $Wm^{-2}K^{-1}$. In this simulation the pressure and gap elements keep the droplet flat initially. Without any decrease in h, the shell gains enough strength and starts to pull away from the substrate around 0.035 seconds. Hence, for this particular grade, a decrease in h occurring near 0.035 seconds is reasonable. For comparison, Figure 5.30 also displays the deformation for a similar case in which the only change is the heat transfer coefficient is dropped to 5.0×10^3 $Wm^{-2}K^{-1}$ at 0.035 seconds. Figure 5.31 shows the corner node displacement for this simulation again, along with the heat transfer coefficient function. The heat transfer coefficient is decreased from 2.0×10^4 $Wm^{-2}K^{-1}$ to 5.0×10^3 $Wm^{-2}K^{-1}$ at 0.035 seconds. The figure shows the drop in h and the droplet pulling away from the surface coincide. After h is decreased the surface temperature quickly rises back up, before it begins to gradually cool down. The surface reheating can also be observed by examining the temperature slice histories of the droplet. Figure 5.32 shows the development of the temperature profile throughout the droplet for the initial part of the

simulation. As the droplet begins to cool, a steep temperature gradient develops near the surface of the steel, due to the large heat transfer coefficient. The gradient starts to decrease slowly as the surface temperature drops. At 0.035 seconds the drop in h causes the surface gradient to decrease, so heat from inside the droplet is conducted to the surface faster than it can be removed. This makes the surface temperature of the droplet reheat by 115°C. This is comparable to the measured surface reheating, but should not be mistaken for classic recalescence due to undercooling, which is not possible in this model. Figure 5.33 displays the results for the later part of the simulation, in which the temperature gradient continues to decrease. Another sharp drop in temperature gradient accompanies complete solidification of the droplet around 4.8 seconds. The drop would be larger if cooling from the top surface was not zero. The temperature gradient continues to drop gradually after solidification and almost becomes level before the simulation is ended around 23 seconds. The surface temperature of the droplet at the end of the simulation is around 112.8°C.

The corner node displacement and the surface temperature of the droplet can be seen in Figure 5.34. The surface initially pulls away from the chill, so h decreases and the surface temperature heats back up. Shortly after 0.2 seconds, the surface relaxes and becomes slightly less deformed. The surface temperature at this point is around the transition temperature for the δ to γ phase change in the constitutive equations. For the 0.003%C grade, the transition temperature is 1393.9°C. Figure 5.35 displays the surface temperature and corner node displacement for the entire simulation. Between 0.5 seconds and 5 seconds the surface deformation has a steady increase. At around 5 seconds the deformation increases slightly more because of the change in thermal expansion due to the phase transformation from γ to α. By 8 seconds most of the deformation has taken place, and after 10 seconds the amount of deformation increases slightly as the solid droplet begins to cool down.

5.4.5.c Droplet Shell Growth

Figure 5.36 shows the calculated shell growth history. The start of contraction and drop in transfer coefficient occurs when the shell is less than 0.3 mm thick. For the equilibrium conditions assumed, the solidification rate drops from roughly 10 mm/s initially to 2 mm/s at 1 second, to less than 1 mm/s when the droplet solidifies near 4.8 seconds. This rate is almost three orders of magnitude slower than the growth rate predicted with 100°C undercooling [67]. Thus, if any undercooling occurs, the solidification front will quickly grow to the thickness given in Figure 5.36, as soon as nucleation finally starts. The drop in solidification rate which follows this rapid initial spurt is likely responsible for the sharp change in microstructure commonly seen near the surface of rapidly solidified steel.

5.4.5.d Droplet Stress Development

Figure 5.37 shows the predicted y stress profiles at several important times for the 0.003%C simulation. The initial stress profile (at 0.5 seconds) is qualitatively similar to that observed in Figure 5.5 (one-dimensional solidification), with compression along the droplet surface and tension towards the interior. The magnitudes are slightly lower, however, owing to the stress relief of bending. The temperature gradients, deformation, and stresses do not change significantly for the next 5 seconds. After complete solidification of the droplet, however, temperature gradients within the droplet relax setting up significant tensile stress in the droplet interior and balancing compression in both exterior layers.

5.4.5.e Determining the Amount of Droplet Deformation

The amount of surface deformation for a droplet, is calculated by finding the total amount of displacement experienced by the 31 nodes representing the droplet bottom surface. Both the Z-

direction and r-direction nodal displacement values are added to the original nodal positions to obtain an accurate representation of the bottom surface. The least square method is then used to obtain the best parabolic fit to equation (5.3). Figure 5.38 displays the final deformation for a 0.003%C droplet cooled to a surface temperature of 112.8°C along with its parabolic fit. For this case the amount of deformation is 9.05 m^{-1}. Table 5.2 displays the main parameters of the simulations and the amount of final deformation. The present case with the heat transfer coefficient dropped at 0.035 seconds is labeled as Case 1.1 in Table 5.2.

Similarly, the amount of deformation can be quickly estimated from the amount of displacement experienced by the corner node alone. Equation (5.3) can be rewritten as:

$$N_d = Z/r^2 \tag{5.6}$$

N_d is then calculated by substituting in for Z and r, the amount of displacement experienced by the corner node and the nodes original radial position of 5 mm, respectfully. Figure 5.35 shows at the end of the simulation the corner node displacement value is 206.1 μm. Using equation (5.6), this value results in an estimated N_d value of 8.24 m^{-1}, which is only slightly less than 9.05 m^{-1} as previously determined by curve fitting.

5.4.5.f Effect of the Final Heat Transfer Coefficient, (h_2)

Simulations on this grade of steel were also performed to examine the effects of cooling the droplet down slower. The same simulation as above was run using a heat transfer coefficient function that dropped to 2.0 x 10^3 $Wm^{-2}K^{-1}$ at 0.035 seconds instead of 5.0 x 10^3 $Wm^{-2}K^{-1}$. This simulation is labeled as Case 1.2 in Table 5.2. Figure 5.39 compares the initial deformation for both Case 1.1 and Case 1.2. The figure shows that lowering the final heat transfer coefficient slightly increases the bending at early times. This is because there is a greater drop in the temperature gradient while the shell is still thin. The effect on increasing the amount of final

deformation is much smaller. Figure 5.40 displays the entire simulations showing the development of the deformation. While the paths look different, the simulations have comparable final values of N_d. For Case 1.2, the final deformation is 9.28 m^{-1} at a surface temperature of 476°C. This value would increase slightly if the simulation was run to a surface temperature of around 100°C. For Case 1.1, the calculated increase in N_d due to the cooling down from a surface temperature of 500°C to 100°C is less than 5%. Most of the initial simulations were cooled to a surface temperature around 100°C, however, to save computation time later simulations where only run to a surface temperature around 500°C, decreasing the computation time by about 30%.

For this grade of steel, changes in the final value of the heat transfer coefficient (h_2) had little effect on the amount of final deformation. Changes made to the heat transfer transition time (t_h) had more of an effect. If the transition time is delayed to 0.05 seconds, the surface temperature was allowed to fall below 1300°C, forming a significant layer of austenite while the shell was still flat. When the surface reheated to 1430°C, this cold surface layer transformed back to delta ferrite, producing an expansion that generated further bending. By using a later transition time, more of the solidified steel shell will be reheated from the γ phase back into the δ phase. For earlier transition times more of the shell will stay in the δ phase, and will not go through a phase transition as the surface reheats. Figure 5.27 displays the temperature slice gradients through the droplet at various times with a constant h of 2.0 x 10^4 $Wm^{-2}K^{-1}$, along with the transition line which determines the δ to γ phase transformation. At 0.05 seconds almost half of the solid shell is at a temperature below the phase transition line. Figure 5.41 compares the initial deformation for heat transfer transition times of 0.035 seconds and 0.05 seconds. The longer transition time (0.05 seconds) increases both the initial and subsequently the final deformation. The final amount of curvature, near 17 m^{-1} for this case, greatly exceeds that for the shorter transition time of 0.035 seconds.

5.4.5.g Ultra Low and Low Carbon Steel (0.003%C and 0.05%C)

For 0.003%C, transition times more than 0.035 seconds caused higher final N_d values. This behavior is opposite from the simple theoretical model of Dong [20], which predicts a longer transition time should result in less deformation. The reason for this result has to do with the δ to γ phase transition, which the theoretical model neglects. Thus, longer transition times may not always lead to less deformation, if phase transformation are present. As the droplet solidifies the surface cools into the γ phase. The drop in heat transfer coefficient then increases the surface temperature of the shell, forcing the γ phase to transform back into δ phase. This transformation back to δ, results in a large amount of initial deformation. The amount of initial deformation represents the bulk of deformation experienced by the droplet. This result is discussed further in section 5.4.6.

The model was applied to simulate droplet deformation of several other carbon contents. Much of the behavior of 0.05%C steel is the same as the 0.003%C grade. To understand the transition time for 0.05%C, a simulation was performed using a constant high heat transfer coefficient. Figure 5.42 displays the initial corner node displacement along with temperature for both the 0.003%C and 0.05%C run under the same conditions with a constant h of 2.0×10^4 $Wm^{-2}K^{-1}$. The 0.05%C begins to pull away from the chill about 0.01 seconds earlier than the 0.003%C grade. Both grades pull away from the chill shortly after the surface temperature drops below the δ to γ phase transition temperature. The 0.05%C steel, was assumed to have a δ to γ transition of 1423°C, almost 30°C higher than 0.003%C steel.

Using a transition time of 0.025 seconds, Figure 5.43 displays the displacement and temperature curves for two different simulations. The first simulation drops the heat transfer coefficient from 2.0×10^4 $Wm^{-2}K^{-1}$ to 5.0×10^3 $Wm^{-2}K^{-1}$ at 0.025 seconds, and the second simulation drops from 2.0×10^4 $Wm^{-2}K^{-1}$ to 2.0×10^3 $Wm^{-2}K^{-1}$ at 0.025 seconds, (Case 2.1 and Case 2.2 respectfully).

For both cases the droplet has some initial deformation immediately after the heat transfer drops. The amount of this initial deformation is substantially less than that observed for the 0.003%C cases. For 0.05%C steel the phase transition temperature is 1423°C as observed in the plot. In Figure 5.41 the surface temperate just dips sharply below the transition line, so very little of the solid shell will be reheated back through this temperature. Again, this agrees with the 0.003%C cases.

Unlike the previous results for 0.003%C, 0.05%C has substantially more dependence on the final heat transfer coefficient value. Examination of Figure 5.43 shows that most of the initial deformation is diminished for both cases as the surface temperature decreases. For Case 2.1, however, the shell begins to deform again as it enters into the γ phase, whereas Case 2.2 has less deformation when it eventually enters this transition Figure 5.44 displays the displacement and temperature for Case 2.1 and Case 2.2 for the later part of the simulation. The two simulations have very different results for the first couple seconds of the simulation, after which they show similar patterns but at different magnitudes of deformation. Table 5.2 shows the final results of these simulations in which N_d for Case 2.1 is 5.65 m^{-1} and N_d for Case 2.2 is 2.68m^{-1}.

5.4.5.h Medium Carbon Steel (0.12%C)

The 0.12%C steel has comparable deformation in magnitude to 0.003%C, but the deformation processes are quite different. Figure 5.45 shows, with a constant h, this grade begins to pull away from the shell right around 0.015 seconds, quicker than both 0.05%C and 0.003%C. Using a transition of 0.015 seconds, Figure 5.46 shows the initial part of simulation Case 3.1. However, when the heat transfer is dropped the surface temperature heats up and the shell no longer pulls away as it did in the constant h case. For the case of the constant h, the shell rapidly cools into the γ phase causing the initial deformation around 0.015 seconds. For the case in which h is dropped, the shell remains flat for an additional 0.085 seconds, after which it begins to

deform around 0.01 seconds. At 0.1 seconds the surface temperature is around 1450°C, which is very close to the transition temperature (for the phase change from δ to γ) of 1467°C. Figure 5.47 again displays the early part of the simulation with the phase transformations labeled accordingly. Because the drop in h reheats the shell back into the δ+γ phase, there is little deformation until the shell again cools into the γ phase. Once in the γ phase the shell deforms very rapidly with most of the droplet deformation occurring within the first 0.5 seconds as displayed in Figure 5.48. The final deformation is 11.99m^{-1} as displayed in Table 5.2 (Case 3.1).

5.4.5.i High Carbon Steel (0.16%C and 0.23%C)

In the higher carbon steels, 0.16%C and higher, the transition time was harder to determine due to the droplet surface more gradually pulling away from the chill. Figure 5.49 displays corner node displacement for a 0.16%C steel with a constant h of 2.0 x 10^4 $Wm^{-2}K^{-1}$. Because it is less clear as to when to drop h, simulations were performed using transition times of both 0.04 seconds and 0.15 seconds (Case 4.1 and Case 4.2) to gain an understanding of how much the droplet is going to deform between these two values. Figures 5.50 and 5.51 compare the corner node displacement for transition times of 0.04 seconds and 0.15 seconds. In Figure 5.50 it is apparent how the decrease in h forces the rapid deformation of the surface. The figure also shows that most of the deformation takes place within 0.1 seconds after h is dropped. Figure 5.51 displays the deformation for the entire length of the simulation showing the similarity of the two runs. By using an earlier transition time of 0.04 seconds, the final N_d value is 9.58 m^{-1}, while a transition time of 0.15 seconds produces a value of 8.4 m^{-1}, as can be seen in Table 5.2, (Case 4.1 and Case 4.2 respectfully). These results show the 0.16%C steel does behave like the theoretical model, where an earlier transition time produces more final deformation. One reason for this is the absence of δ-ferrite existing below the solidus.

The 0.23%C behaves very similar to 0.16%C, in that an earlier transition time results in a higher final deformation. This can be seen by examination of Cases 5.1, 5.2, and 5.3 of Table 5.2. Figure 5.52 displays the corner node displacement and temperature at early times for all three simulations. The figure shows that an earlier transition time forces more displacement immediately after the heat transfer coefficient is dropped. The differences in the initial deformation are then carried forward throughout the simulation. Figure 5.53 displays the deformation of all three cases for the entire simulation, showing how the three cases behave almost identical, ignoring the magnitude of the initial deformation.

Figures 5.54 and 5.55 display the temperature profiles corresponding to Case 5.2, with a transition time of 0.1 seconds, for the initial and later parts of the simulation. As the droplet begins to cool, a large temperature gradient develops near the surface of the steel. This gradient starts to decrease slowly as the surface temperature drops. Because the shell is only in the γ phase, it will not go through any phase changes as its surface is reheated by the drop in h. Hence, for this grade, the shell behaves as if it were a pure material. This follows the theoretical model with the gradient at the transition time determining the amount of deformation. Because the initial temperature gradient is changing so slowly, the amount of final deformation between all three cases are within approximately 20% of each other, despite the wide range of the transition times.

5.4.6 Comparison with Experimental Results

In general the results from the model match the behavior for low carbon steel droplets very well with the results from the experiment [20]. The agreement may be fortuitous, considering the tremendous oversimplifications in the model. Figure 5.56 displays the comparison between the models predicted deformation and the amount of deformation measured by Dong et al. [20] for low carbon commercial grade steels (less than 0.23%C). Table 5.3 gives a description of the

parameters used in the droplet simulations for Figure 5.56. All the droplet simulations were performed using a constant pour temperature of 1536°C, for all carbon contents. Observation of Figure 5.56 shows the model is able to qualitatively predict the trend in the data measured by Dong et al. [20]. Quantitatively, the simulation consistently over predicts the deformation. It is also important to note the variation in measurements for the experimental values, particularly for the 0.12%C grade and below.

In the experiment and the simulation the amount of deformation decreases with carbon content between the ultra low carbon 0.003%C to low carbon 0.05%C. Dong et al. [20] suggest several reasons for the phenomena, including that the addition of an alloy lowers the solidus temperature, at which the metal begins to have strength. This result corresponds to a decrease in melting temperature and hence a decrease in the temperature gradient, (G_{Sc}). From the results of the simulation, this explanation does not entirely hold up. Figure 5.57 displays the amount of initial deformation for a 0.05%C steel with transition times of 0.025 and 0.035 seconds. The temperature gradient corresponding to a shorter transition would be slightly greater than that of a later transition time, however, the later time produces substantially more deformation. The key that separates 0.003%C from 0.05%C appears to be the 0.01 second differential in transition time and its effect on deformation. Figure 5.58 compares 0.003%C and 0.05%C for the initial part of the simulation, showing how the earlier transition time allows only a small amount of initial deformation.

Going from 0.05%C to 0.12%C the experiment and model show a rise in deformation, obtaining the most amount of deformation at 0.12%C. Dong [20] suggest this phenomena is due to the thermal expansion between the δ to γ phase transformation. Below 0.10%C more fraction of initial temperature gradient is diminished before the δ begins to transform to γ. Above 0.10%C there exists less amount of δ that is to be transformed to γ during the process of diminishing the initial temperature gradient. This same argument also applies to the amount of inelastic

deformation occurring in the δ phase. For the steel above 0.10%C the presence of a shorter δ phase will result in less inelastic deformation, and hence a shorter transition time and thus, the higher initial deformation.

In the simulations for 0.12%C, the initial shell deformation is occurring 0.08 seconds after the surface begins to reheat due to the change in h. For 0.003%C and 0.05%C the initial deformation is occurring right when the surface temperature begins to reheat. For 0.12%C the reason the deformation is not occurring after the rise in surface temperature may be due to the closeness in temperature of the δ to γ phase change and the surface temperature of the shell at the time when h is dropped. Because of this, the entire shell cools through the δ to the γ phase change at one time causing an enormous amount of deformation. The rate of deformation experienced by the shell is also more gradual due to the reduced heat transfer coefficient. This result is in disagreement with Dong [20], as the start of deformation for this grade occurs much later than the other grades with lower carbon content.

In the 0.16%C and higher steels, the steep initial deformation is not observed with the constant high h. Instead, the deformation is gradual until h is decreased, after which a large amount of deformation will begin. Without a decrease in h, the gap remains very small even for the longer transition times. This long time allows temperature gradients to drop before the bending gets started, so the amount of final deformation is less. For both the 0.16%C and 0.23%C steels an earlier transition time produced more initial deformation. This initial deformation would then result in a higher amount of final deformation. Because there are no significant solid phase transformations occurring, a large change in transition time produces only small changes in the amount of final curvature. Hence, these grades performed more like the theoretical model, in which a shorter transition time results in an increased amount of curvature.

Using the same modeling approach, attempts where also made to predict the concave deformation (Figure 5.21b) observed by Dong et al. [20] in the higher carbon steels. The simulations were unable to predict a final negative curvature. One reason for this may be due to the increased droplet size. The concave curvature was observed by Dong in high carbon, larger 8 gram sized droplets. The increased size would result in more spreading of the droplet, something the simulation is unable to model.

5.4.7 Droplet Discussion

This work is a crude first attempt to quantitatively predict the shape of solidified surfaces. The encouraging results of the work suggest that the characteristic curved bottom shape observed in Figure 5.21a is consistent (both qualitatively and quantitatively) with thermal stress generation in a solidifying droplet in the absence of friction.

The simulation results suggest a high cooling rate is doubly detrimental to shell bending in peritectic steels. In addition to the steep temperature gradients produced, cooling rates of more than 5000°C/s are reported to induce direct transformation to metastable cellular austenite [67]. When the resulting surface austenite layer reheats a few milliseconds later, it transforms to delta and expands. Combined with a rigid subsurface layer, the result would be a tremendous increase in bending, relative to other grades.

Case	%C	h_1 (W/m^2K)	h_2 (W/m^2K)	t_h (s)	N_d (m^{-1})	time (s)	surf. T (°C)	Est. N_d * (@100°C)
1.0	0.003	20000	20000	N/A	17.30	8.7	107	17.3
1.1	0.003	20000	5000	0.035	9.05	23.1	113	9.1
1.2	0.003	20000	2000	0.035	9.28	19.0	476	9.7
1.3	0.003	20000	5000	0.05	13.20	1.0	1218	17
2.0	0.05	20000	20000	N/A	13.60	0.1	1591	21
2.1	0.05	20000	5000	0.025	5.65	10.0	518	5.9
2.2	0.05	20000	2000	0.025	2.68	30.0	221	2.7
2.3	0.05	20000	5000	0.035	14.30	0.1	1425	17
3.0	0.12	20000	20000	N/A	9.11	0.1	1118	11
3.1	0.12	20000	5000	0.015	11.99	22.5	100	12.0
3.2	0.12	20000	5000	0.017	10.71	1.0	1194	13
4.0	0.16	20000	20000	N/A	2.60	1.0	596	3.1
4.1	0.16	20000	5000	0.04	9.58	20.0	153	9.6
4.2	0.16	20000	5000	0.15	8.04	18.5	183	8.1
5.0	0.23	20000	20000	N/A	0.75	0.2	953	1.6
5.1	0.23	20000	5000	0.05	8.88	22.5	110	8.9
5.2	0.23	20000	5000	0.1	8.57	22.0	115	8.6
5.3	0.23	20000	5000	0.3	7.08	22.0	110	7.1

*Estimated N_d for a surface temperature near 100°C based on experience

Table 5.2. Simulation parameters and results for steel droplet simulation Cases

%C	Case	h_1 (W/m^2K)	h_2 (W/m^2K)	t_h (s)	N_d (m^{-1})	Superheat (°C)	Liquidus (°C)	Solidus (°C)	δ to γ* (°C)
0.003	1.1	20000	5000	0.035	9.1	0.24	1535.76	1534.63	1393.87
0.05	2.1	20000	5000	0.025	5.7	4.0	1532.06	1513.22	1423.01
0.12	3.1	20000	5000	0.015	12.0	9.5	1526.54	1495.00	1466.64
0.16	4.1	20000	5000	0.040	9.6	12.6	1523.38	1495.00	1491.52
0.23	5.3	20000	5000	0.050	8.9	18.1	1517.87	1485.34	N/A

*Transition temperature from delta-ferrite to austenite (%δ=10%)

Table 5.3. Simulation parameters and results of simulations shown for Figure 5.56

The wavy final bottom shapes observed after solidification of larger droplets or with higher pressure might be caused by fluid overflowing the initially solidifying region. The liquid surface at the edge of the droplet is subject to very high temperature gradients, so surface tension effects including Marangoni-driven flow and dynamic changes in contact angle could greatly affect droplet spreading when liquid first contacts the chill. The direction of these forces is very sensitive to small composition changes, such as low S levels in steel. These phenomena together may cause the solidifying surface of a large volume of metal to behave mechanically like a series of barely connected droplets.

This mechanism is likely complicated by the distribution or shortage of nucleation sites, intermittent surface contact and sticking adhesion, and mechanical bending associated with the nonuniform heat transfer. Prediction of the critically-important convection heat transfer coefficient is a difficult coupled problem that is time and position dependent. In addition to the size of the gap, h depends on the thermal properties of the medium that fills the gap, the condition of the chill surface, and how well the molten metal initially contacts the chilled surface, which may depend on the surface tension (which may in turn vary with superheat and

composition). The anisotropic properties of columnar dendrites will produce different mechanical behavior in the x and y directions. Finally, quantitative prediction of surface shape also requires proper consideration of nonequilibrium phase transformation, undercooling, micro segregation, and other effects such as gas evolution and entrapment. Clearly, much work remains to be done before the shape of solidified surfaces can be predicted with confidence.

5.4.8 Droplet Validation Problem Conclusions

The transient finite-element model has been applied to predict temperature and thermal distortion of a steel droplet solidifying against a chill plate. The findings suggest that:

1) Model predictions of final surface shape of the droplet agree surprisingly well with measurements from Dong [20] for several different carbon contents.
2) The observed drop in heat transfer coefficient, and corresponding rise in surface temperature appear to coincide with the formation of a critical thickness of solidified metal with sufficient strength to bend away from the chilled surface.
3) Surface shape evolves almost completely within the first 0.03 - 0.2 seconds of the droplet impacting the chill plate. The shorter times apply to lower carbon contents, which produce a strong thin shell more quickly
4) The increase in surface temperature observed in experiments might not be due entirely to recalescence related to delayed nucleation and latent heat evolution. Surface reheating is predicted even with this equilibrium solidification model, when the surface heat transfer coefficient drops suddenly.
5) Creep and bending relax almost all of the stresses until the droplet is completely solid.
6) A sudden decrease in the gap heat transfer coefficient (h), generally causes more bending when it occurs earlier, unless phase transformations reverse. This means that for high carbon steels, faster transition from high to low h, causes more deformation. For low carbon steels, a faster transition causes less deformation, due to less phase transition reversal effect.
7) The 0.12%C steel is predicted to have the most bending and consequent curvature of the bottom surface, and 0.05%C is predicted to have the least amount of curvature.
8) A very fine mesh and time step are needed to obtain grid-independent model predictions.

5.5 Model Validation Conclusions

This two-dimensional fixed-grid finite-element model has displayed its ability to accurately model steel solidification phenomena. The present work, along with the work by Zhu [2], which validated the mathematical consistency of the model, prove the model is capable of simulating both the mechanical and thermal analysis of steel solidification. Based on the simulation of various steel solidification occurrences, several conclusions can be made regarding the thermo-mechanical model.

1) A benchmark test problem for thermal-mechanical analysis of solidification with a known analytical solution has been developed, using a highly nonlinear constitutive equation to create a severe numerical challenge. This test problem is ideal to compare finite-element models for solving mechanical problems with solidification.
2) The constitutive relations used in the model have been shown to accurately match experimental mechanical data. The combination of Model III and the power law model is able to accurately predict the mechanical behavior of steel for a wide range of conditions.
3) Using a simplified mesh, the model was able to accurately predict the stress development of a submerged split chill tensile (SSCT) test. The model was able to predict the strength of the steel up until the point where non-uniform necking began weakening the steels strength.
4) An extensive amount of work was done using the model to predict the final deformation of steel droplets solidifying on a copper chill. While the final results of the work may be fortuitous, they do suggest the model is able to accurately predict the mechanical behavior.

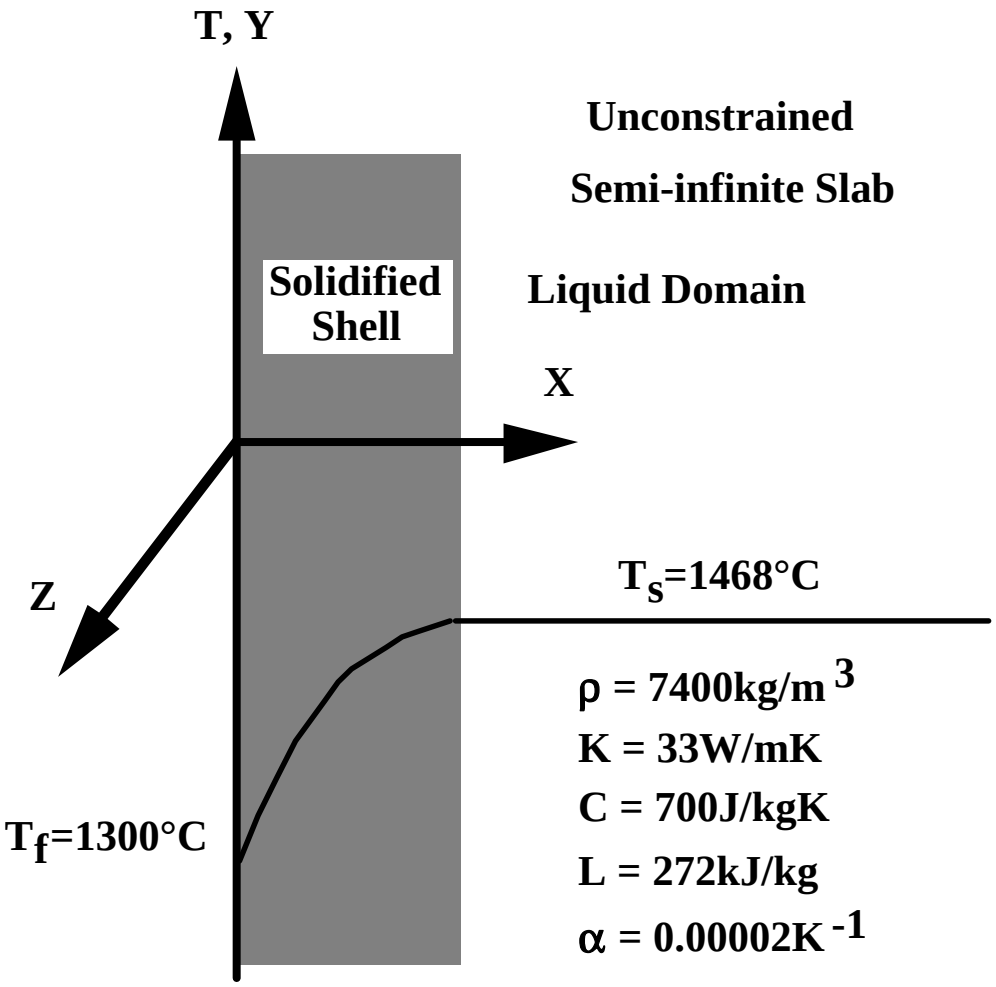

Figure 5.1. One-dimensional chilled slab solidification

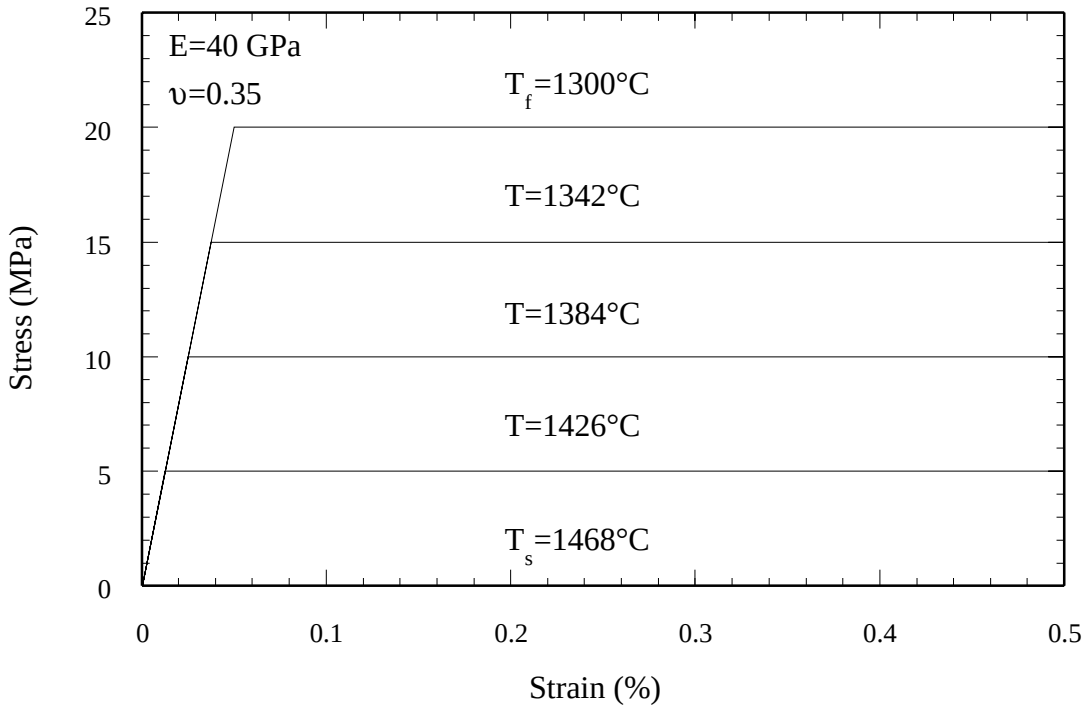

Figure 5.2. Constitutive behavior assumed in solidification test problem

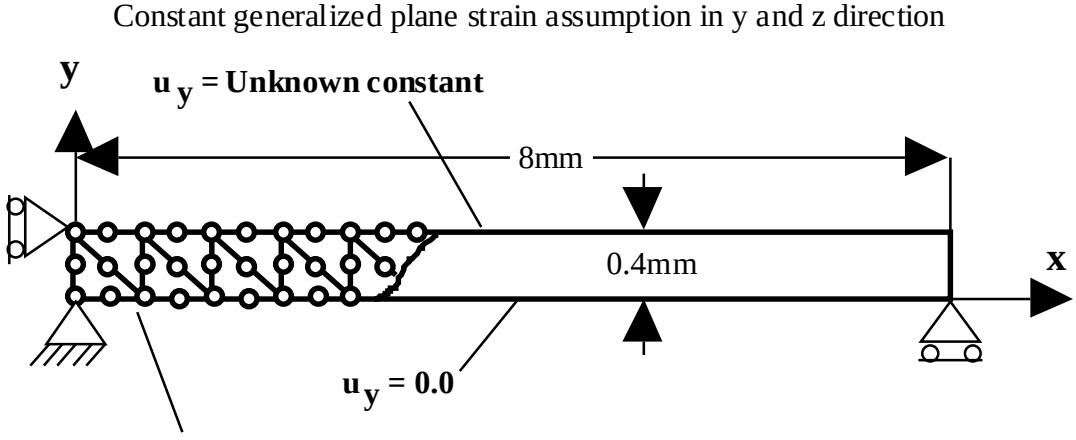

Figure 5.3. Finite element model of one-dimensional solidification test problem

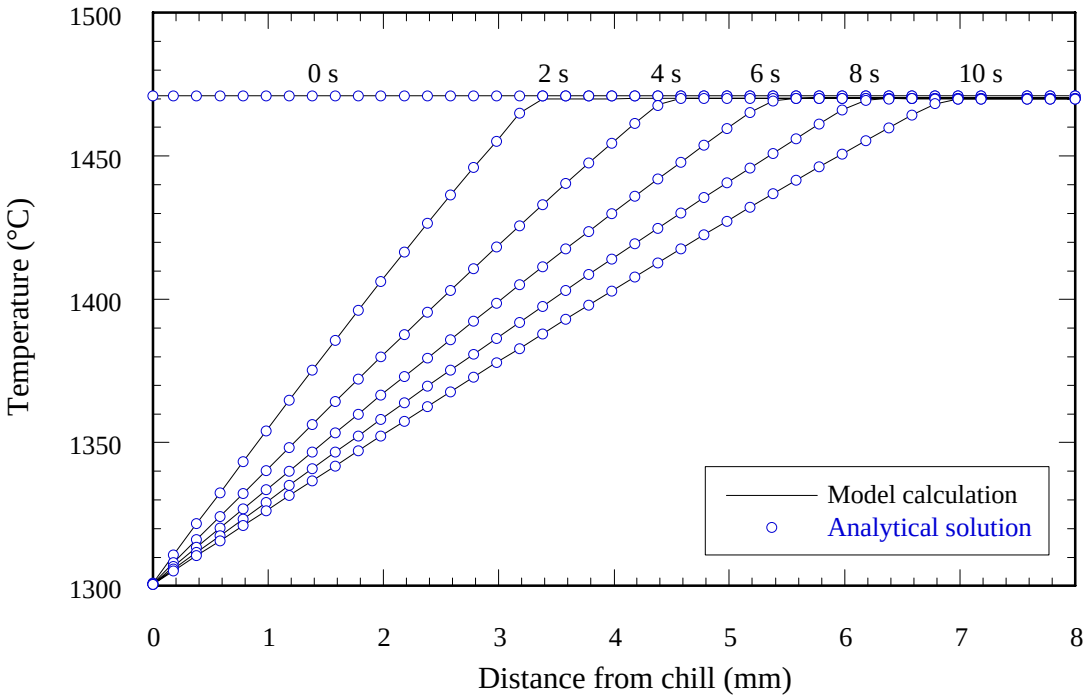

Figure 5.4. Temperature distribution of slab for one-dimensional solidification test

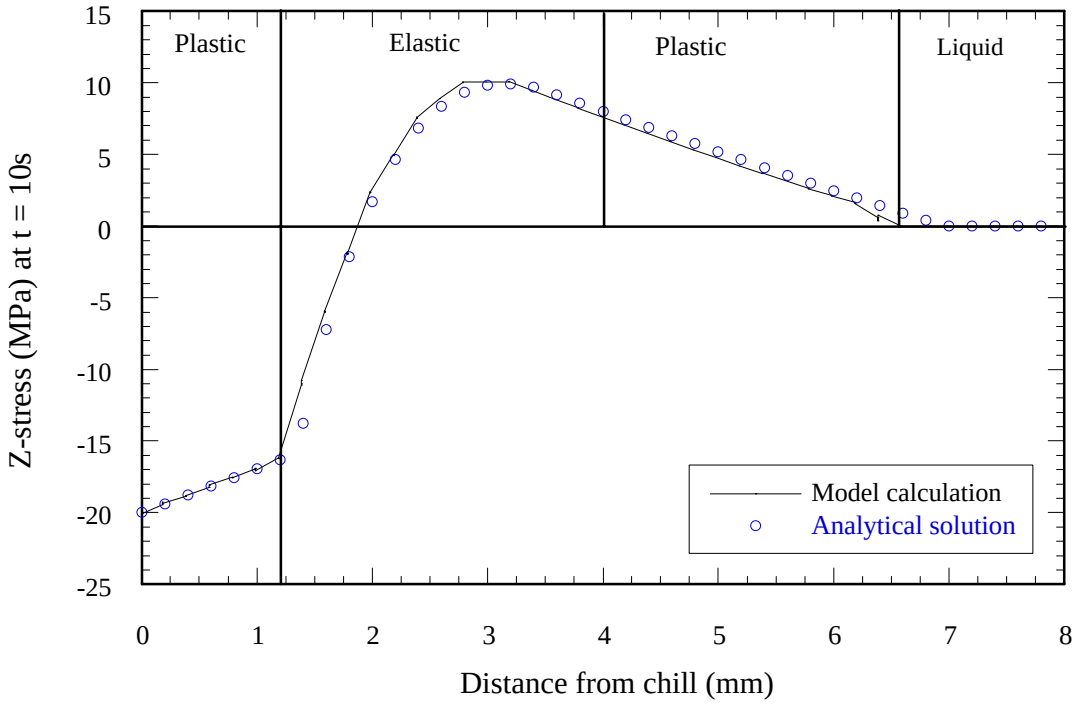

Figure 5.5. Stress distribution through slab of one-dimensional solidification test

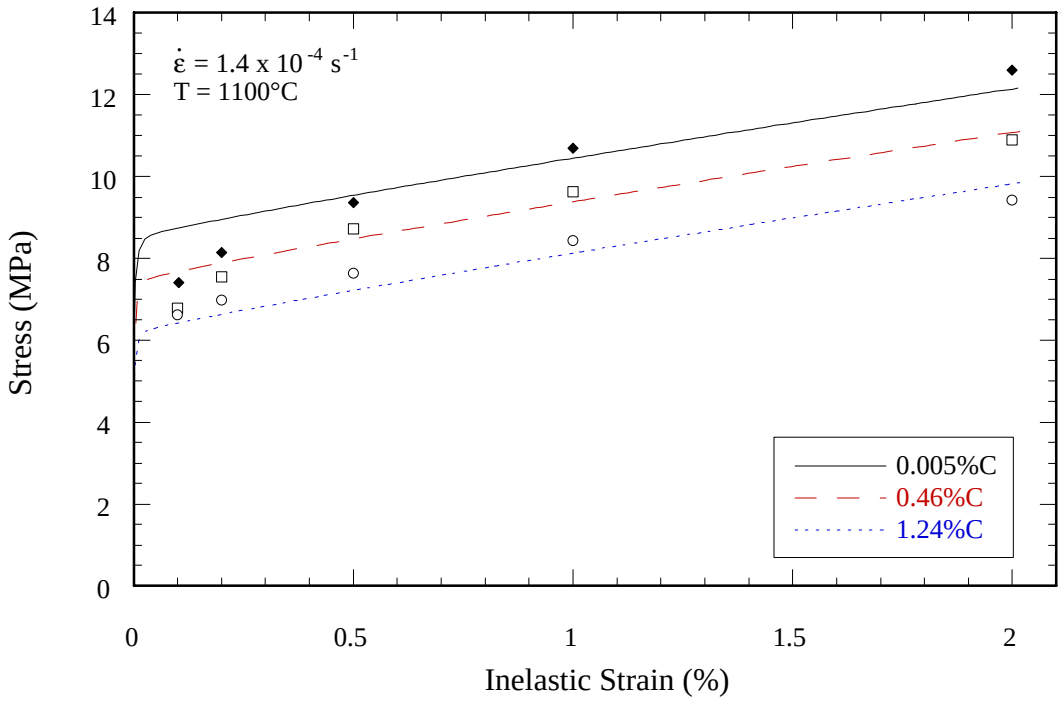

Figure 5.6. Tensile test curves calculated with Model III for various carbon content (Compared with Wray data [63])

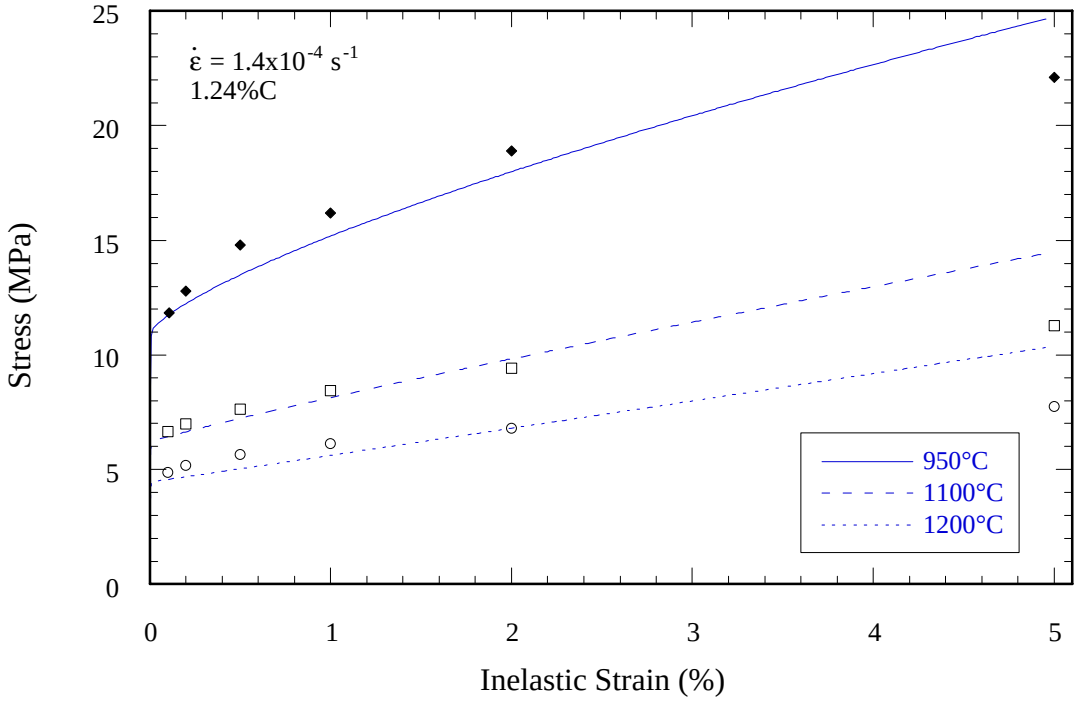

Figure 5.7. Tensile test curves calculated with Model III at different temperatures (Compared with Wray data [63])

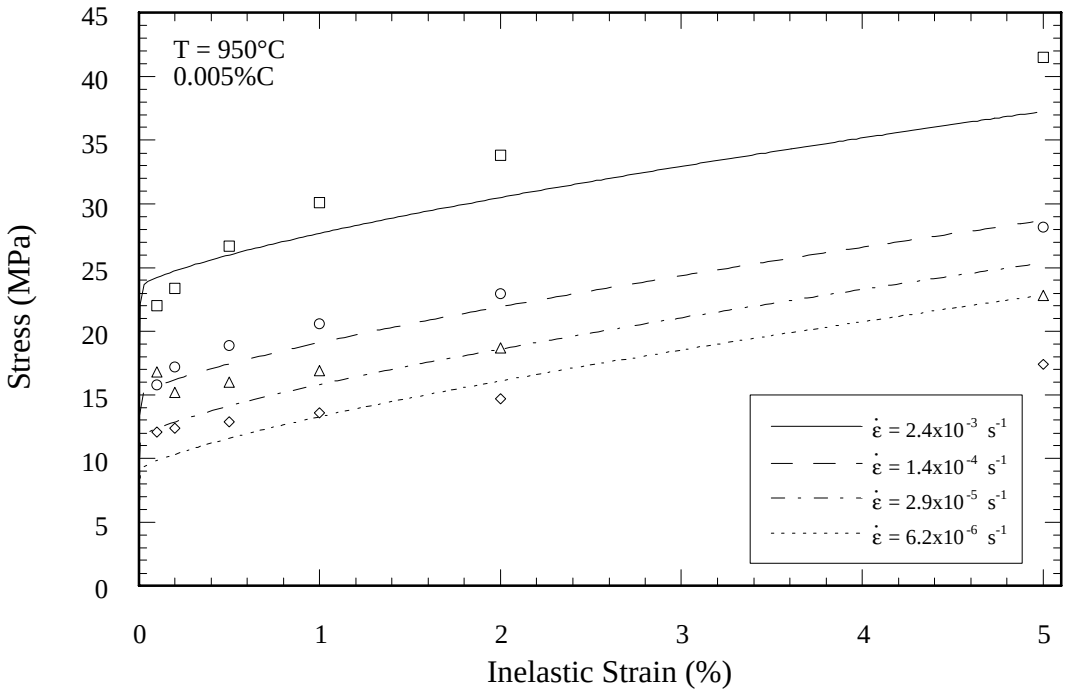

Figure 5.8. Tensile test curves calculated with Model III at different strain rates (Compared with Wray data [63])

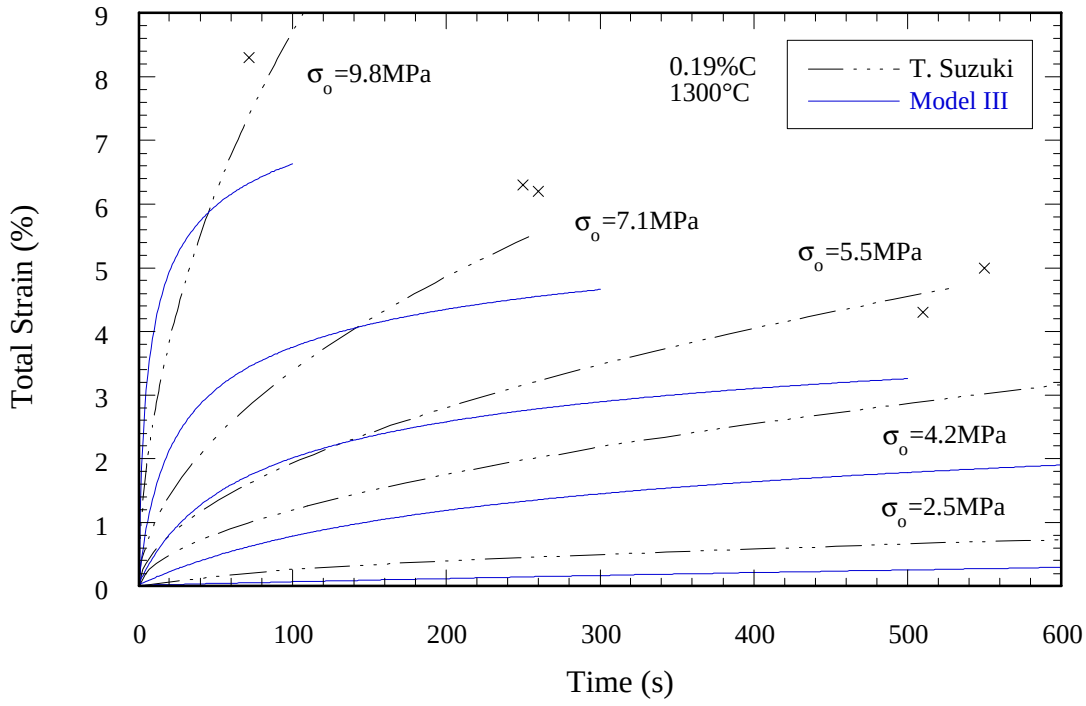

Figure 5.9. Creep test curves calculated with Model III at 1300°C (Compared with Suzuki data [7])

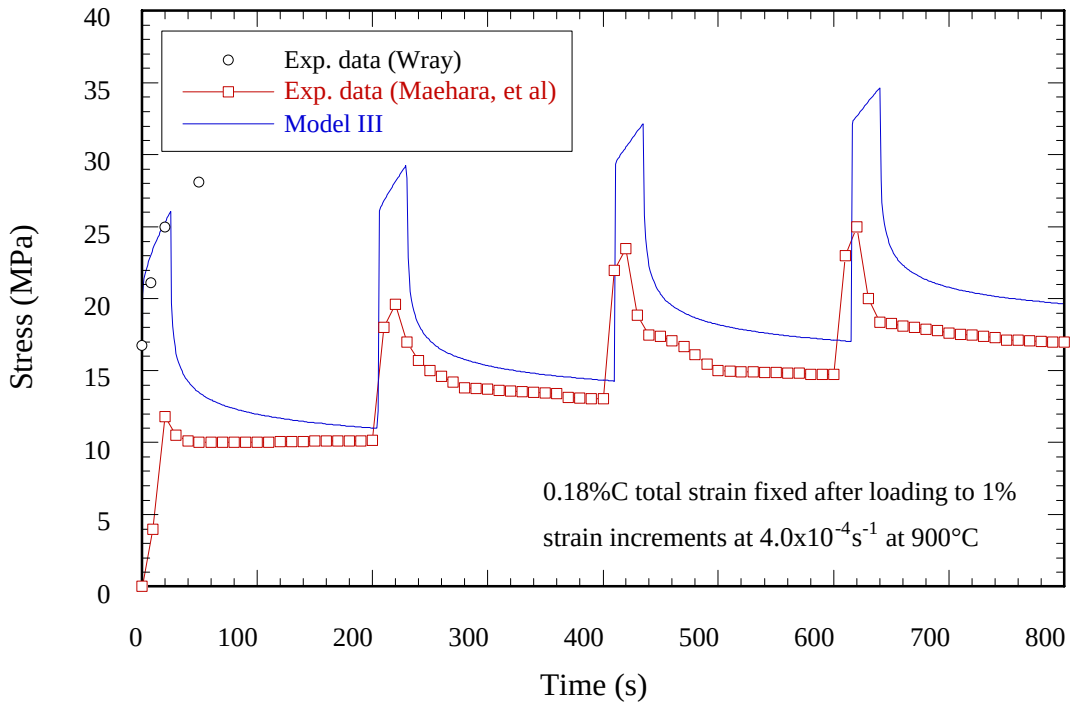

Figure 5.10. Stress relaxation test response of Model III
(Compared with experimental data [63, 64])

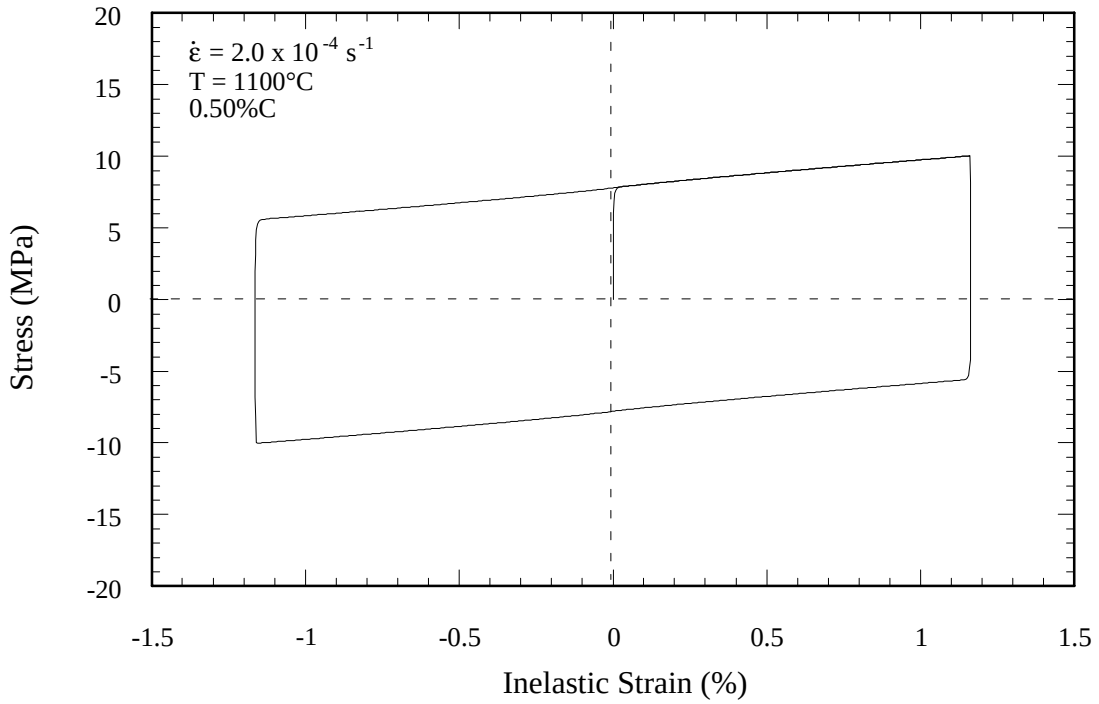

Figure 5.11. Cyclic loading response of Model III with ± 1.2% strain cycles

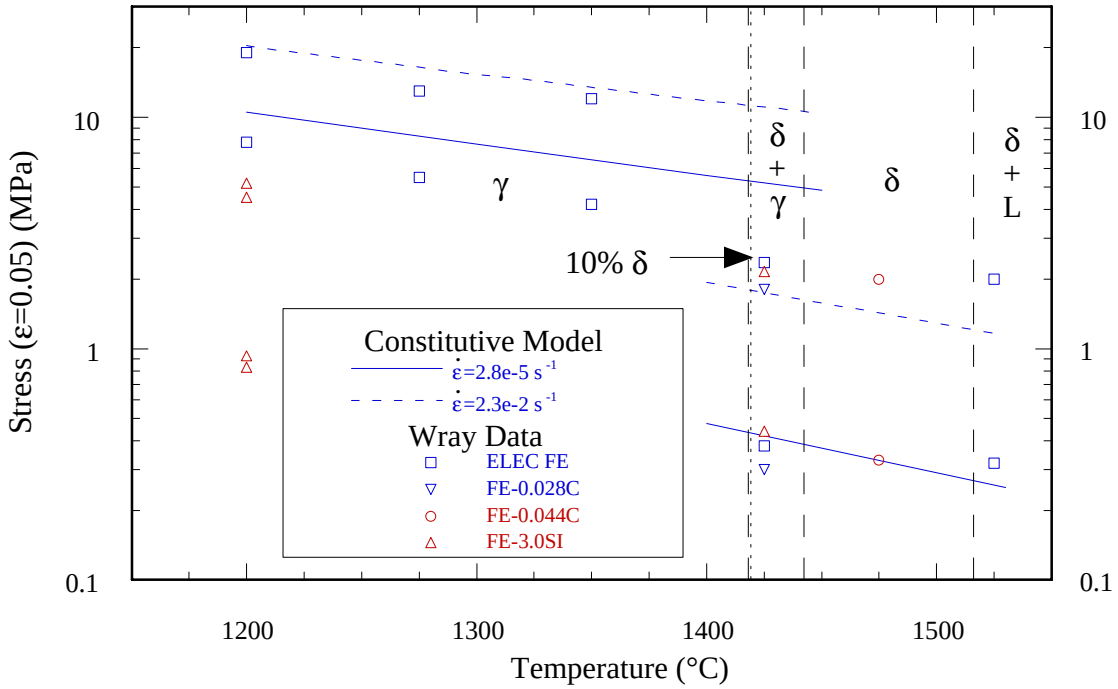

Figure 5.12. Constitutive model comparison showing δ-ferrite is weaker than γ (Compared with Wray data [63])

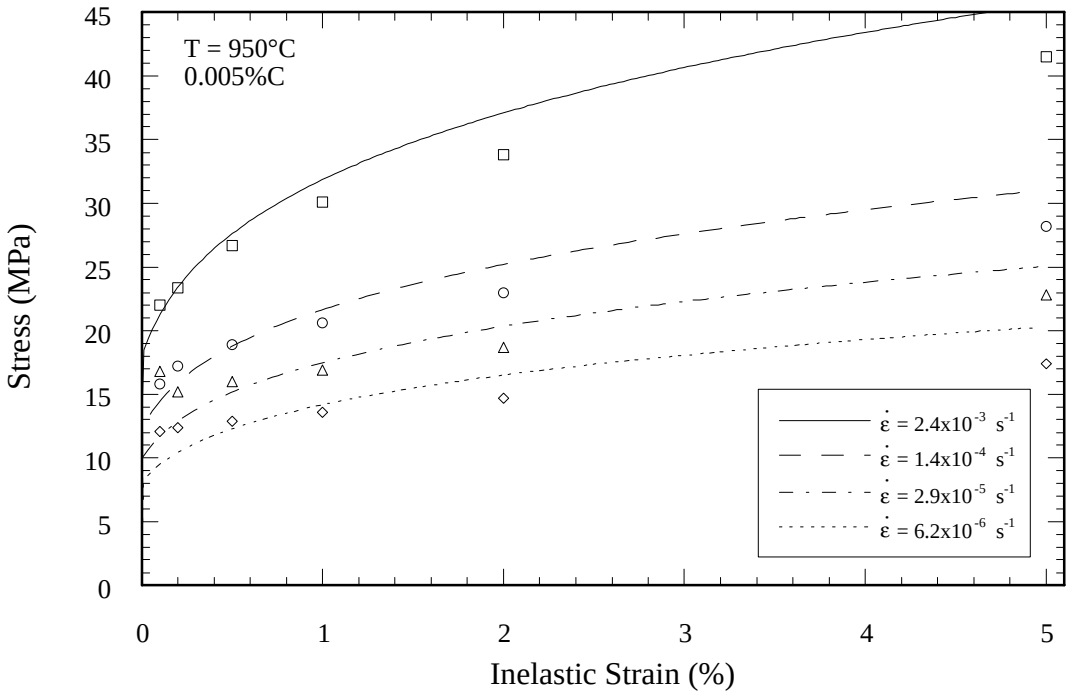

Figure 5.13. Tensile test curves calculated with power law at different strain rates (Compared with Wray data [63])

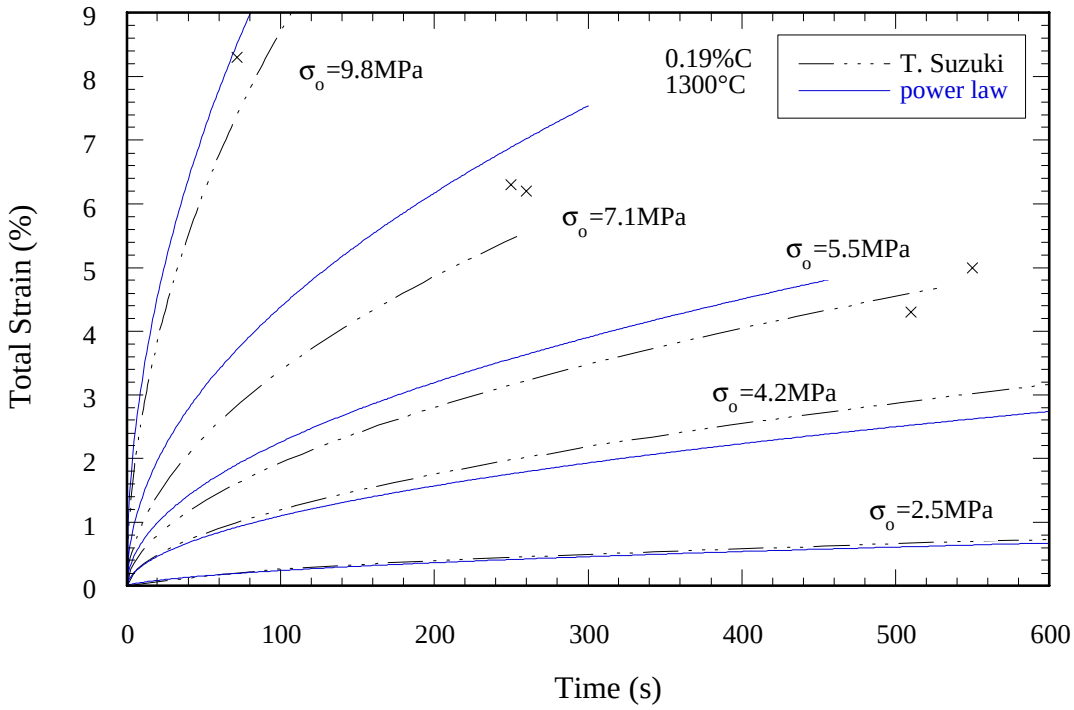

Figure 5.14. Creep test curves calculated with power law at 1300°C (Compared with Suzuki data [7])

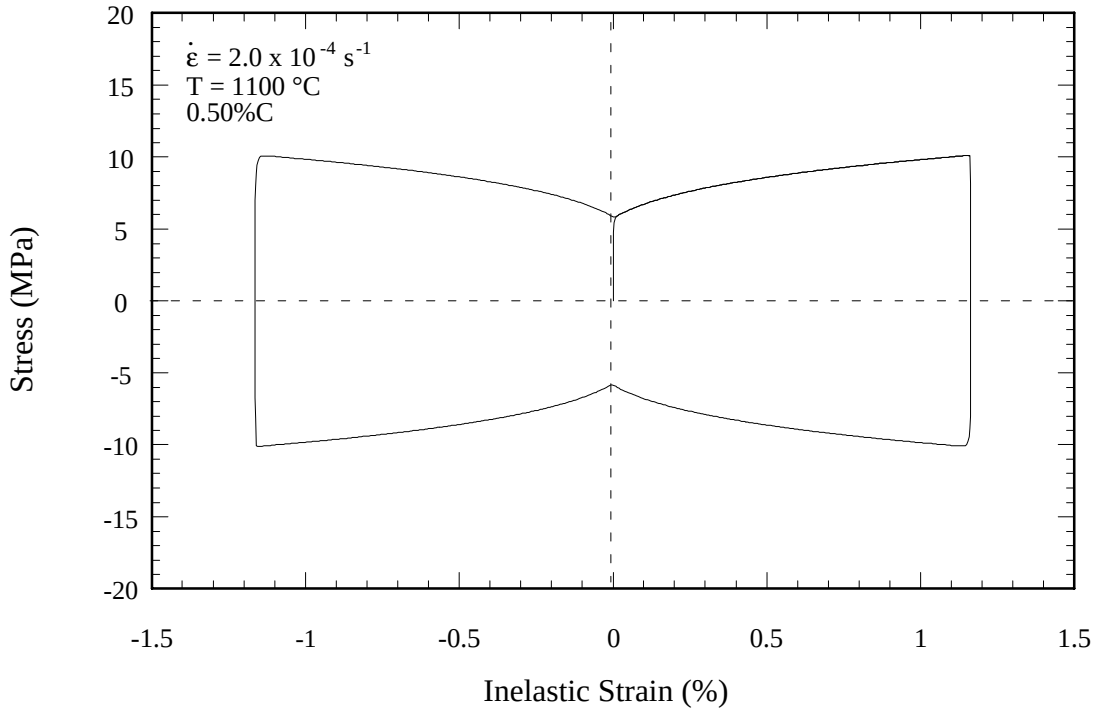

Figure 5.15. Cyclic loading response of power law with ± 1.2% strain cycles

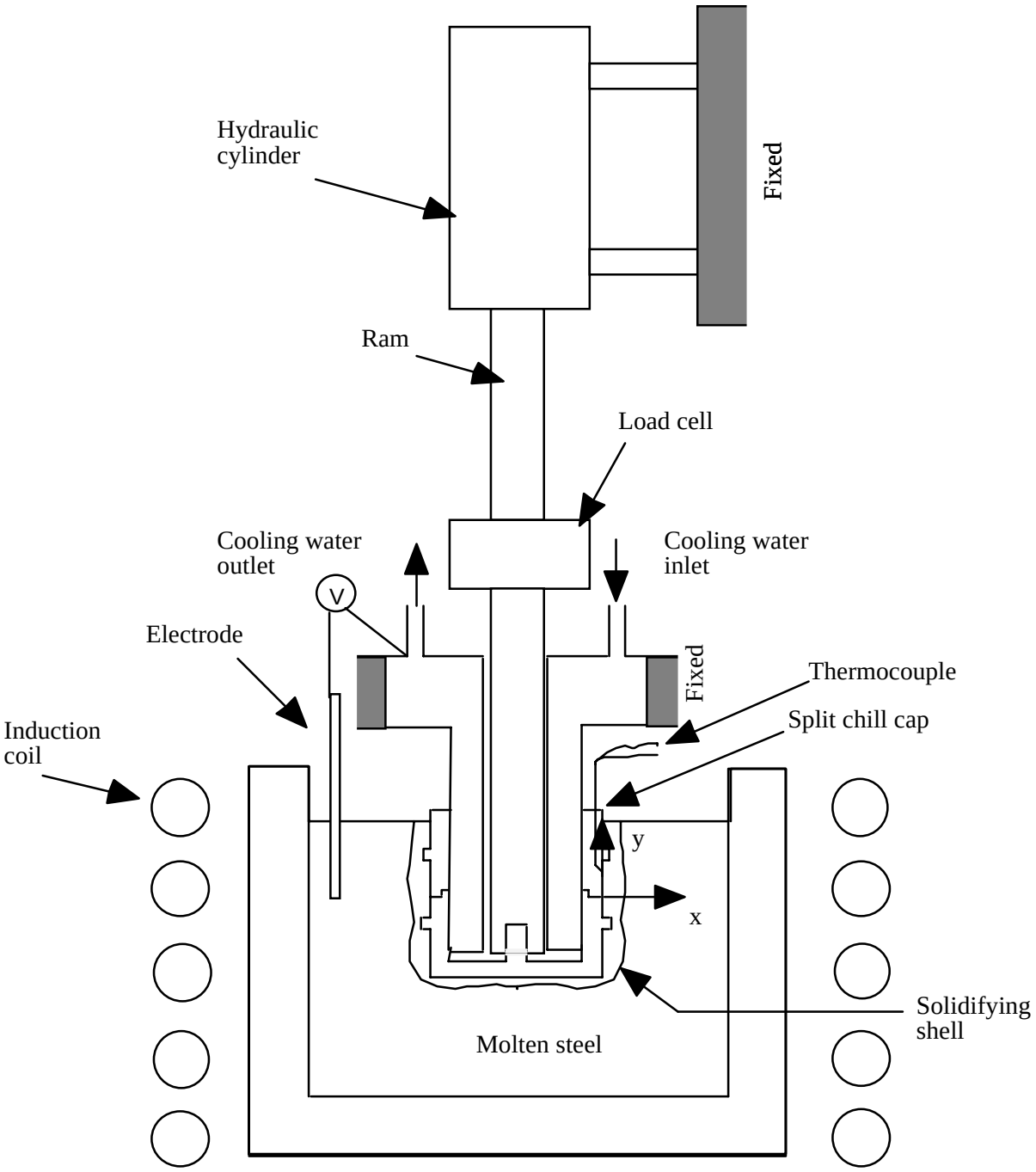

Figure 5.16. Diagram of Submerged Split Chill Tensile (SSCT) apparatus

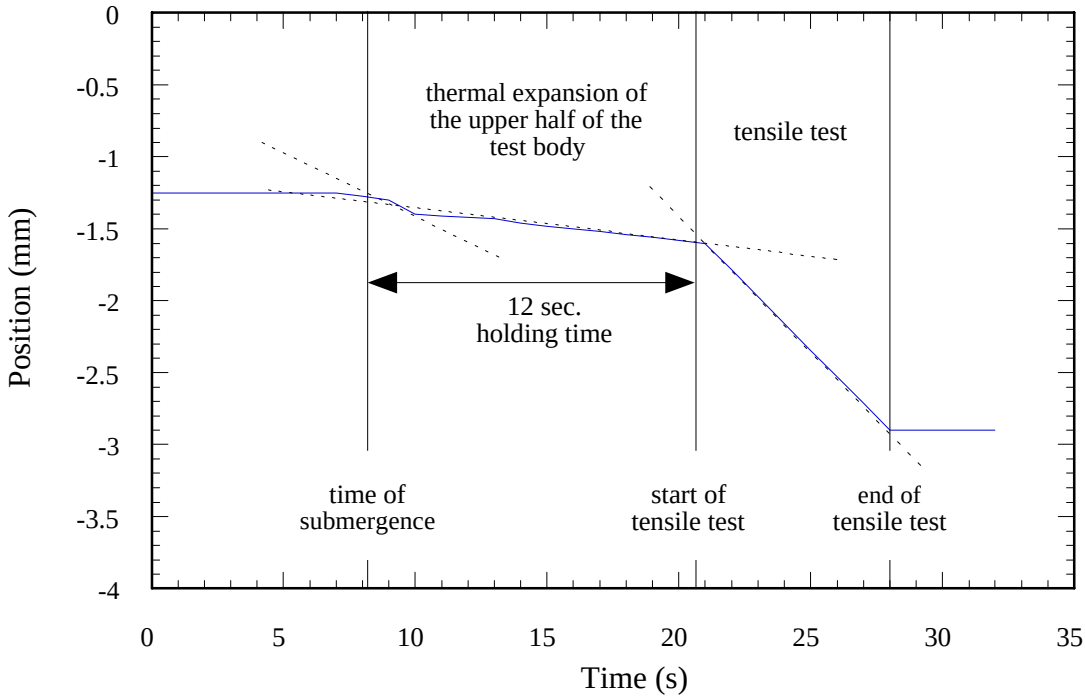

Figure 5.17. Graph displaying data and time sequence for a typical SSCT test

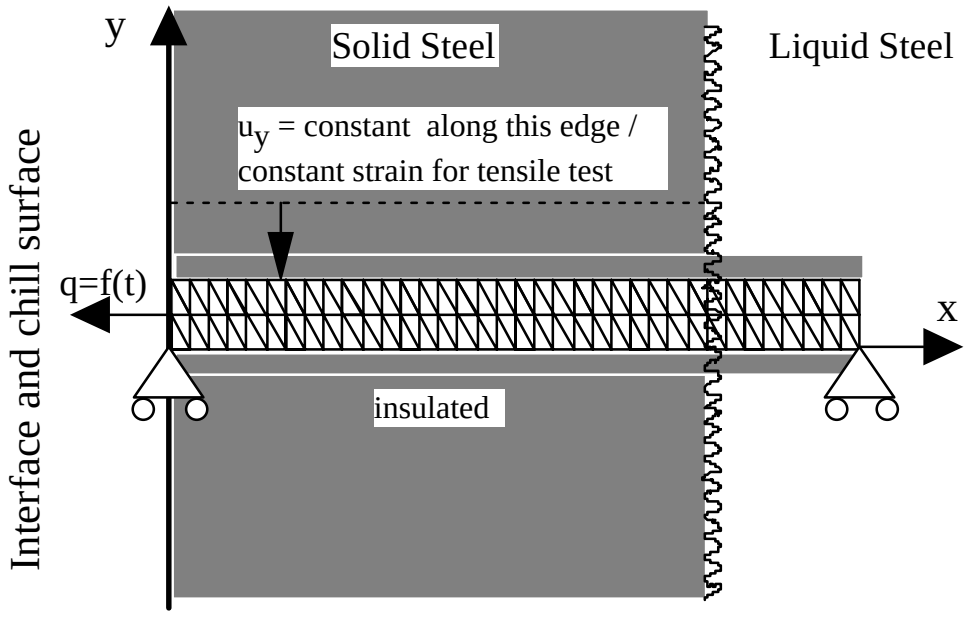

Figure 5.18. Finite element mesh used to model SSCT test

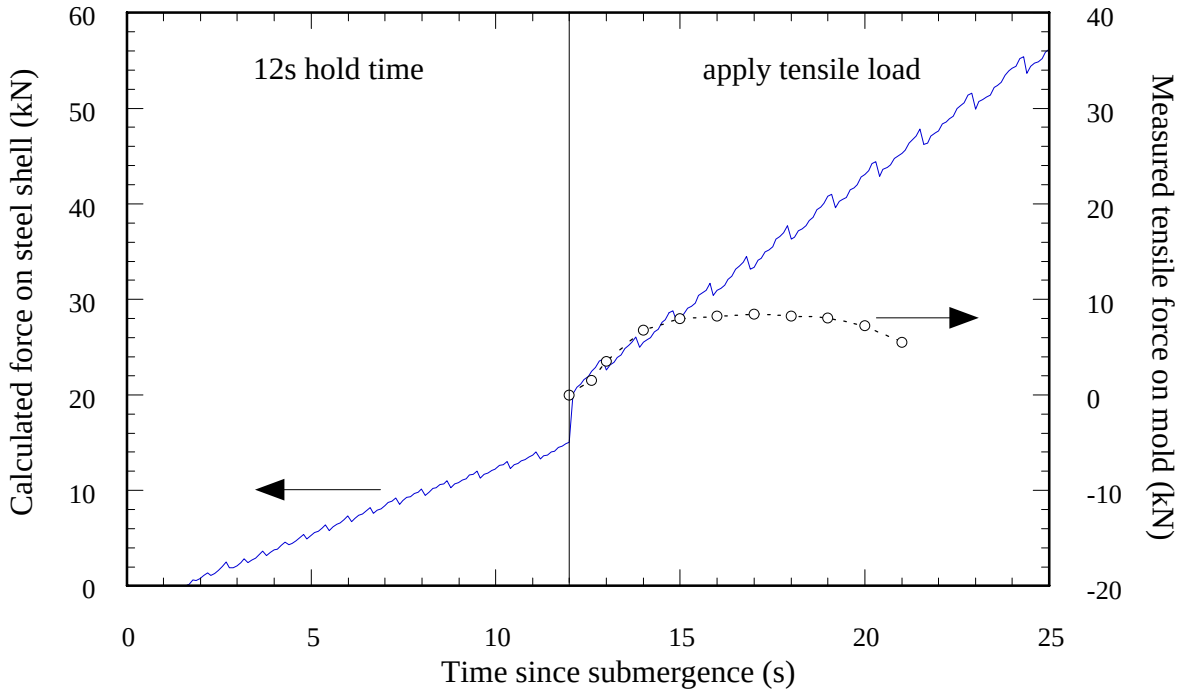

Figure 5.19. Comparison of experimental and simulation results of SSCT test

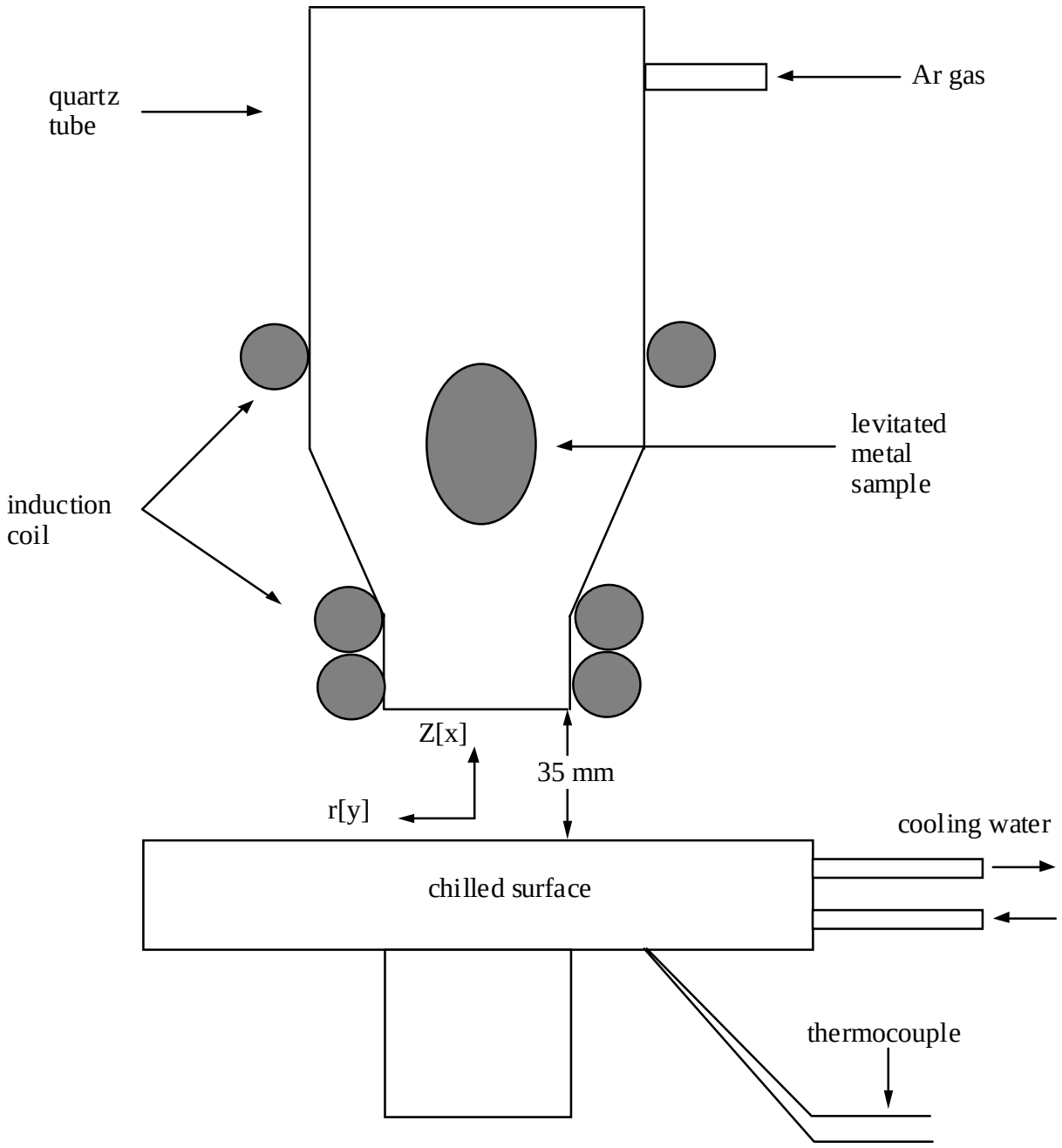

Figure 5.20. Schematic of droplet quenching apparatus used by Dong et al. [20]

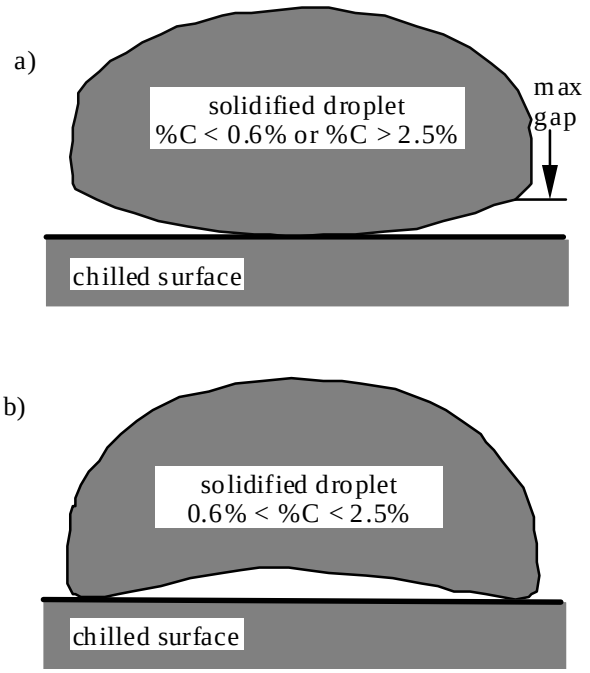

Figure 5.21. Schematic of deformed droplets showing representative shapes

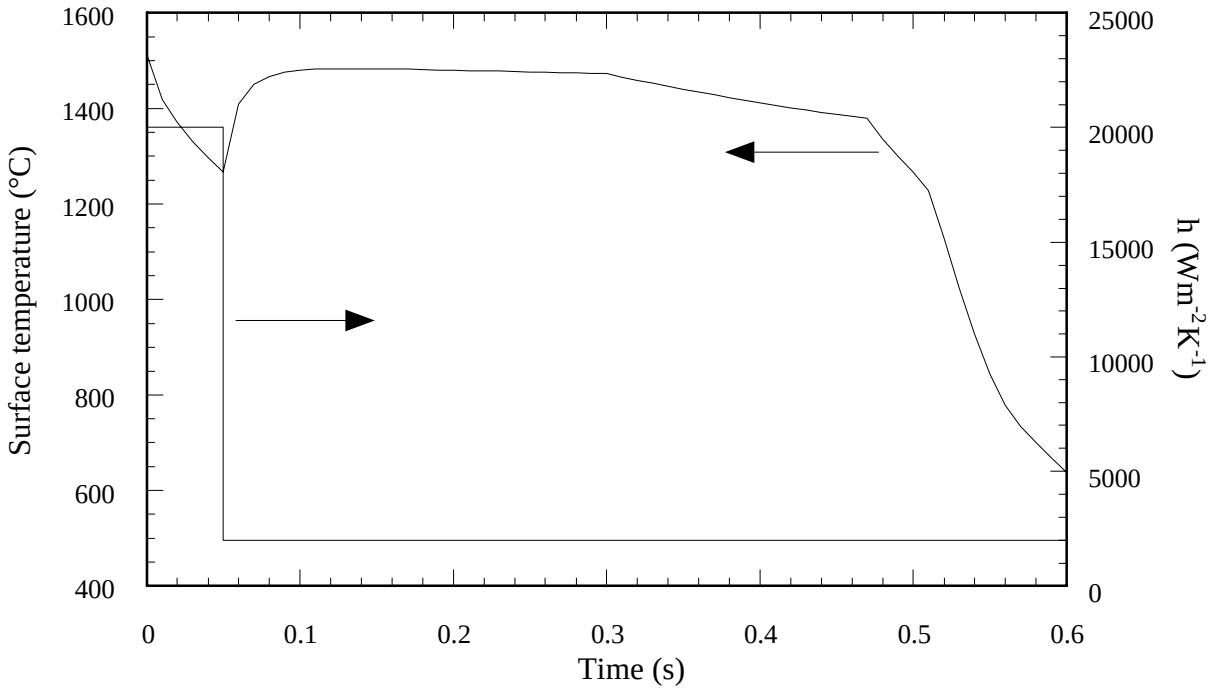

Figure 5.22. Estimation of droplet surface temperature and heat transfer coefficient

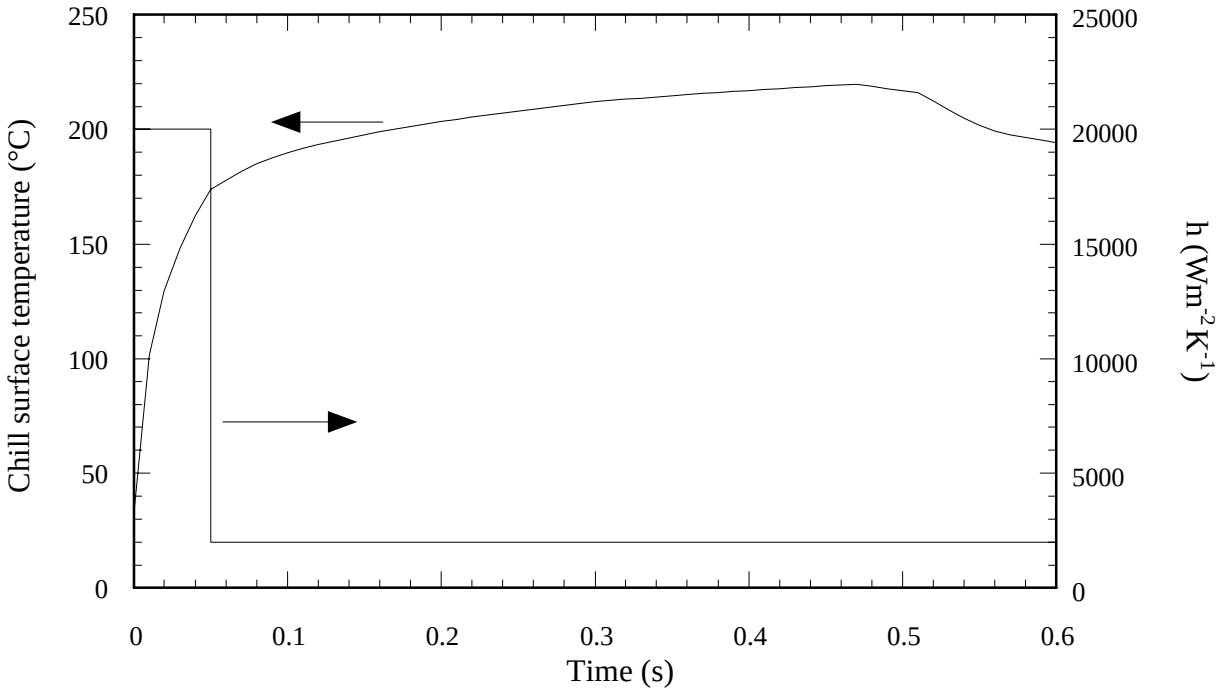

Figure 5.23. Estimation of surface of the copper chill in reaction to droplet

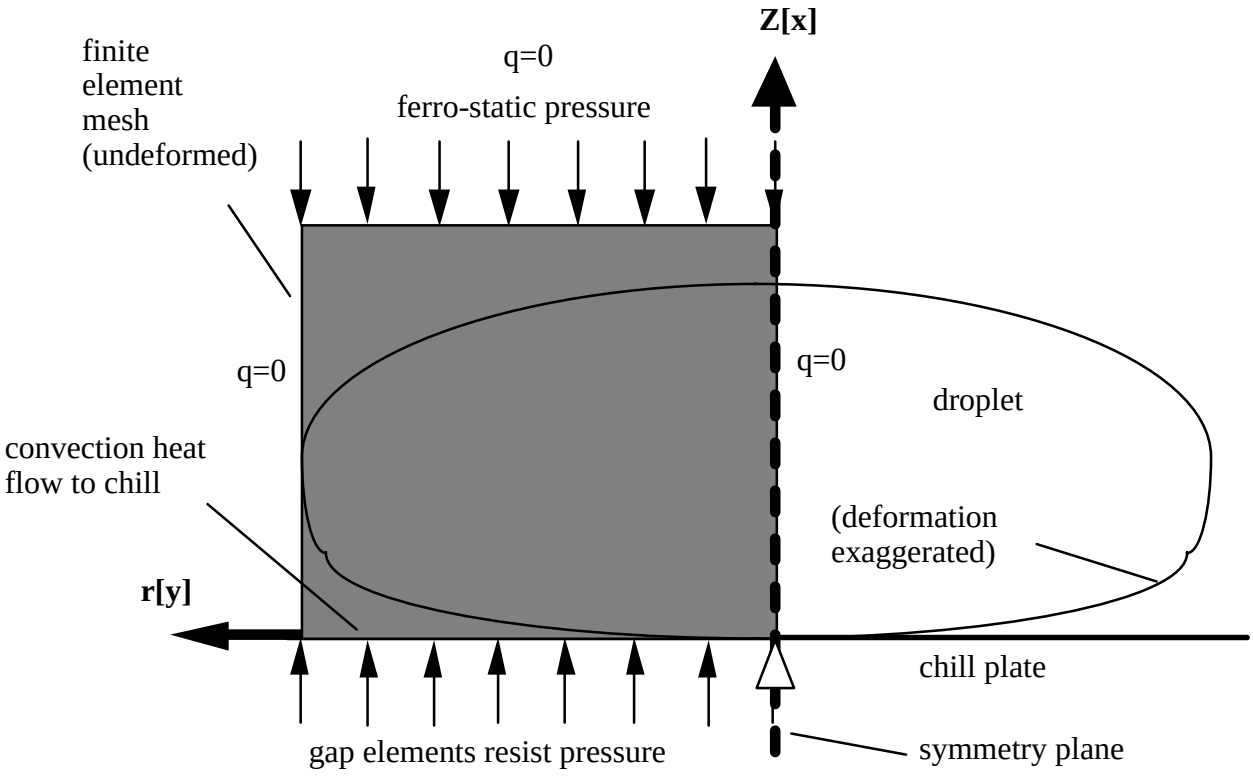

Figure 5.24. Schematic of model domain and boundary conditions for simulations

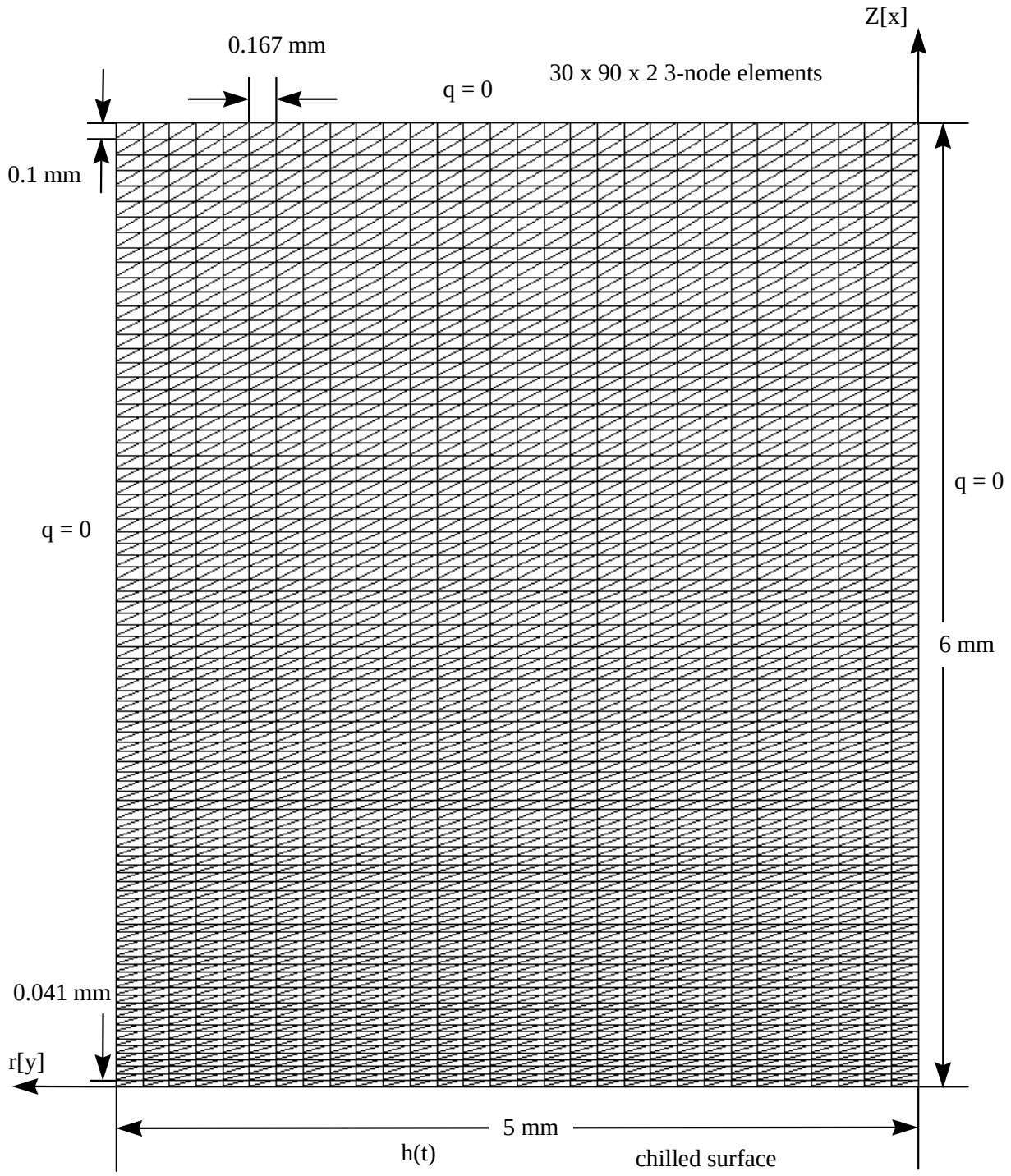

Figure 5.25. Schematic of mesh to model droplet, showing dimensions

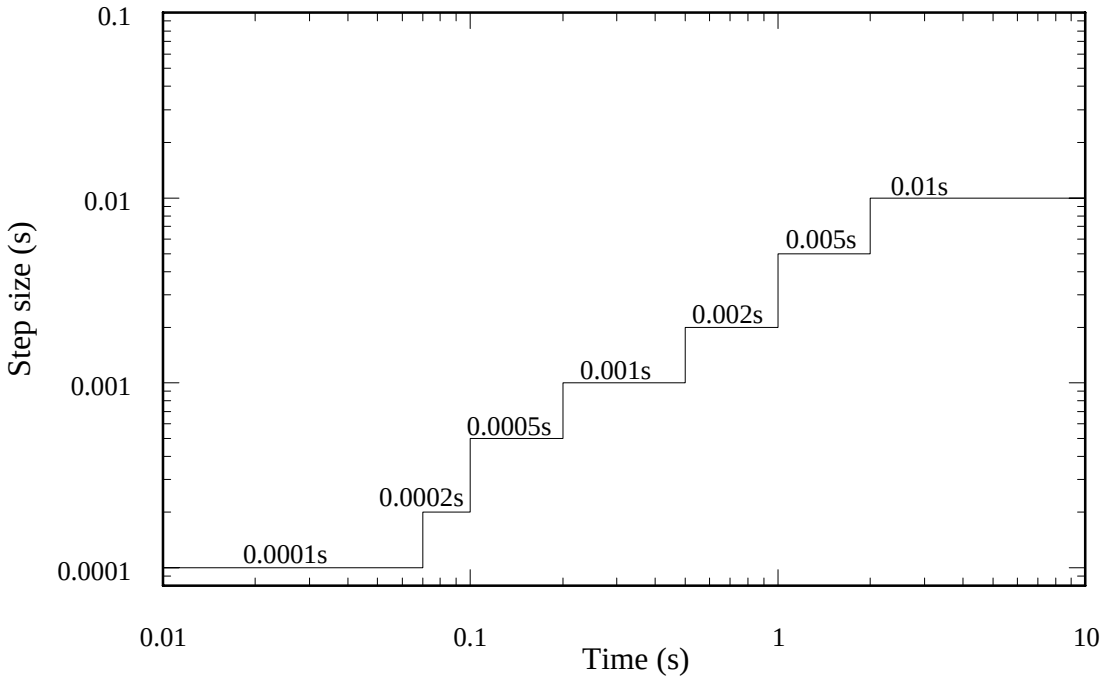

Figure 5.26. Graph displaying time history of Δt for droplet simulations

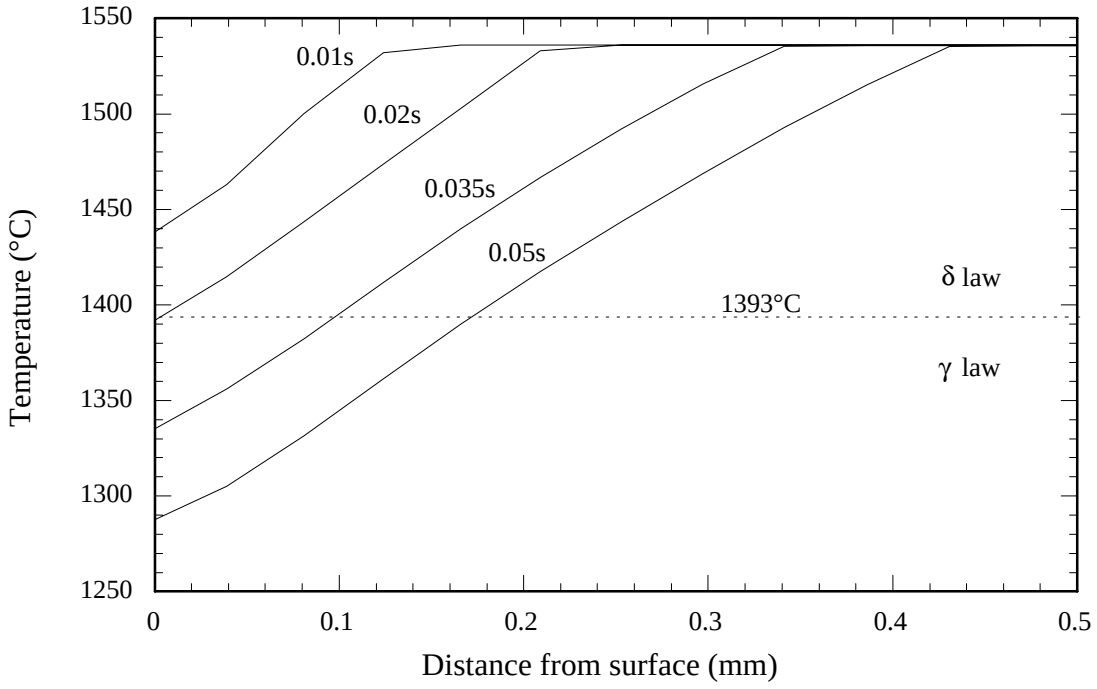

Figure 5.27. Temperature slice history for early times of 0.003%C with a constant h

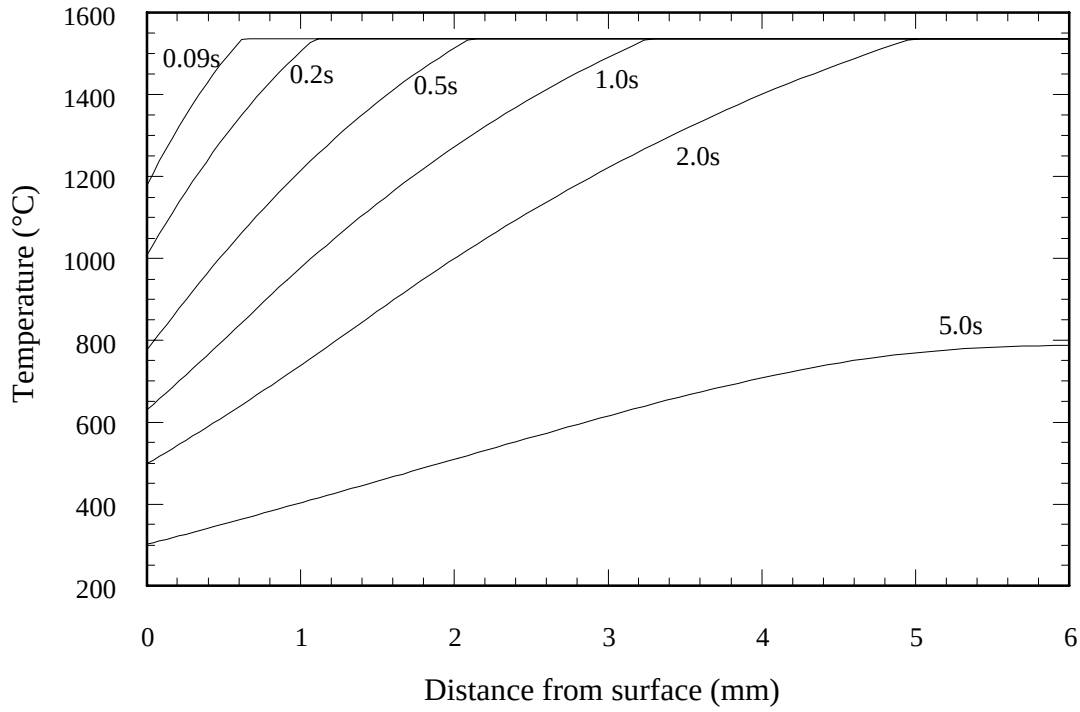

Figure 5.28. Temperature slice history for later times of 0.003%C with a constant h

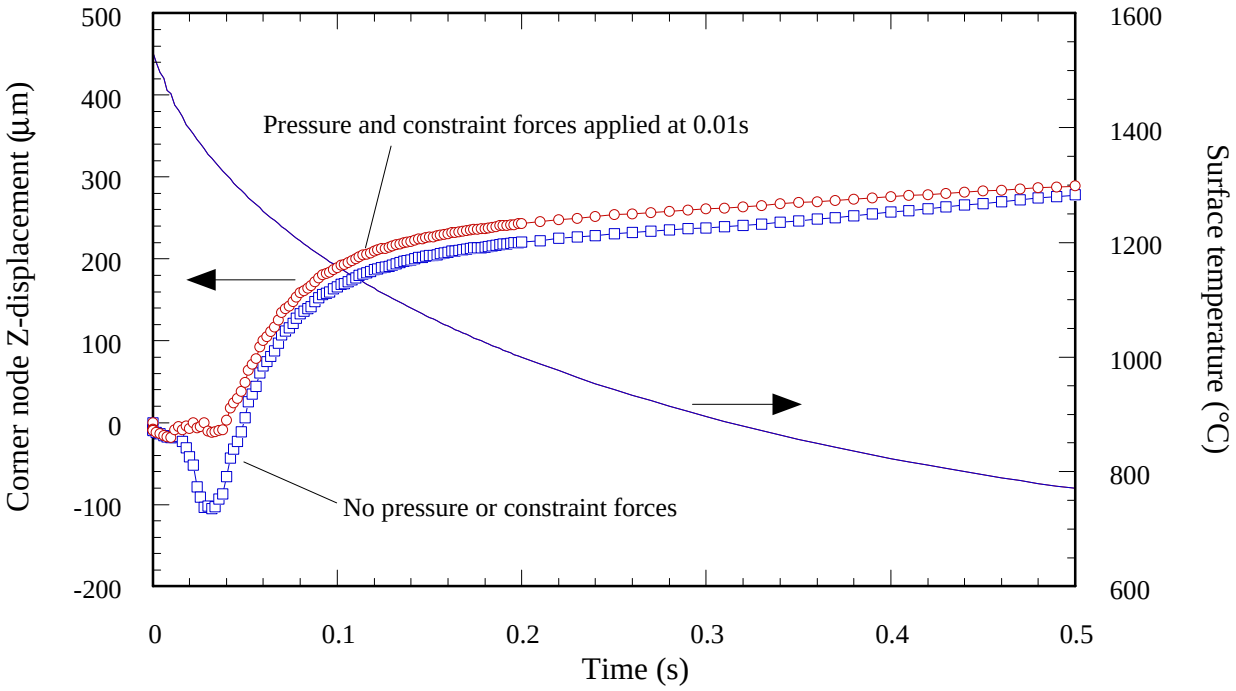

Figure 5.29. Deformation using constant h, comparing pressure boundary conditions

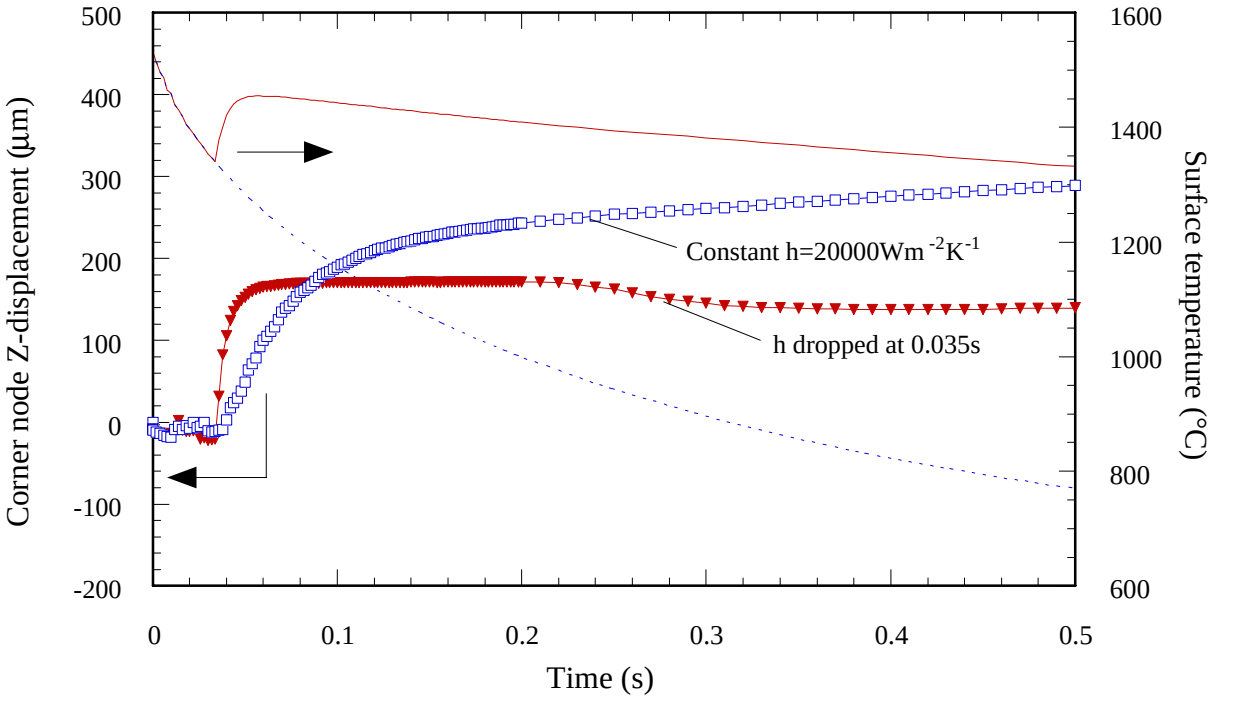

Figure 5.30. Deformation, comparing effect of dropping h at 0.035 s for 0.003%C (Case 1.1 and Case 1.2)

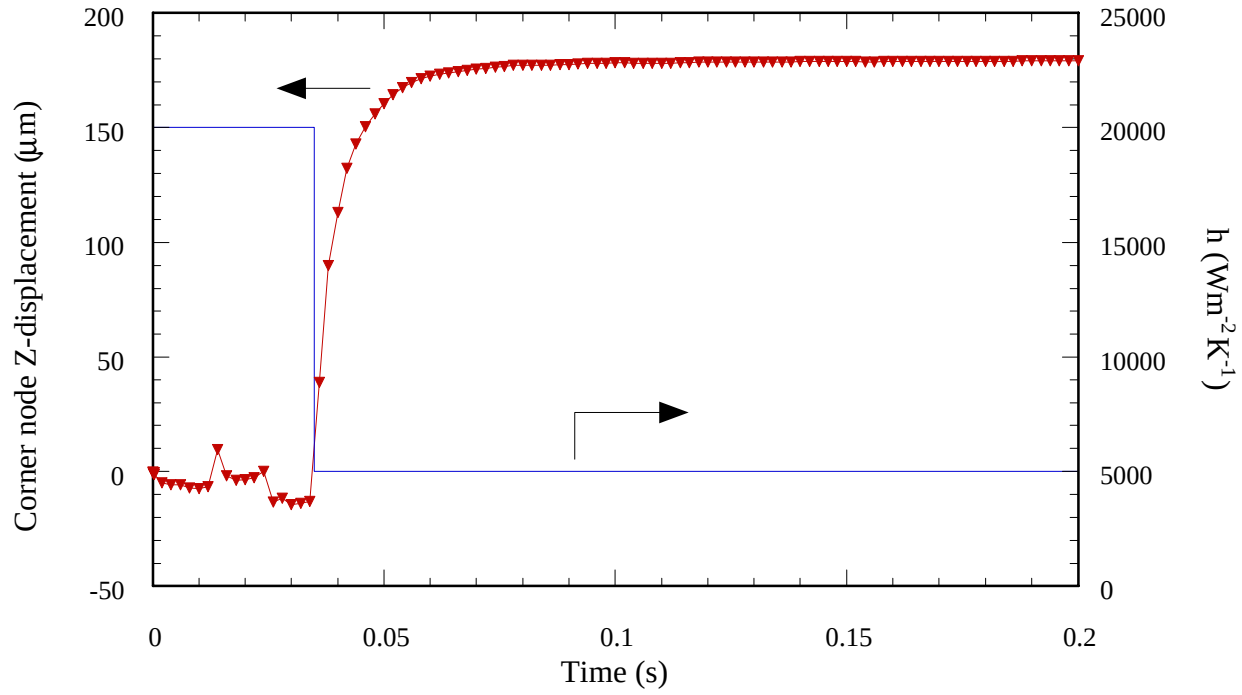

Figure 5.31. Corner node displacement and heat transfer coefficient function

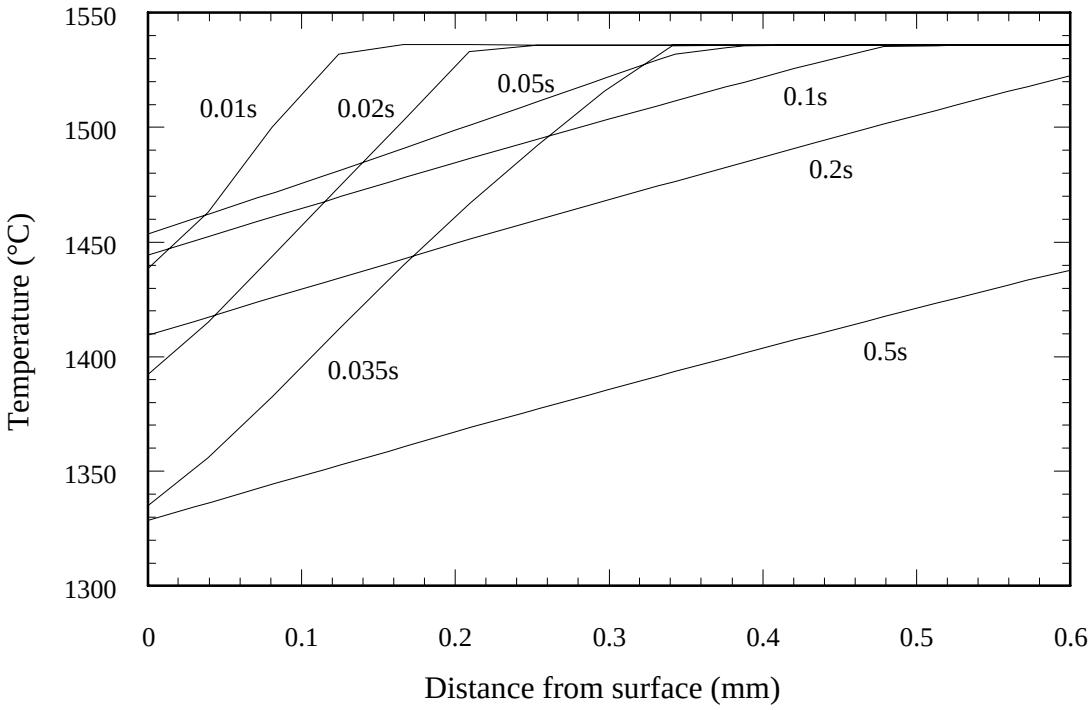

Figure 5.32. Temperature slice history of 0.003%C for early times (Case 1.1)

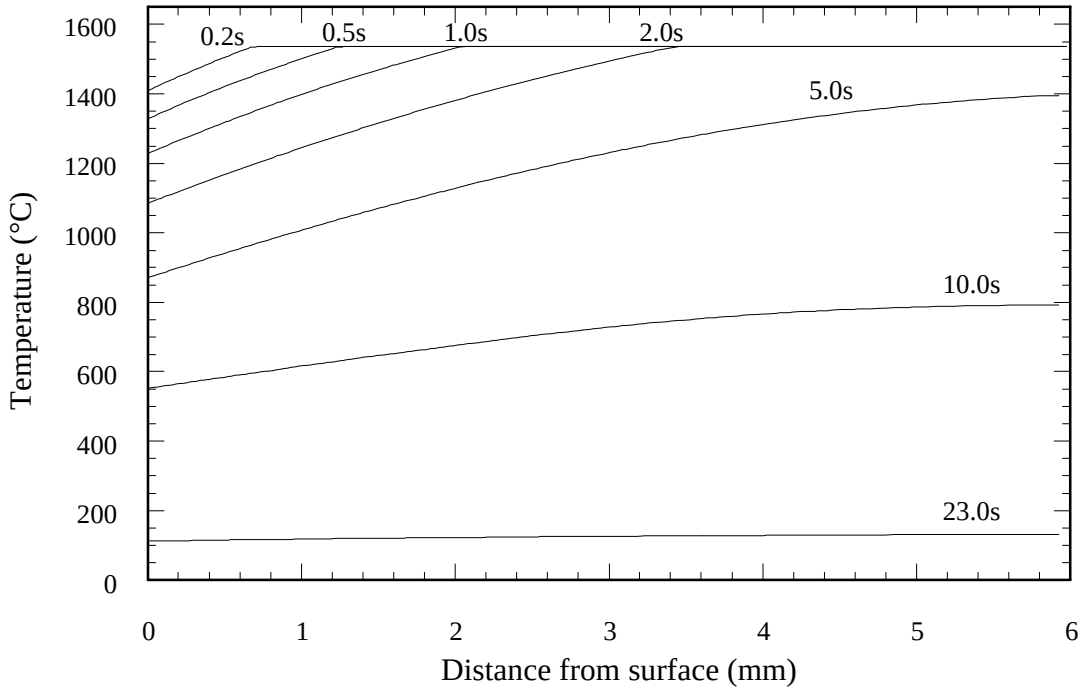

Figure 5.33. Temperature slice history of 0.003%C for later times (Case 1.1)

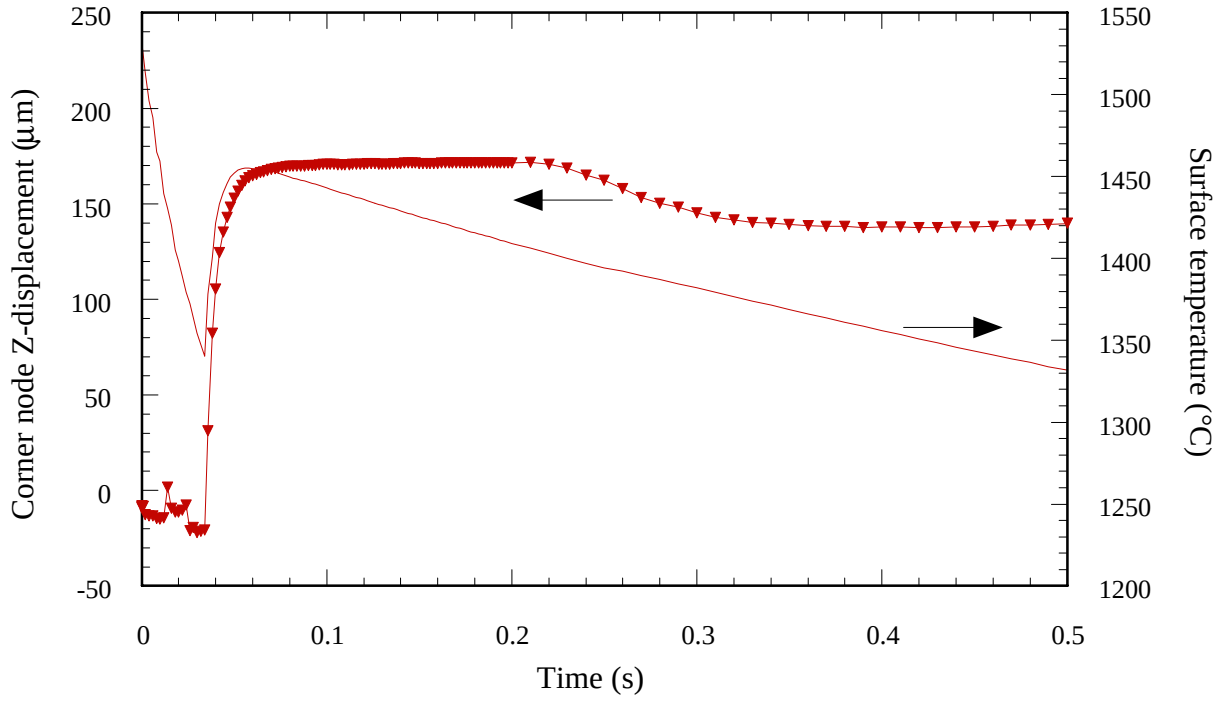

Figure 5.34. Corner node displacement and temperature for early times of 0.003%C (Case 1.1)

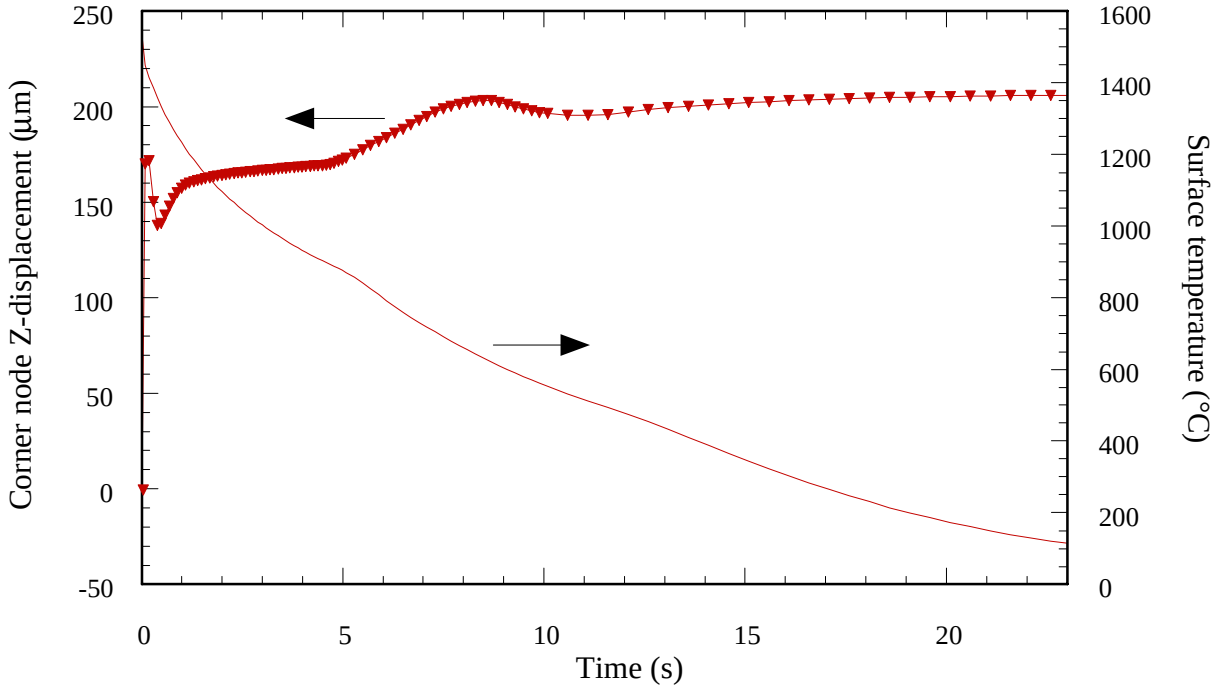

Figure 5.35. Corner node displacement and temperature for later times of 0.003%C (Case 1.1)

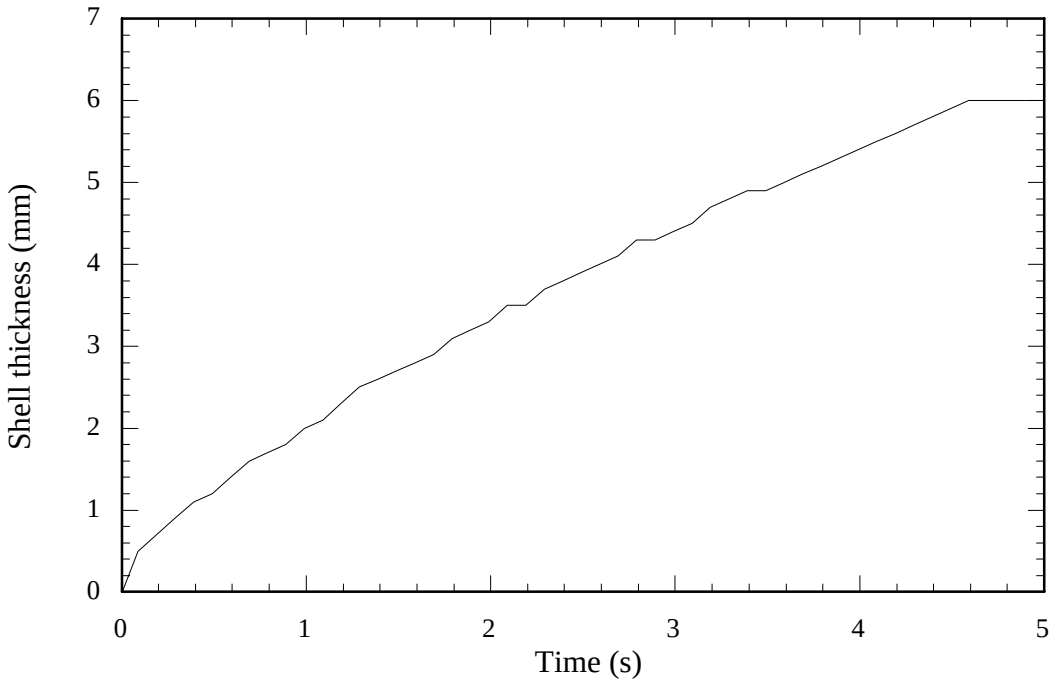

Figure 5.36. Calculated shell growth history of droplet for 0.003%C (Case 1.1)

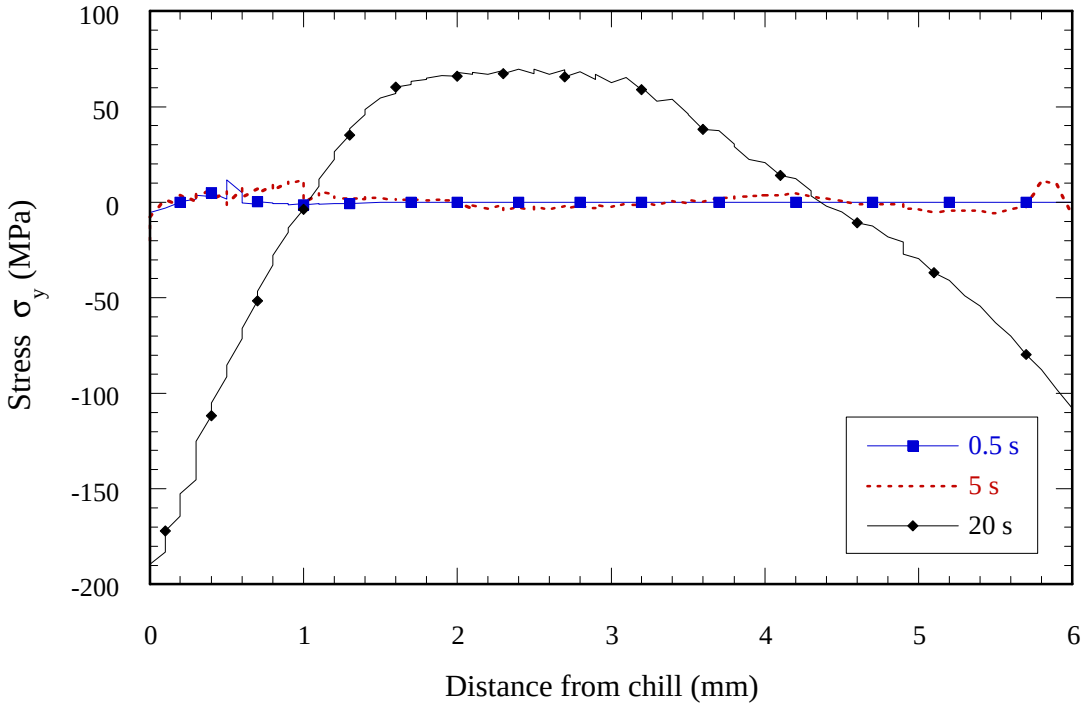

Figure 5.37. Evolution of transverse stress profiles through droplet for 0.003%C (Case 1.1)

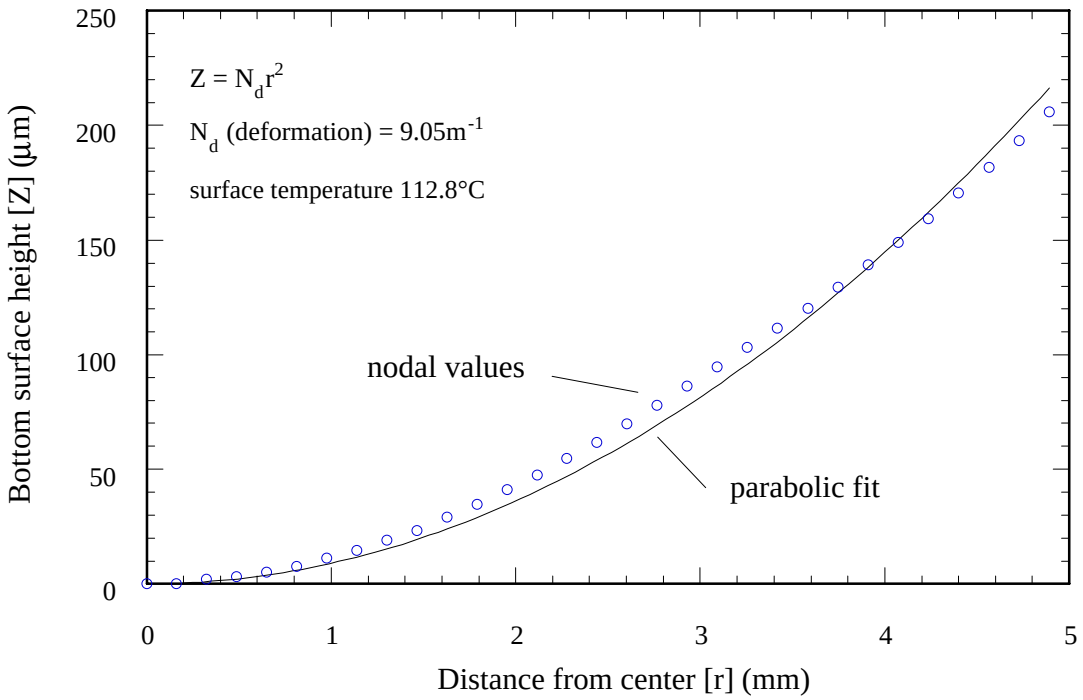

Figure 5.38. Final deformation curve fit for 0.003%C (Case 1.1)

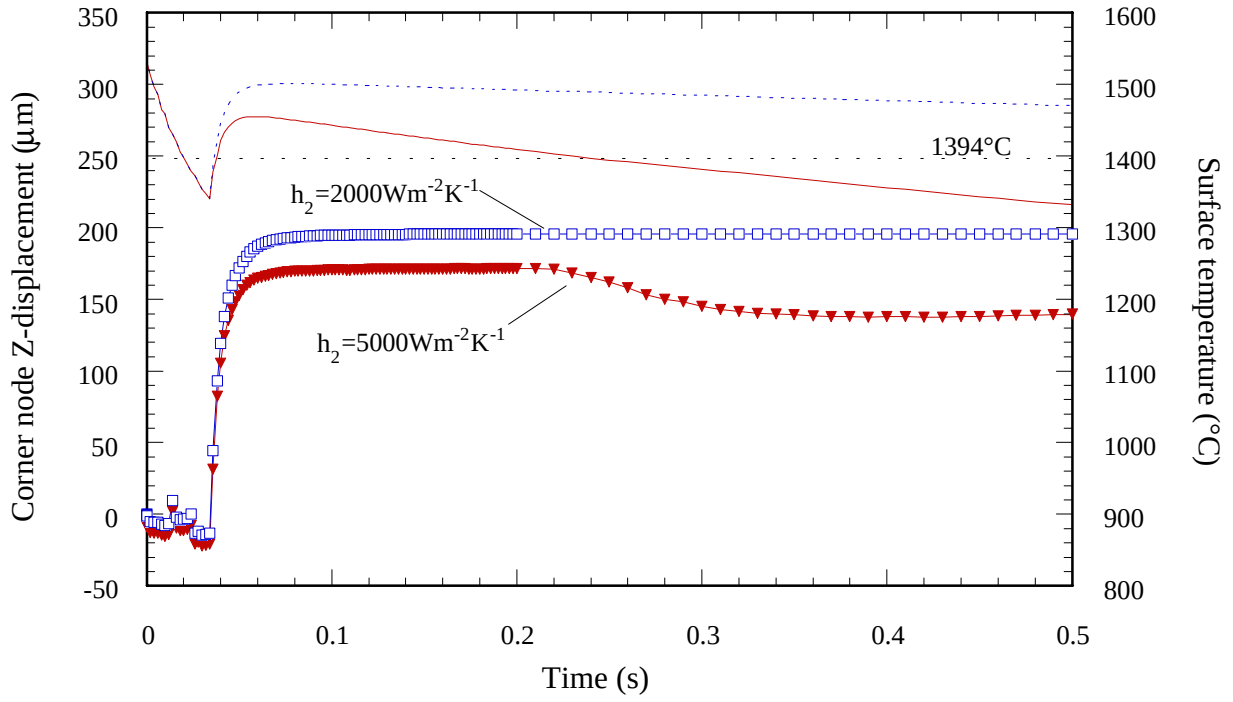

Figure 5.39. Heat transfer effect on deformation and temperature for early times for 0.003%C (Case 1.1 and Case 1.2)

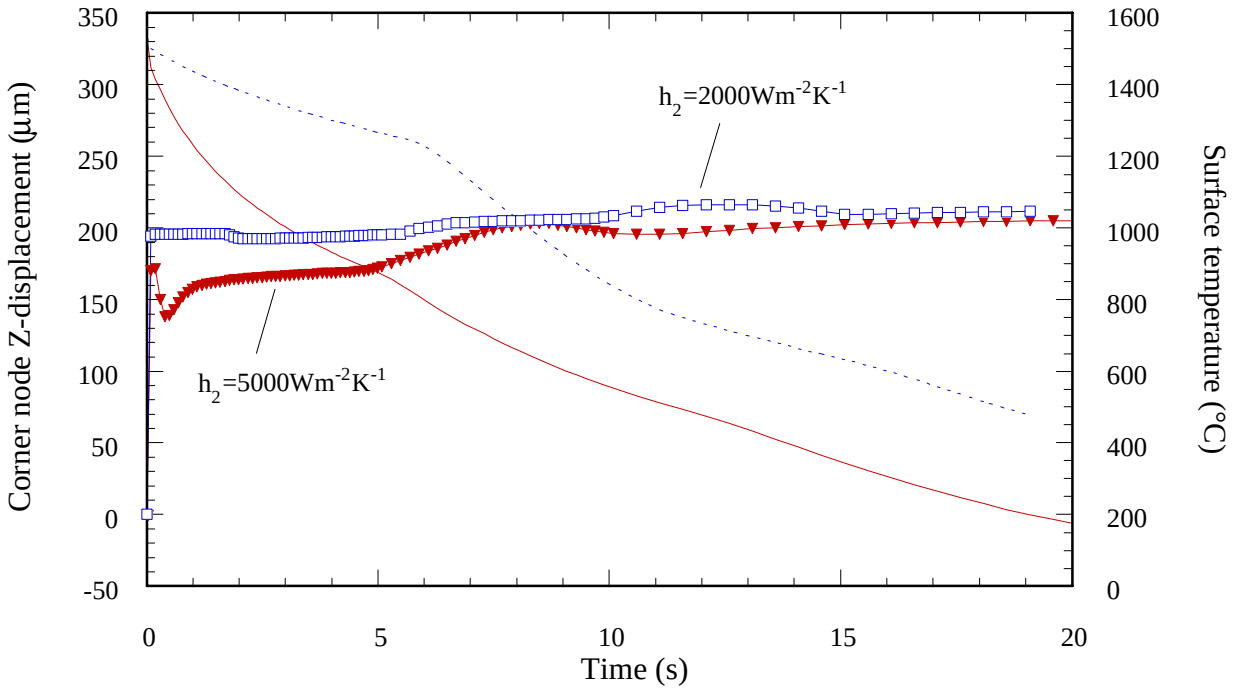

Figure 5.40. Heat transfer effect on deformation for later times for 0.003%C (Case 1.1 and Case 1.2)

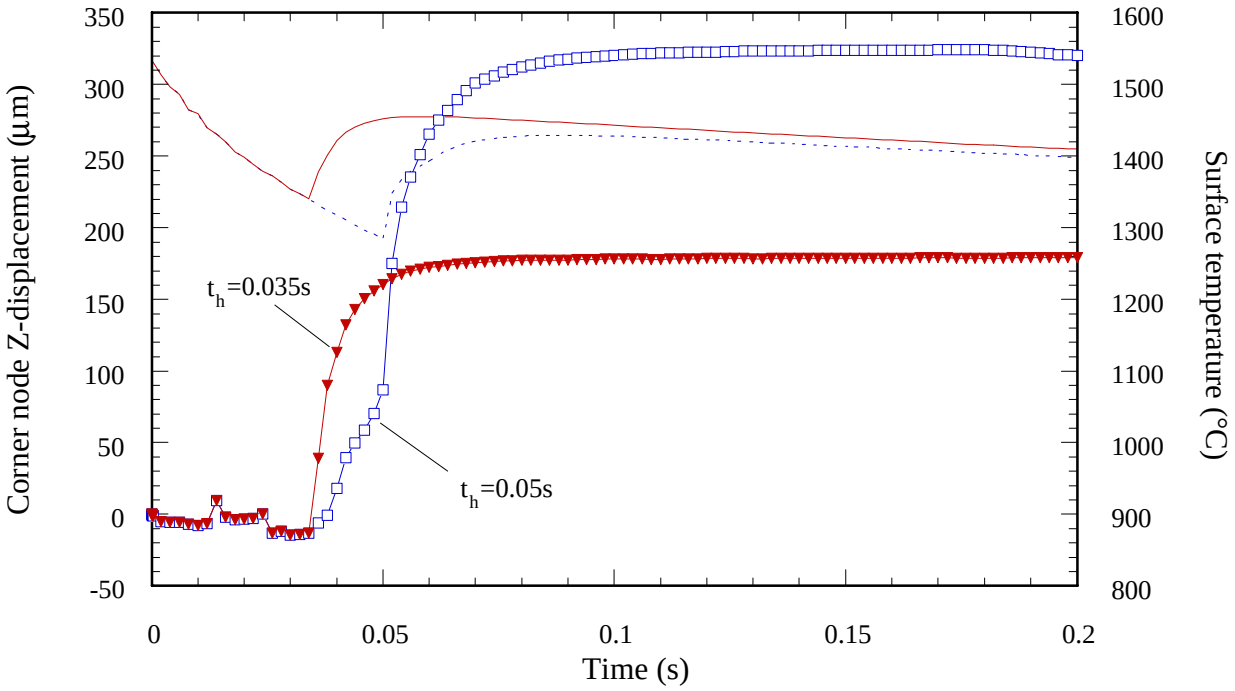

Figure 5.41. Effect of heat transfer transition times (t_h) for 0.003%C (Case 1.1 and Case 1.3)

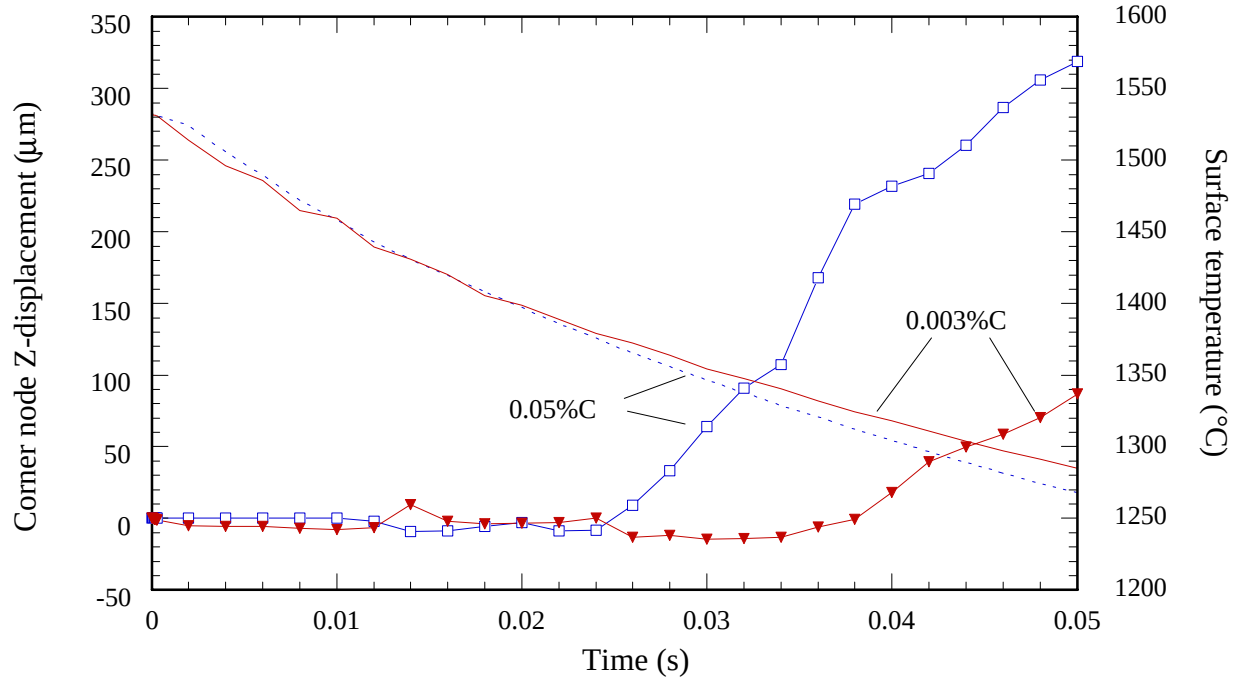

Figure 5.42. Comparing effect of carbon on initial deformation with constant h (Case 1.0 and Case 2.0)

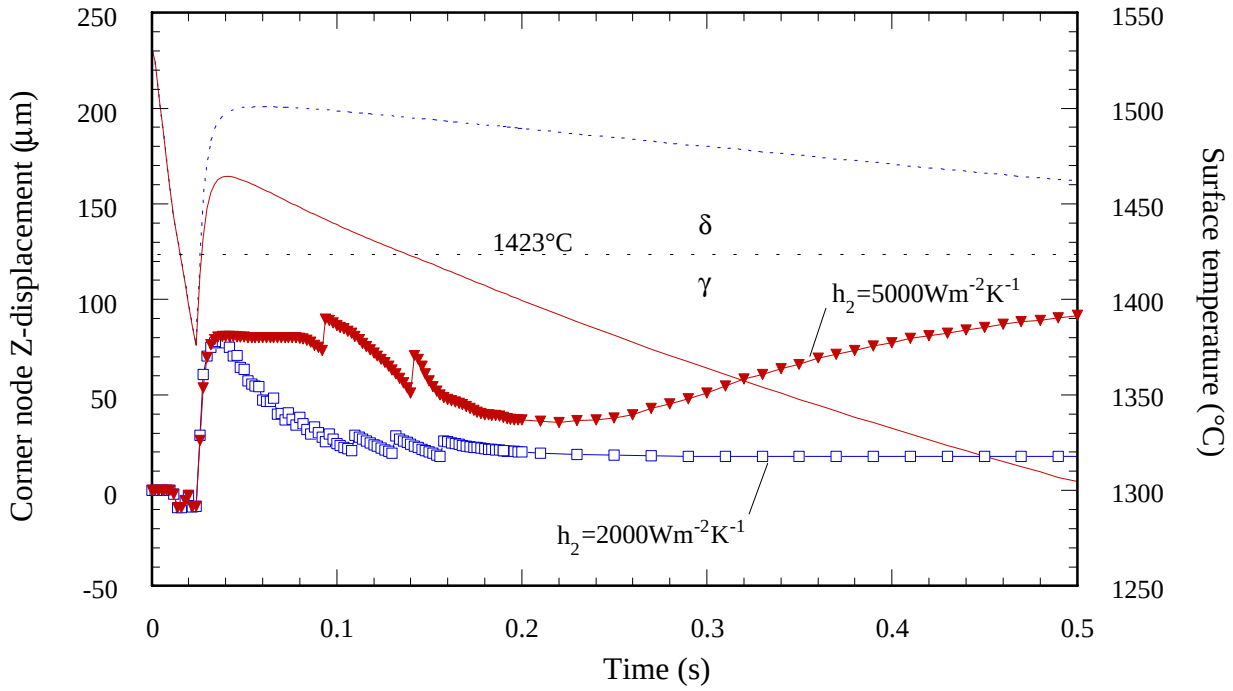

Figure 5.43. Comparison of heat transfer coefficient, h_2, for early times for 0.05%C (Case 2.1 and Case 2.2)

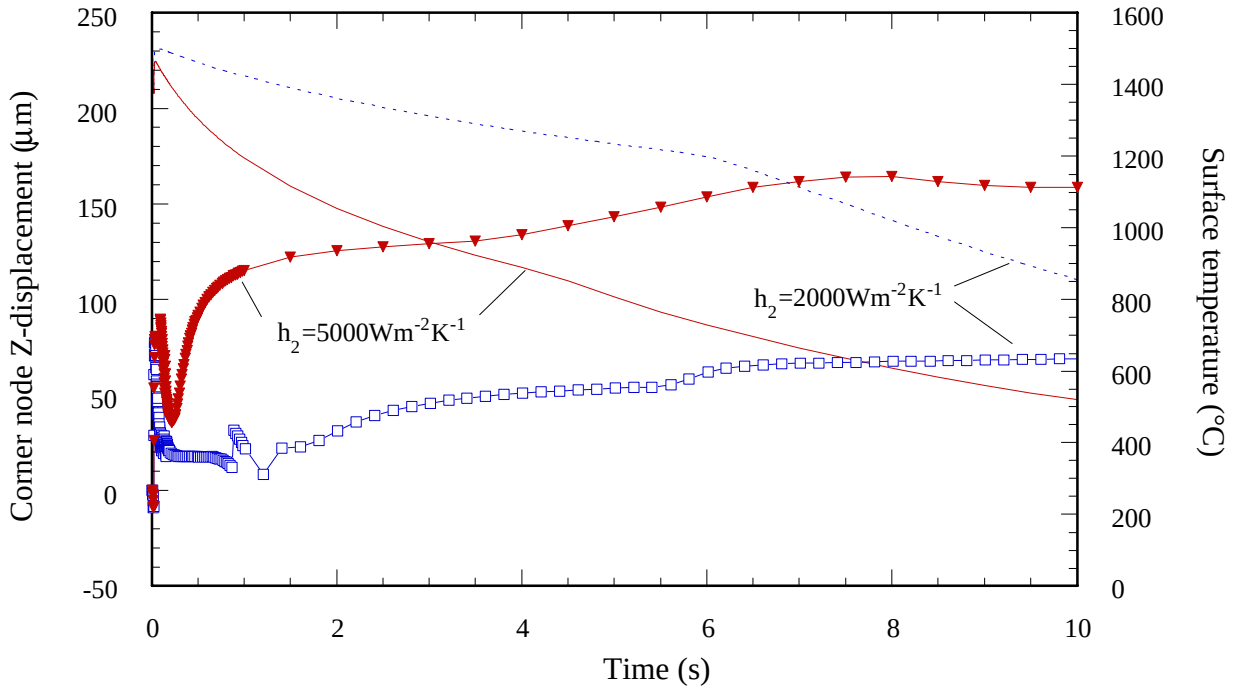

Figure 5.44. Comparison of heat transfer coefficient, h_2, for later times for 0.05%C (Case 2.1 and Case 2.2)

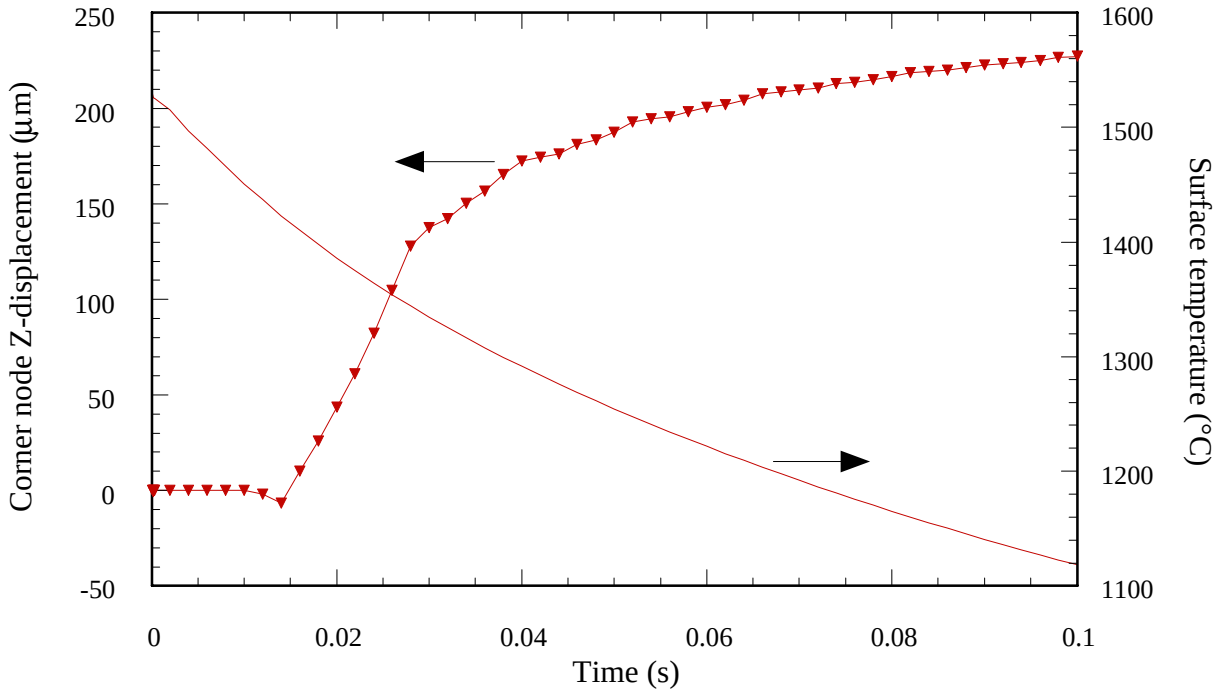

Figure 5.45. Initial surface deformation of 0.12%C with a constant h (Case 3.0)

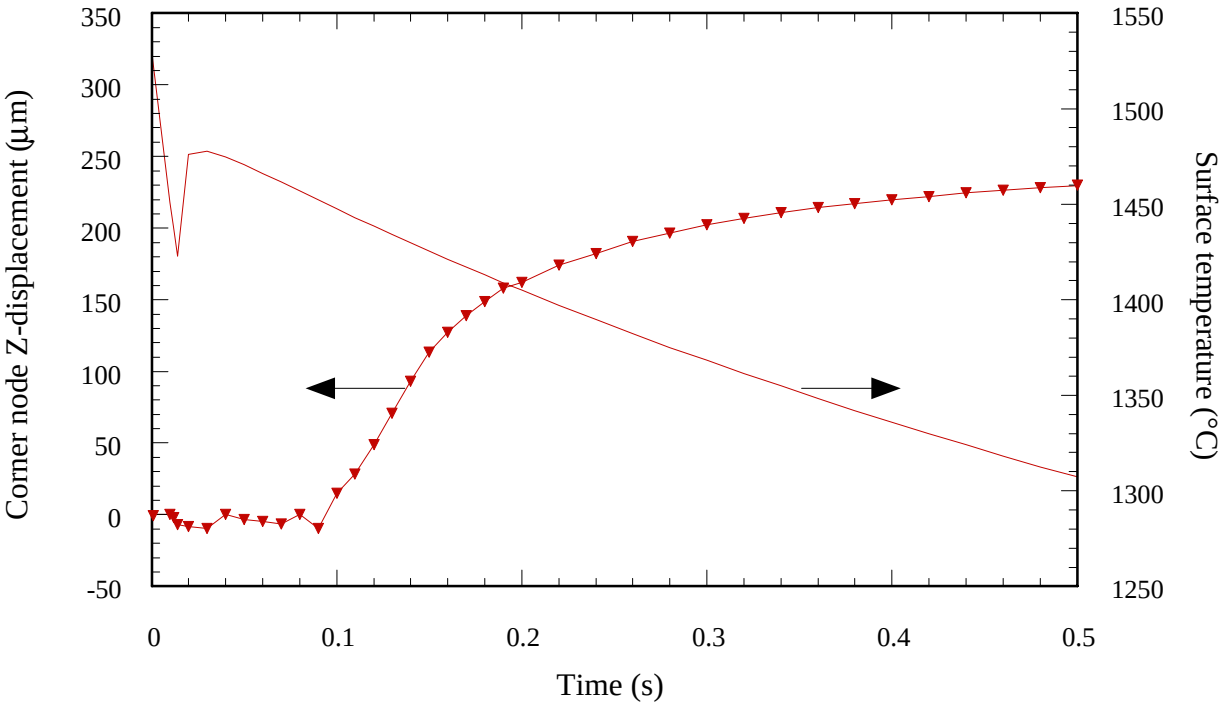

Figure 5.46. Graph of deformation for 0.12%C at early times (Case 3.1)

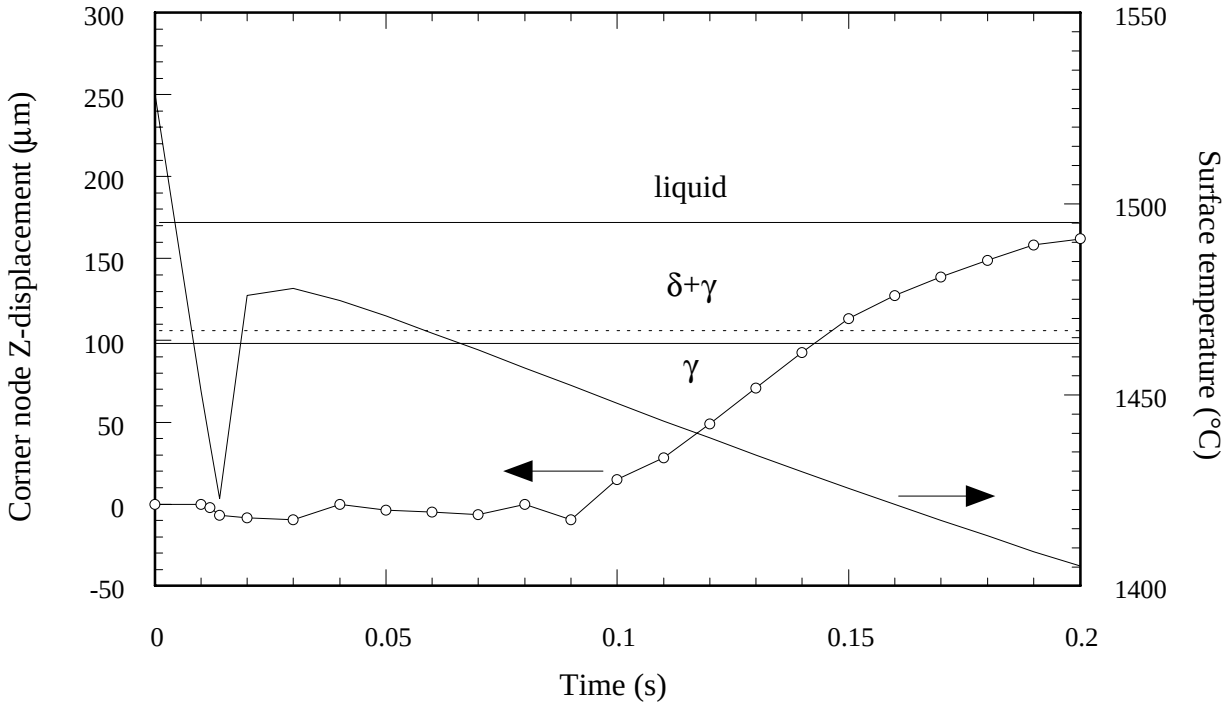

Figure 5.47. Detail of deformation for 0.12%C along with transition line temperatures (Case 3.1)

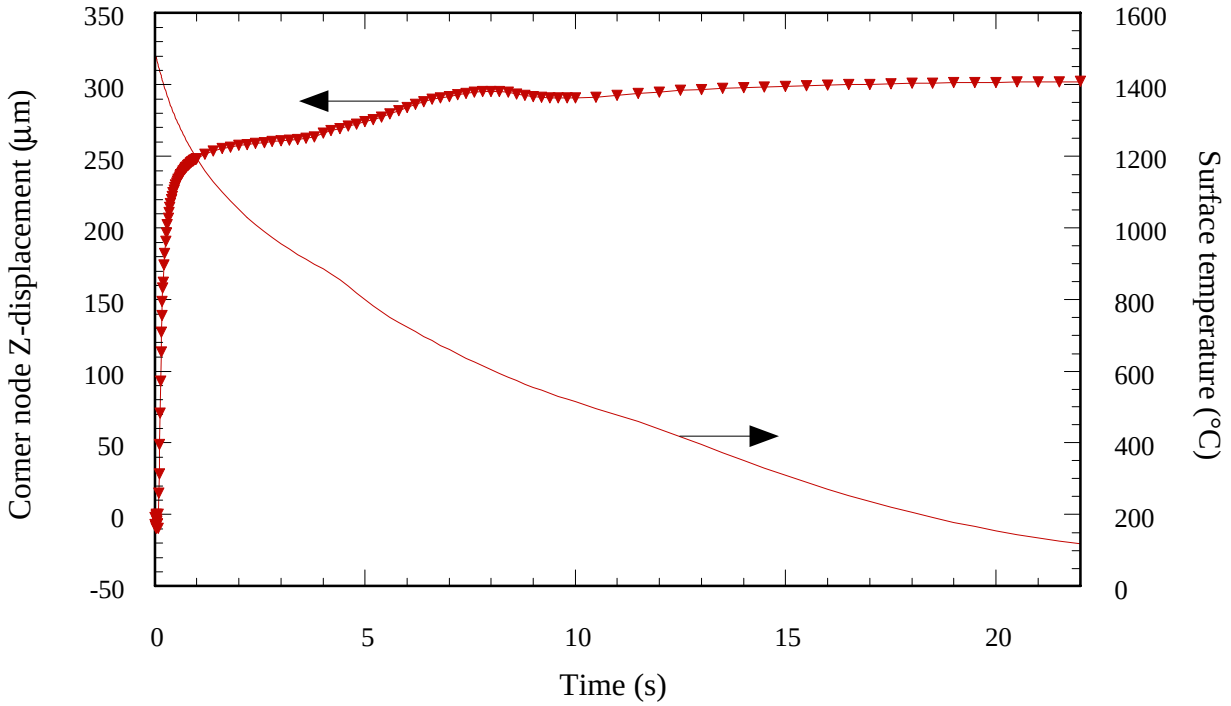

Figure 5.48. Graph of deformation for 0.12%C for later times (Case 3.1)

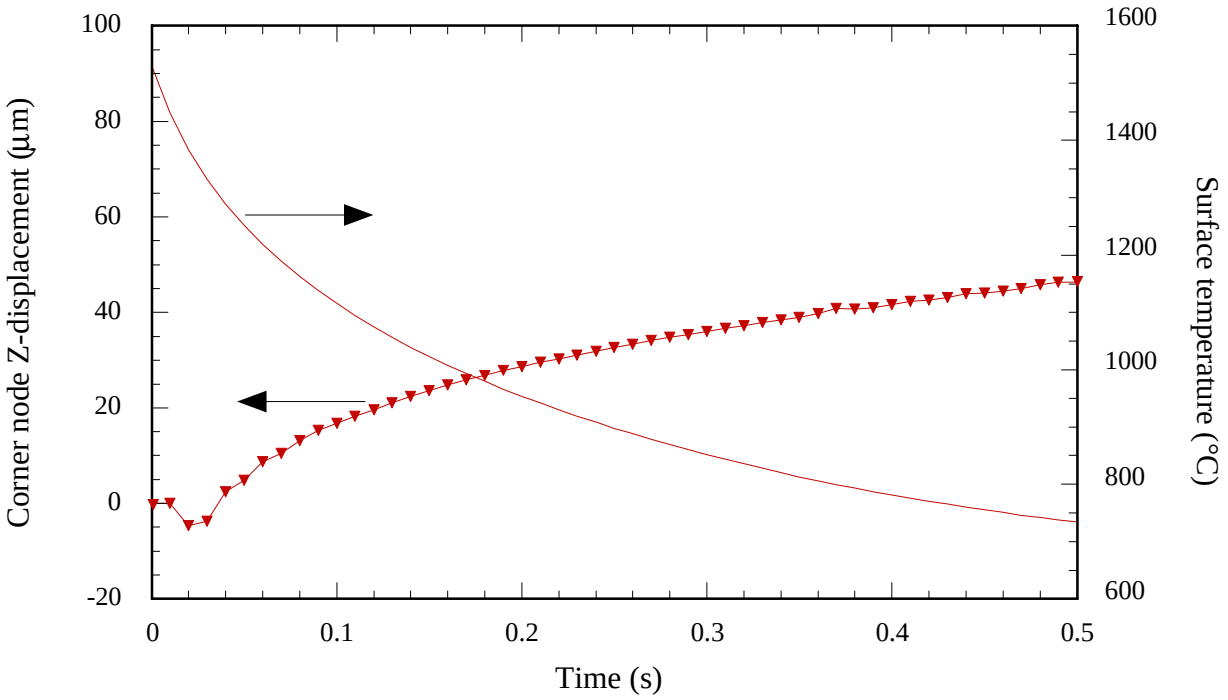

Figure 5.49. Initial surface deformation of 0.16%C with a constant h (Case 4.0)

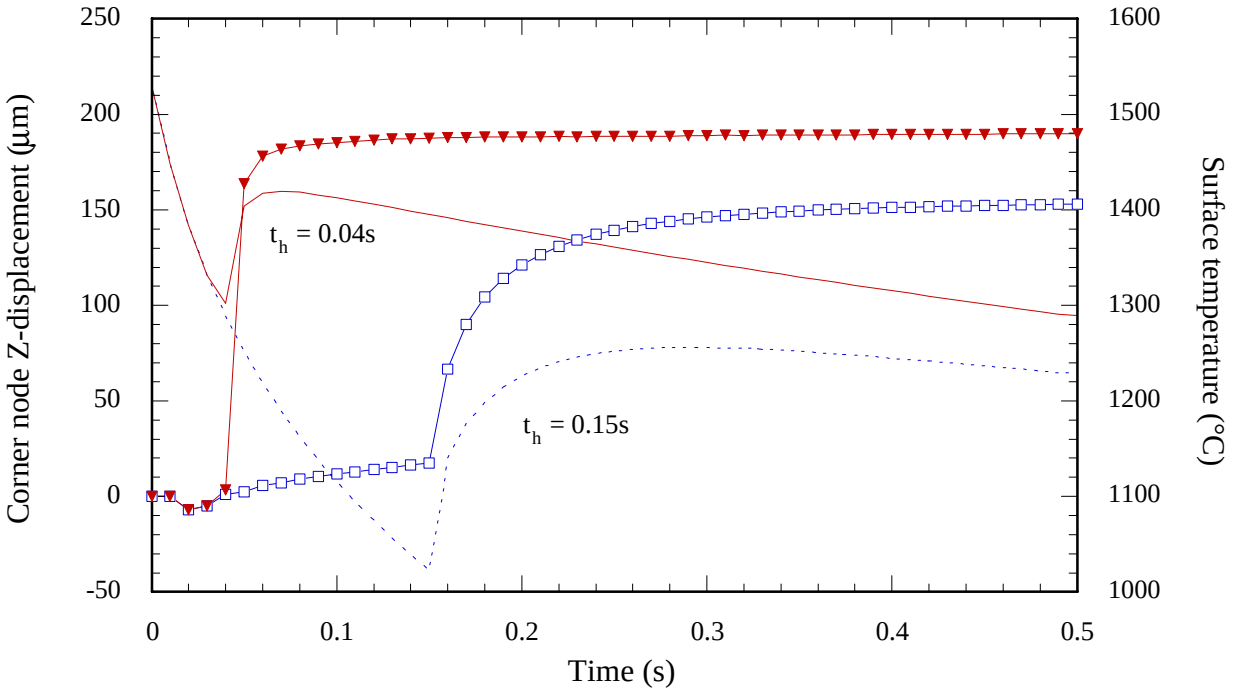

Figure 5.50. Graph of deformation for 0.16%C for early times with various t_h (Case 4.1 and Case 4.2)

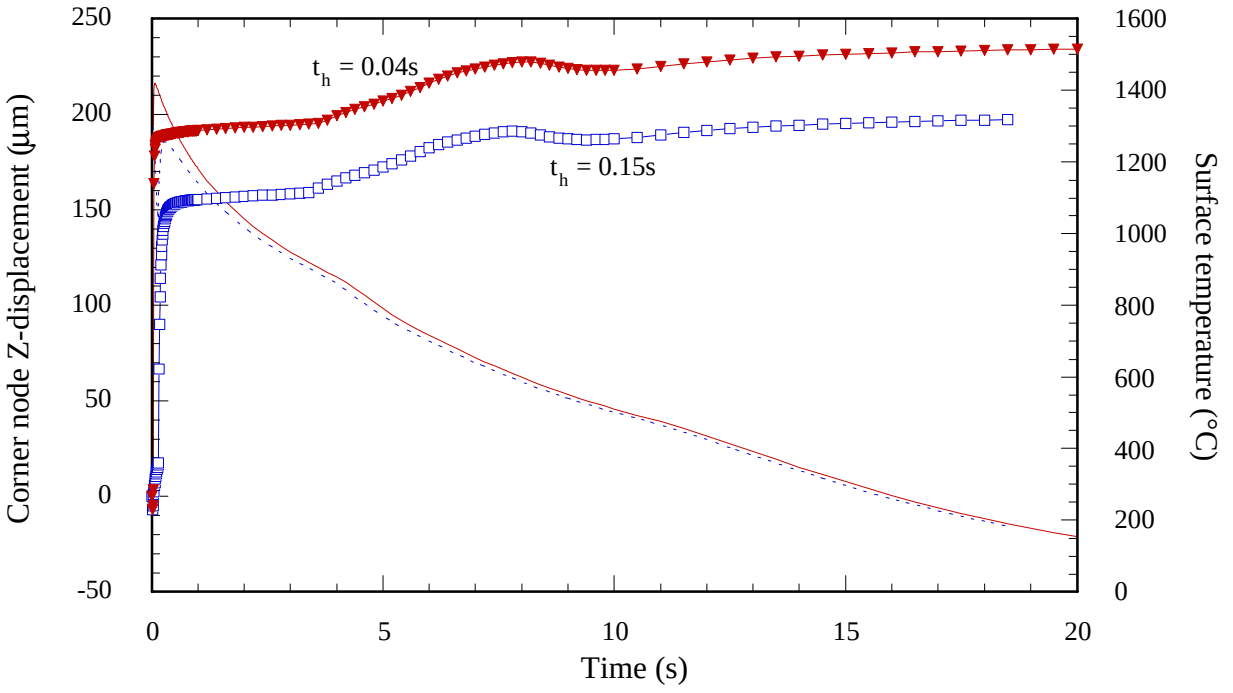

Figure 5.51. Graph of deformation for 0.16%C for later times with various t_h (Case 4.1 and Case 4.2)

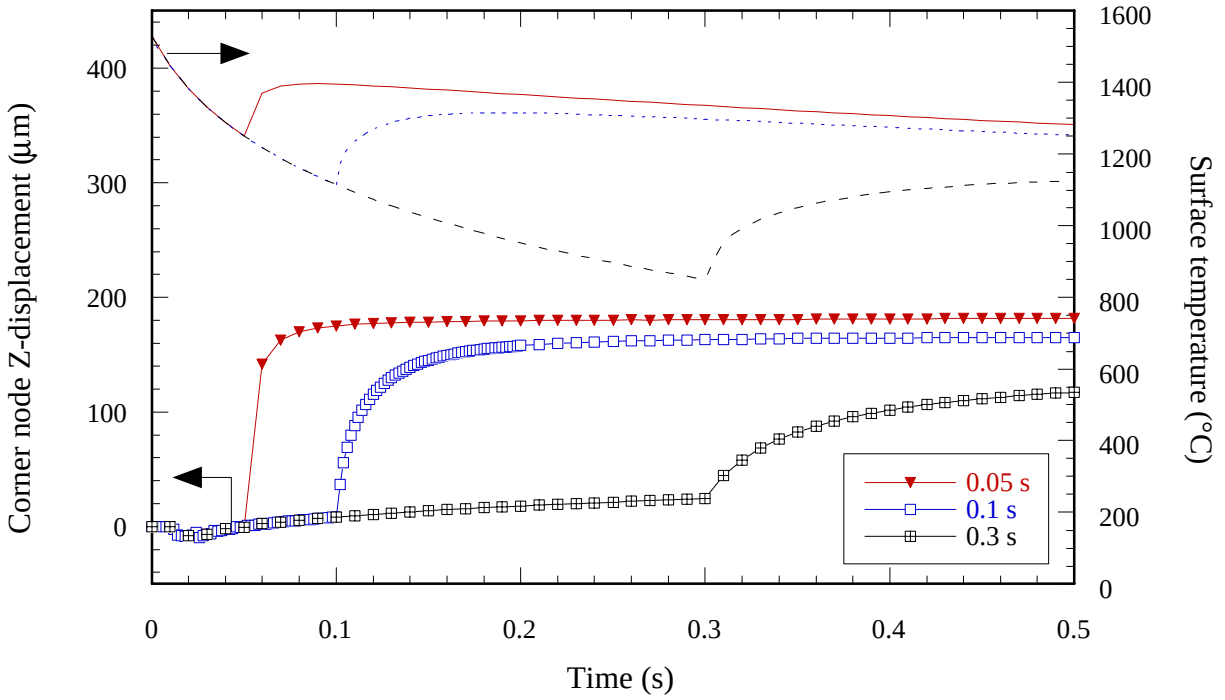

Figure 5.52. Graph of deformation for 0.23%C for early times with various t_h (Case 5.1, Case 5.2, and Case 5.3)

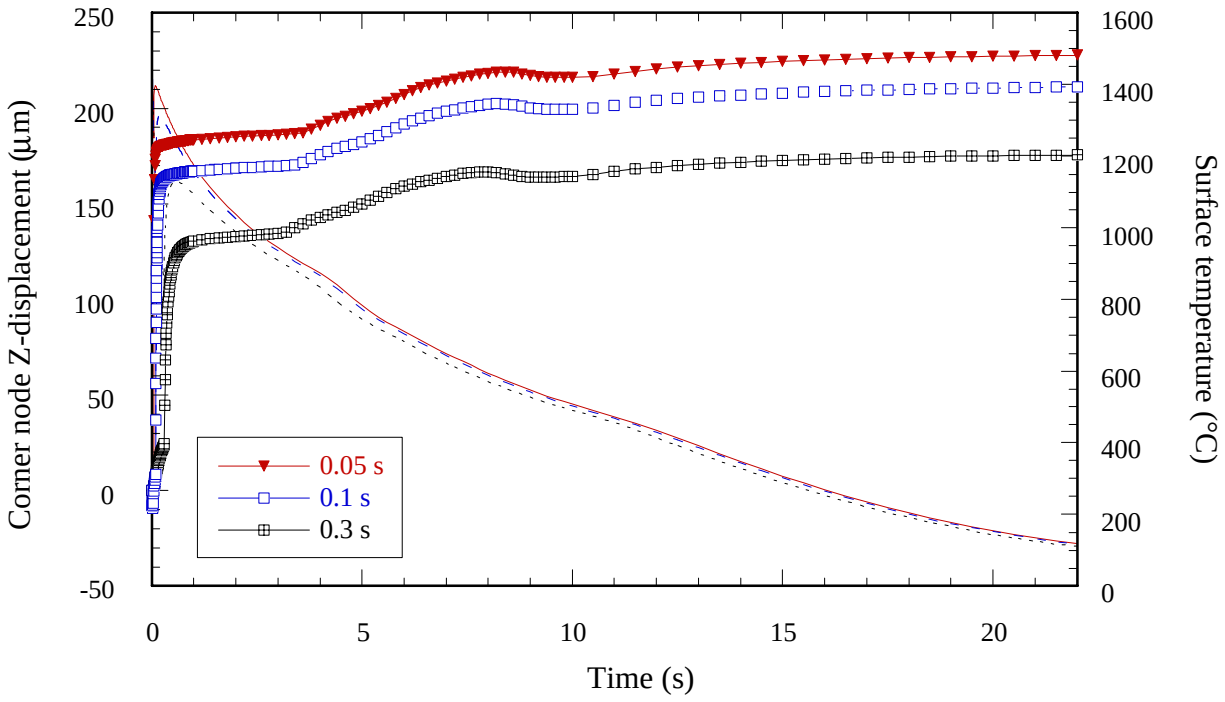

Figure 5.53. Graph of deformation for 0.23%C for later times with various t_h (Case 5.1, Case 5.2, and Case 5.3)

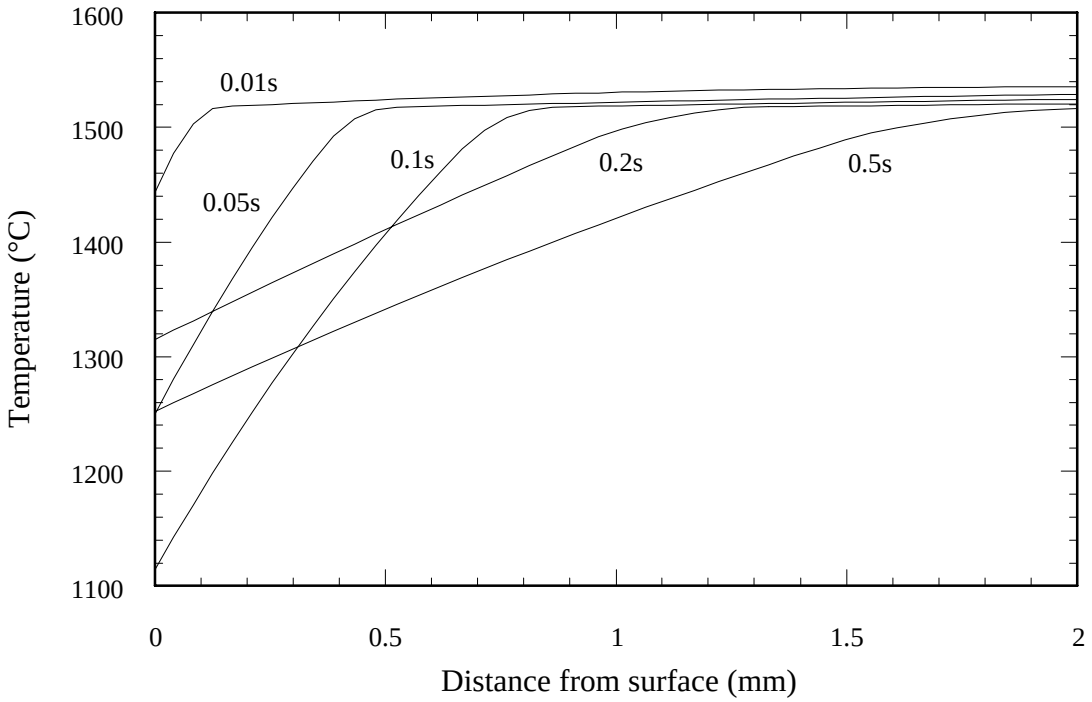

Figure 5.54. Graph of temperature slices for 0.23%C for early times (Case 5.2)

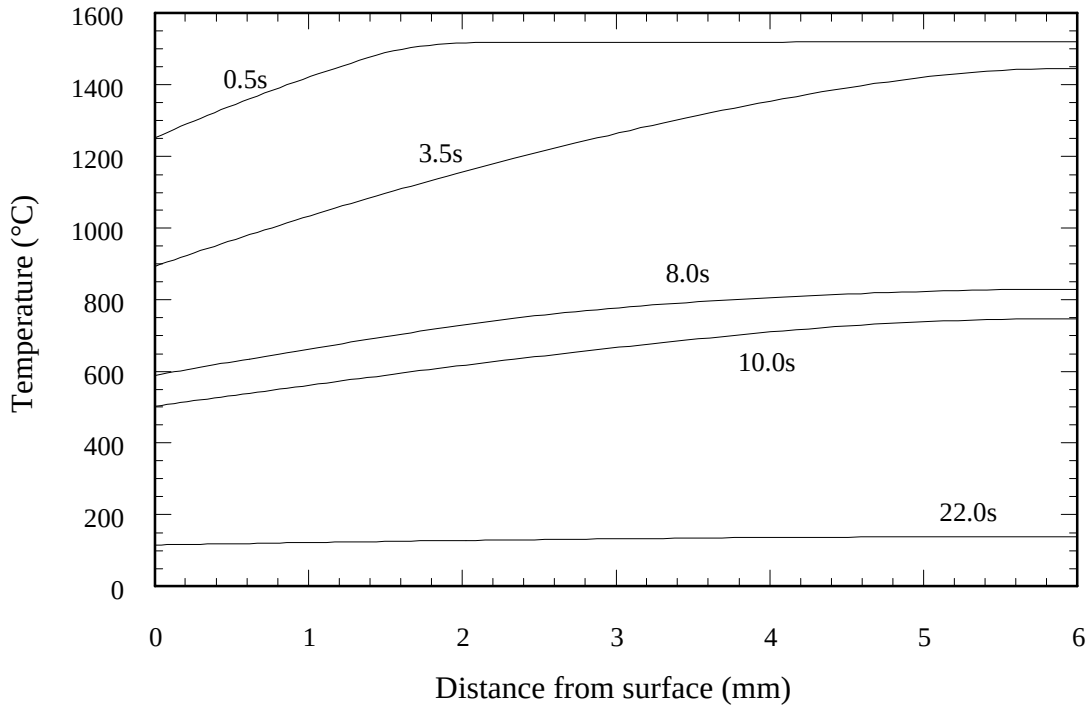

Figure 5.55. Graph of temperature slices for 0.23%C for later times (Case 5.2)

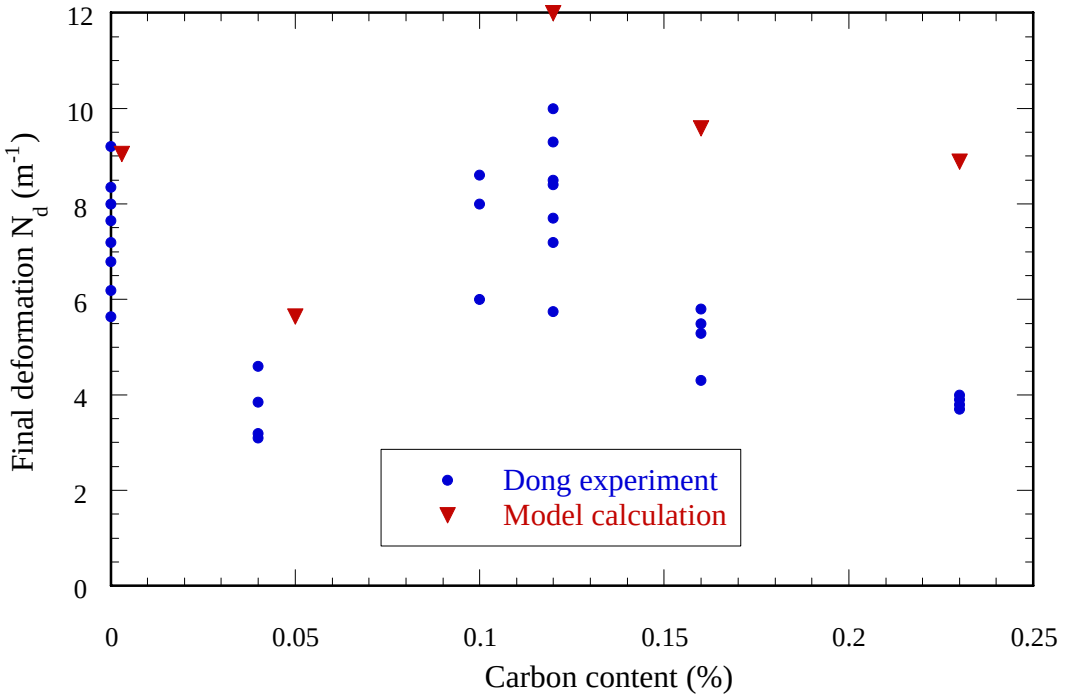

Figure 5.56. Final comparison of simulation with experiment results from Dong et al. [20]

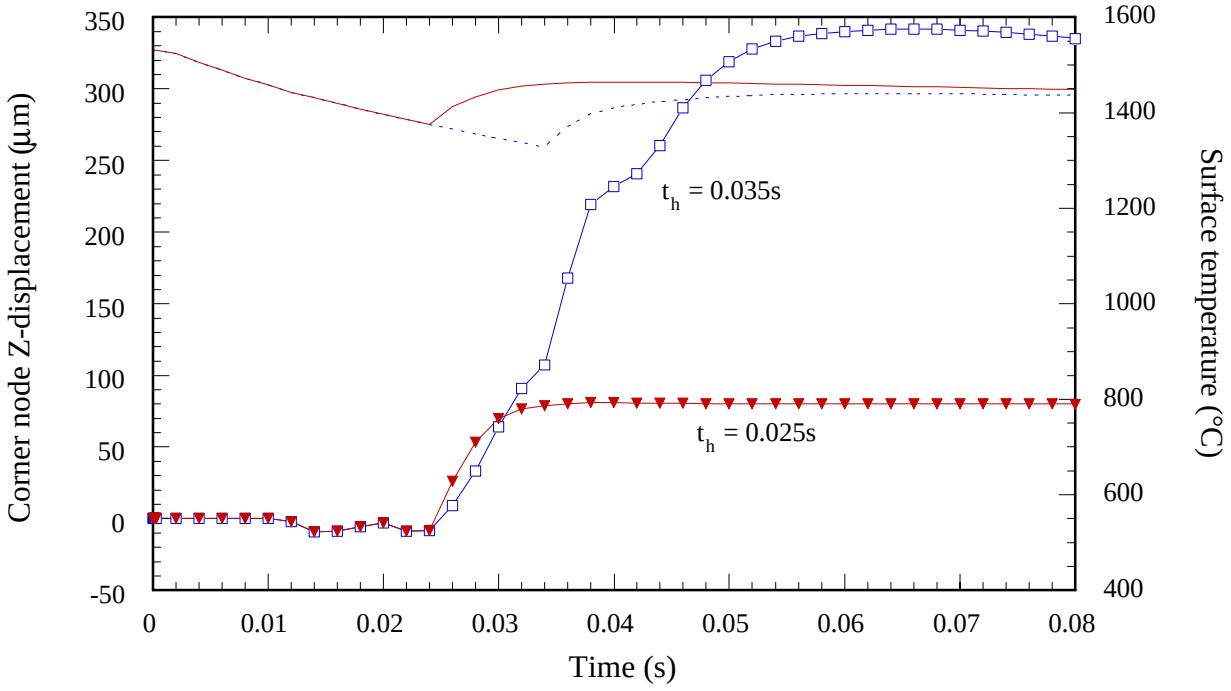

Figure 5.57. Comparison of various transition times for 0.05%C
(Case 2.1 and Case 2.3)

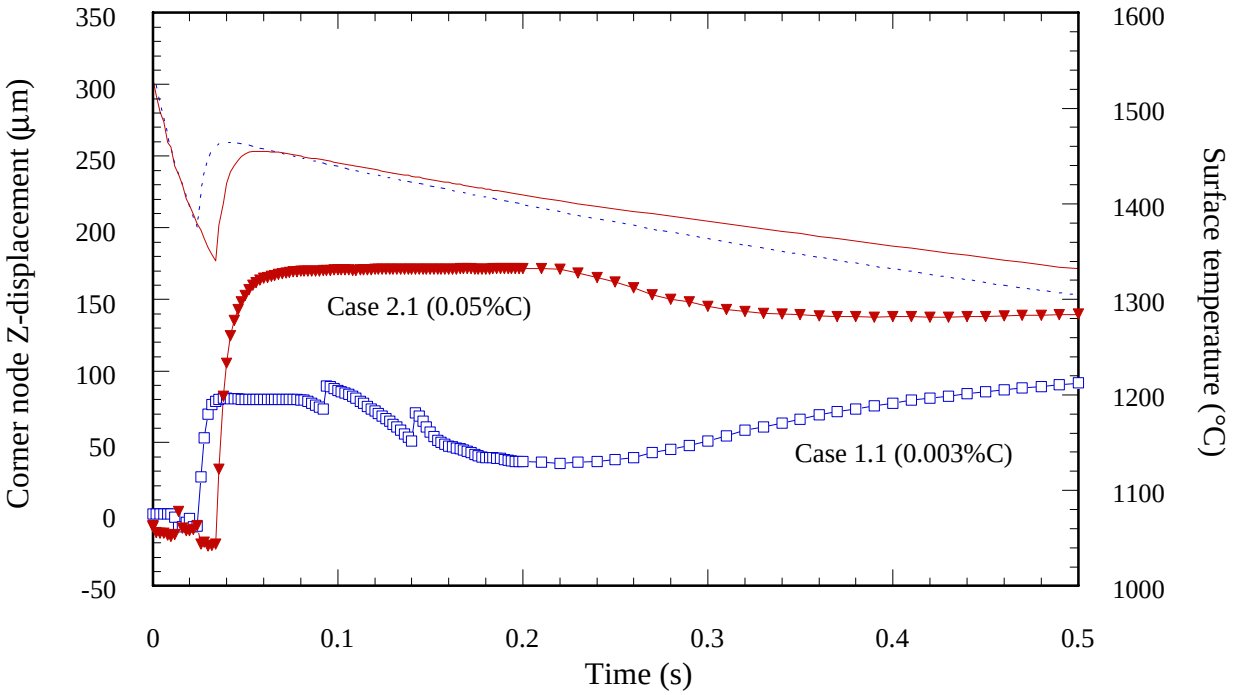

Figure 5.58. Comparison of 0.003 and 0.05%C for early times (Case 1.1 and Case 2.1)

6 Model Results

As part of a larger project to develop and apply a comprehensive system of mathematical models of the continuous casting of steel slabs, this finite-element model is being used to predict stress and deformation in the solidifying shell in continuous casting. The previous chapter displayed the ability of the model to realistically treat many complex solidification phenomena, hence displaying the robustness of the model. Here the model is used to predict the stress and deformation development in the continuous cast shell again using a simplified mesh. The results of the analysis are applied to the prediction of cracks and ideal mold taper.

6.1 Stress Analysis

To simulate the stress and strain development as the shell solidifies a one-dimensional slice model is applied as seen in Figure 5.18. The interfacial heat flux is input from another model, CON1D [72], that features a detailed treatment of the interfacial gap between the solidifying steel shell and the water-cooled copper mold. It includes mass and momentum balances on the solid and liquid powder layers. It also predicts the thickness and temperature distribution of the solidified and liquid powder layers, mold temperatures, and the heat flux distribution down the mold. The effects of oscillation mark size on both the powder consumption and heat transfer are also incorporated. For this particular work, CON1D [72] was used to produce the heat flux curves in Figure 6.1, which correspond to typical conventional (low heat flux) and thin slab casting practices (high or standard heat flux). The simulations then assume a constant pour temperature throughout the mesh of 1540°C.

To minimize numerical errors, a very fine, uniform mesh was used. The mesh size is 20 mm x 1 mm with 201 nodes per row across the wide shell. This results in 800 heat transfer elements and 200 stress elements. The time step size varies from 0.001 seconds initially to 0.005 seconds at 1

second. A 15 second long simulation needs approximately 10 minutes to complete on an IBM RS6000-370.

Figure 6.2 displays the calculated shell growth for 0.044%C steel. The standard heat flux input has a 10 mm thick shell, around 14 seconds. For the low heat flux case the shell growth is just slightly less with a shell thickness around 8.7 mm after 14 seconds.

Figure 6.3 - 6.8 display the stress / strain evolution for the 0.044%C for the standard heat flux case. The plots display the stress and inelastic strain distribution through the shell thickness at different times below the meniscus. At 0.5 seconds, both stress and inelastic strain are slightly positive at the surface as the shell is entirely in the δ phase. One second later at 1.5 seconds, the surface of the shell has cooled into the γ phase causing the surface stress to go into compression. At 10 seconds below the meniscus (Figure 6.7) the surface of the shell has cooled enough forcing the inelastic strain to be slightly negative. At 13 seconds (Figure 6.8) the surface compression is around 8 MPa with 5 MPa of tension 5 mm beneath the surface.

Results were also conducted to measure the effects of the constitutive laws on the amount of stress development. Figure 6.9 compares the effect of the δ law constitutive equation for the standard heat flux case at 5 seconds below the meniscus. The plot labeled as (γ law in δ) utilizes Model III of Kozlowski [45, 46] for the entire simulation including the delta ferrite region. The plot labeled as (δ law in δ) utilizes Model III for most of the simulation but uses the Power Law (δ phase) whenever the solid fraction of δ is greater than 10% as previously discussed in Chapter 5. The addition of the δ law allows more inelastic strain to occur in the delta ferrite phase, which decreases the amount of tensile stress beneath the surface.

6.1.1 Effect of Carbon Content

Typical strain distributions through the shell thickness is shown in Figure 6.10 for 0.1%C steel at 5 seconds below the meniscus for the standard heat flux case. At the surface, the inelastic and elastic strains are relatively small, so the total strain matches the thermal strain accumulated in the solid. Ideal taper calculations are therefore calculated reasonably based solely on the temperature of the surface. At the solidification front, liquid contraction exceeds solid shell shrinkage, causing flow into the mushy zone. It may be significant that 0.1% inelastic strain is accumulated in the solid during the δ to γ transformation. This occurs within the critical temperature range 20-60°C below the solidus, where segregation can embrittle the grain boundaries, liquid feeding is difficult, and strain can concentrate in the thin liquid films. Figure 6.11 shows that for a lower carbon steel, 0.044%C, inelastic tensile strain also accumulates during the δ to γ transformation shrinkage. However, this transformation begins 65°C below the solidus for this grade, and there is virtually no inelastic strain generated in the weak delta phase. This effect may partly explain the better ductility of lower carbon steels. For both steels, flow strain is generated primarily in the mushy zone, where the liquid is shrinking. Feeding is easy here, so this may not be significant. The low strains and generally similar behavior of these two grades, suggests that other phenomena may be important to crack prediction.

6.1.2 Effect of Cooling Rate

To alleviate longitudinal cracking, it has been proposed that heat flux from the shell to the mold be reduced at the meniscus [73]. This led to higher viscosity mold powders for middle carbon steels [74]. Stress and inelastic strain profiles for standard (high heat flux) and low heat flux conditions are compared in Figures 6.12 - 6.17. In both cases, which have continuous cooling, compression arises very quickly at the surface. This agrees with theory [9]. Note that average stress across the shell is always zero, which is required for equilibrium in the absence of sticking.

About 40% of the way from the surface to the weak δ phase, the stress becomes tensile. All figures (6.12 - 6.17) show that both stress and elastic strain are generated primarily during the δ to γ phase transformation.

At 13 seconds, the surface reheats below the mold by about 100°C for the standard (high heat flux) case. This increases the compressive stress near the surface, with a corresponding increase in tensile stress in the austenite. The absolute strain and stress levels are not completely different between the two cases, even though it is believed that reheating greatly increases the likelihood of crack formation [75]. Yamanaka et al. [76] suggests that a crack will form when the total strain accumulated while the steel is between a solid fraction range from 0.8 to 0.99 exceeds 1.6%. Based on this data, surface cracks should not form in the mold in either case.

Longitudinal surface cracks might initiate within 1 second of the meniscus when the shell sticks to the mold (via problems with flux feeding, or mold taper problems). Here, non-uniform surface roughness will create local variations in heat transfer and shell growth rate. Strain concentrates in the hotter, thinner shell at the low heat flux regions. Localization may occur on both the small scale (at the segregated grain boundaries) and on a larger scale (within surface depressions or hot spots). Later sources of tensile stress (including constraint due to sticking, unsteady cooling below the mold, bulging, and withdrawal) worsen strain concentration and promote crack growth. Further work is needed to investigate these phenomena.

6.2 Damage Criteria

By tracking the accumulation of flow strain as the shell solidifies insight can be gained into the susceptibility of cracking. Cracks are most likely to occur when flow strain is needed to compensate shrinkage and the temperature is in a critical range near the solidus where feeding is difficult. This follows that damage criteria can be established which compile the amount of flow

strain and or inelastic strain through a specified range of temperatures near the solidus. For the present analysis two different damage criteria have been established for four different carbon contents. The descriptions below represent the accumulation of ε^f (flow strain) and or ε^P (inelastic strain) in the corresponding y-direction and the temperature range over which they are summarized.

$$\text{Damage Criteria \#1} = \sum_{T_{sol}}^{0.8\ f_{solid}} \Delta\varepsilon_y^f + \sum_{T_{sol}-\Delta T_s}^{T_{sol}} \Delta\varepsilon_y^P \tag{6.1}$$

$$\text{Damage Criteria \#2} = \sum_{T_{sol}-\Delta T_s}^{T_{sol}} \Delta\varepsilon_y^P \tag{6.2}$$

where $\Delta\varepsilon_y$ is the incremental strain in the time step and ΔT_s represents the undercooling below equilibrium solidus, dependent on grade

$\Delta T_s = 0°$ for 0.003%C

$\Delta T_s = 25°$ for 0.044%C

$\Delta T_s = 25°$ for 0.1%C

$\Delta T_s = 40°$ for 0.4%C

Figure 6.18 displays the Damage Criteria #1 for the four various grades with a standard heat flux input taken at 18 seconds into the simulation. To accumulate the entire amount of strain damage, the simulations are ran long enough to ensure that at 10 mm beneath the surface the temperature is less than solidus minus ΔT_s. For the 0.1%C and 0.4%C this time was underestimated and the total strain damage is only accurate up to 7 mm beneath the surface for Figures 6.18 and 6.19. This is the reason for the drop-off in strain damage observed for 0.1%C and 0.4%C near 10 mm beneath the surface. The high levels of strain damage right at the surface are from the response of the flow strain due to the rapid cooling of the surface shortly after the simulation begins and are not of much interest. The strain damage levels of interest occur approximately 7 - 9 mm beneath the surface of the shell. 0.1%C contains the most amount of strain damage, 0.3%, at a

distance of 8.8 mm beneath the surface. Though the amount of accumulated strain is rather low, this does suggest more susceptibility to cracking in the 0.1%C as compared to the grades. Figure 6.19 displays Damage Criteria #2 for the same simulations as above. Again, 0.1%C contains the highest amount of strain damage. 0.1%C has approximately 0.2%, 8.5 mm beneath the surface. The reason for these peaks 7 - 10 mm beneath the surface, is believed to be due to the reheating below the mold when the heat flux drops. Examination of Figures 6.18 and 6.19 suggests the peaks are driven primarily driven by the accumulation of plastic strain at temperatures just below the solidus and not the accumulation of flow strain.

The strain damage criteria were also used to examine the effects of cooling rate. Figure 6.20 displays Damage Criteria #1 for 0.044%C for the two different heat flux inputs. The low heat flux case has near zero amount of accumulation 10 mm below the surface. Figure 6.21 displays Damage Criteria #2 again for the same simulations. Figures 6.20 and 6.21 are almost identical except for the differences near the surface, which suggests almost all of the strain damage can be attributed to inelastic strain taking place below the solidus. The lower heat flux case allows the shell to take a longer amount of time cooling though this critical region. This allows for greater relaxation of the inelastic stress, and hence the lower amount of strain damage.

6.3 Ideal Taper Calculations

In order to get a better understanding of the amount of shrinkage experienced in continuous casting, a series of mesh shrinkage calculations were performed using CON2D [1]. Again a similar thin mesh approach is used to model the region shown in Figure 6.22.

6.3.1 Explanation of Taper Calculations

In order to account for the ferrostatic pressure inside the shell, a force is applied along one edge of the mesh. This side of the mesh is also constrained to move as a single piece, thus, the entire side has the same displacement as shown in Figure 6.23. The force being applied to this edge is in proportional to the amount of ferrostatic pressure. The ratio is determined by dividing the half-thickness (T/2) of the caster being modeled, by the length of the mesh being used (X). For all simulations the caster thickness (T) is taken as 200 mm. The applied load is then converted into stress with the following relation:

$$\sigma_y = \frac{\rho \times g \times z \times (T/2)}{X} \tag{6.1}$$

Where ρ = density, g = gravity and z = distance from meniscus. Even though the stress is applied along the entire mesh, the liquid region has very little strength and most of the load must be carried by the solid part of the solidifying steel. The mesh size is 0.5 mm thick and 30 mm long, with 100 six node elements per every 10 mm section. The time step size varies from 0.001 seconds initially to 0.005 seconds at 1 second, after which it is kept constant.

To prevent the domain from being torn apart by the applied load, an iterative routine is applied to represent the mold walls by ensuring the mesh thickness never increases beyond its original thickness. Hence, the mesh is only allowed to shrink. This procedure is accomplished in two steps as described next. In the initial part of the simulation, the first 0.1 seconds, the load is not applied to ensure that the solid shell is at least one element thick. In the second step, after 0.1 seconds, the load is applied if it is determined the mesh is strong enough to handle the extra load without increasing beyond its original thickness. If the mesh is not able to handle the load, the load is then set to zero at that particular time step and the simulation continues, applying the load accordingly. Thus, the mesh is kept almost flat, until at some time when it is strong enough to begin shrinking. Comparisons are then made between grades and cooling conditions with the

amount of time it takes for the mesh to start shrinking. Simulations were also performed without the applied force, to gain an understanding of how much the applied load is affecting the shell.

6.3.2 Results of Taper Calculations

For the taper simulations, CON1D [72] was again used to generate both high and low typical cooling curves, which are used as input into CON2D. Figure 6.24 displays the heat flux curves generated from CON1D.

Initial simulations were performed with and without the previously described applied load in order to understand the effect of the ferrostatic pressure. Figure 6.25 displays the total y-strain experienced by the mesh for a 0.4%C steel using a high cooling rate. From the figure it is evident the applied load has a very small effect on increasing the total strain. At the end of the simulation the difference between these two cases was less than 0.05%.

Simulations were also run to compare the differences between the total y-strain experienced by the mesh and the amount of thermal strain experienced at the surface of the mesh. This would allow for taper prediction comparisons between CON2D and CON1D, as taper calculations in this model are solely based on the thermal stress. Figure 6.26 displays the total y-strain and the thermal strain for a 0.1%C using the low cooling rate curve. The figure displays two separate curves for the amount of thermal strain, one curve accumulates the amount of thermal strain starting at the solidus and the other starts accumulating the thermal strain when the fraction of delta is 10%. The amount of thermal strain accumulated below the solidus is slightly less than the total strain. The shape of the curves are also slightly different, as the thermal strain is quickly accumulated just below the solidus.

Simulations were performed on various carbon contents for both cooling rates in order to compare differences in taper between grades. All the simulations are performed with a superheat of 1°C in order to compare the grades correctly on a time scale. Figure 6.27 displays the y-strain results using the high cooling rate. 0.1%C shows the most amount of strain with 0.4%C having the least amount of strain. Figure 6.28 shows the early part of the simulation, displaying the amount of time it takes before the grade starts to shrink. Figures 6.29 and 6.30 display similar plots for the same grades using the low cooling rate. For the low cooling rate the amount of y-strain is slightly less than the high cooling rate.

Figures 6.31 and 6.32 display curves representing the shell growth, based on the solidus, between grades for the high cooling rate. The grades all have similar behavior with the exception of 0.4%C, which takes a slightly longer time to start solidifying. Figures 6.33 and 6.34 display similar curves for the low cooling rate cases. Again showing that the 0.4%C steel has the longest solidifying time.

Table 6.1 summarizes the amount of time it takes for each case to start to pull away from the mold corner. Because each grade only has a superheat of 1°C, comparisons can be made on a time basis. The table also displays the shell thickness, based again on the solidus, at the time the shell is strong enough to pull away. For most cases the shell is near 0.2 mm thick before it has enough strength to pull away from the mold. It is also evident from the table the amount of time it takes for 0.4%C steel to solidify to around 0.2 mm.

%C	time(s) low cooling rate	time(s) high cooling rate	shell(mm) * low cooling rate	shell(mm) * high cooling rate
0.003	0.102	0.102	0.10	0.20
0.044	0.298	0.156	0.20	0.21
0.1	0.51	0.26	0.20	0.22
0.4	1.02	0.302	0.22	0.18

*Shell thickness based on solidus

Table 6.1. Times and shell thickness for determining when the shell gains strength

6.4 Analysis Conclusions

Utilizing simplified one-dimensional mesh domains, the transient finite-element model simulations have predicted the development of stress and strain in a solidifying steel shell. The findings suggest the following:

1) Without sticking and with steady cooling conditions, the shell surface goes into compression within 1 second after solidification. Surface cracks grow only if these conditions are not met.
2) The δ-ferrite portion of the shell creeps very rapidly, which relaxes all of its stress. Thus, strain in this weak portion of the shell is controlled by the strength of the austenite portion.
3) Creep strain in the weak δ-ferrite and mushy portions of the shell is relatively small, because it is only needed to replace the elastic strain lost by stress relaxation.
4) In the absence of friction, the solid shell contracts on the order of 1% during the first 5 seconds of solidification. The mismatch in shrinkage generates inelastic strains at the

solidification front on the order of 0.1%, which should not be enough for it to cause cracks. Thus, stress concentration and strain localization are required for cracks to form.

5) The sensitivity of cracks to carbon content and initial cooling rate appears more related to the formation of the non-uniform shell than to direct changes in stress and strain evolution.

6) The shell pulls away from the corner of the continuous casting mold very quickly (0.1 - 0.3 seconds below meniscus) when the shell thickness grows near 0.2 mm. Longer times are required for the shell to pull away for higher carbon steels and slower cooling rate.

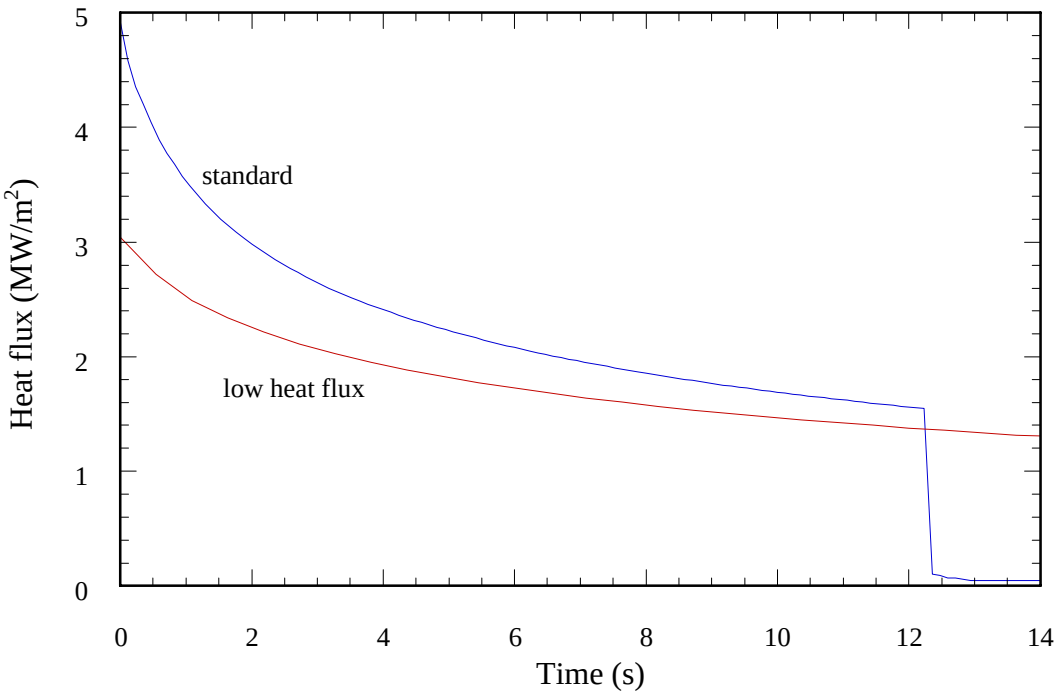

Figure 6.1. Heat flux input from CON1D for standard and low heat flux cases

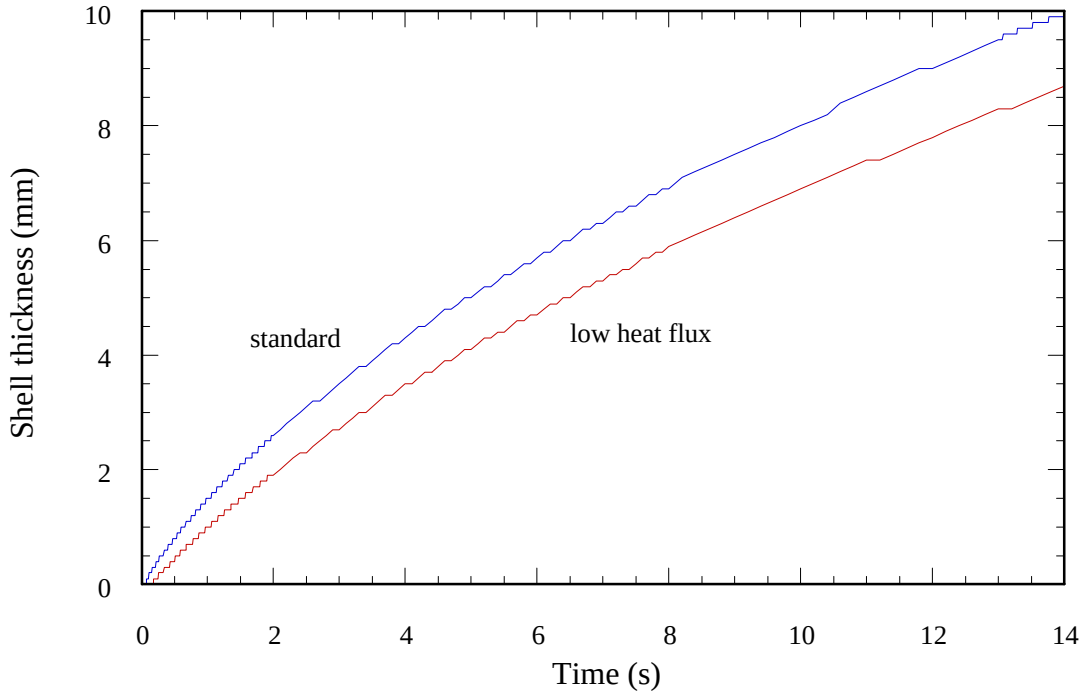

Figure 6.2. Graph of calculated shell growth for 0.044%C for both heat flux cases

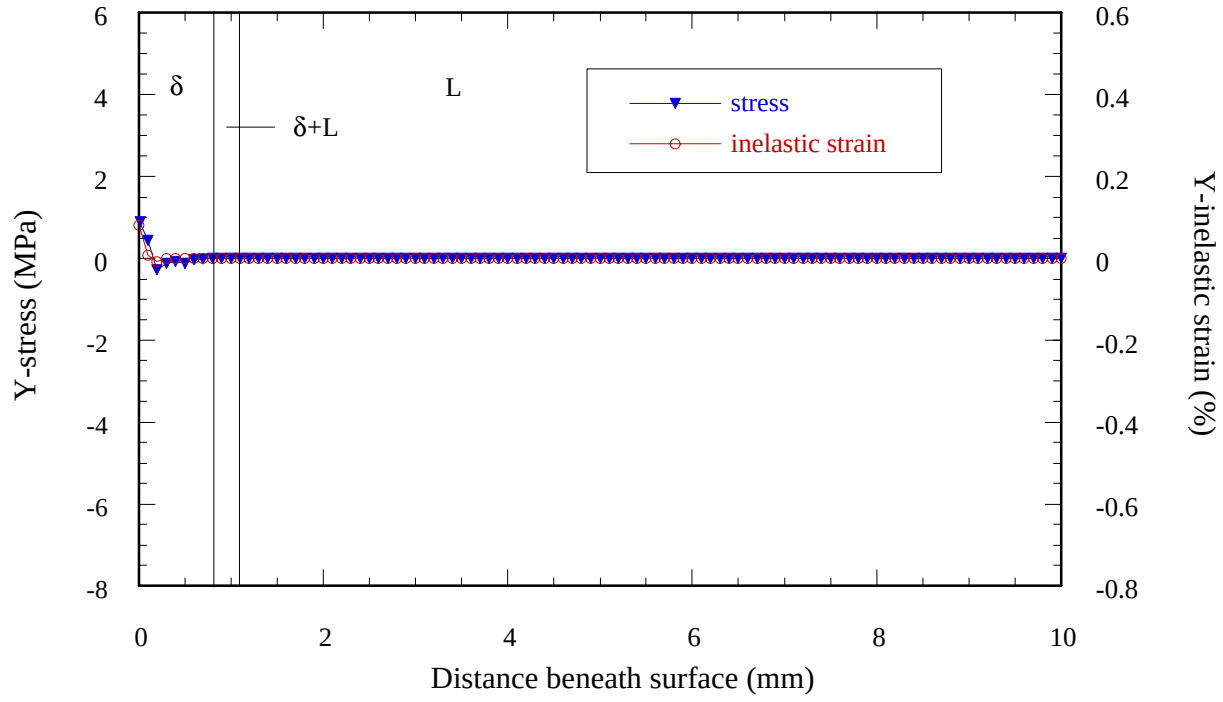

Figure 6.3. Stress / strain evolution of 0.044%C with standard heat flux at 0.5 s

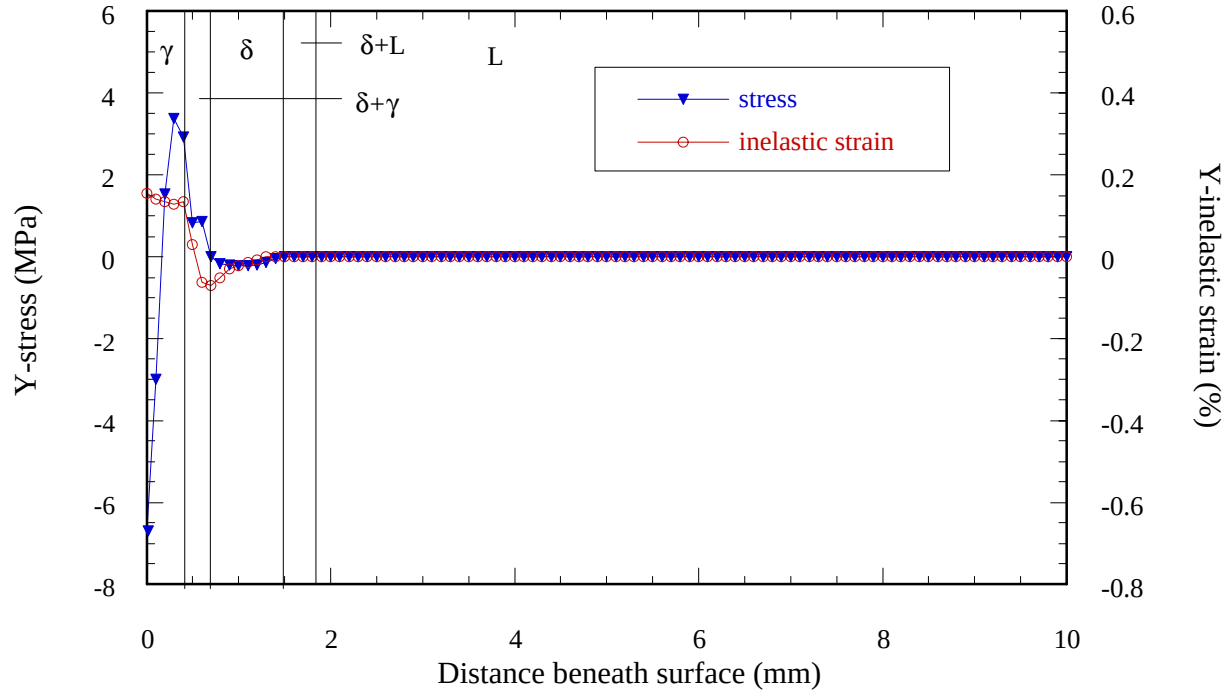

Figure 6.4. Stress / strain evolution of 0.044%C with standard heat flux at 1.0 s

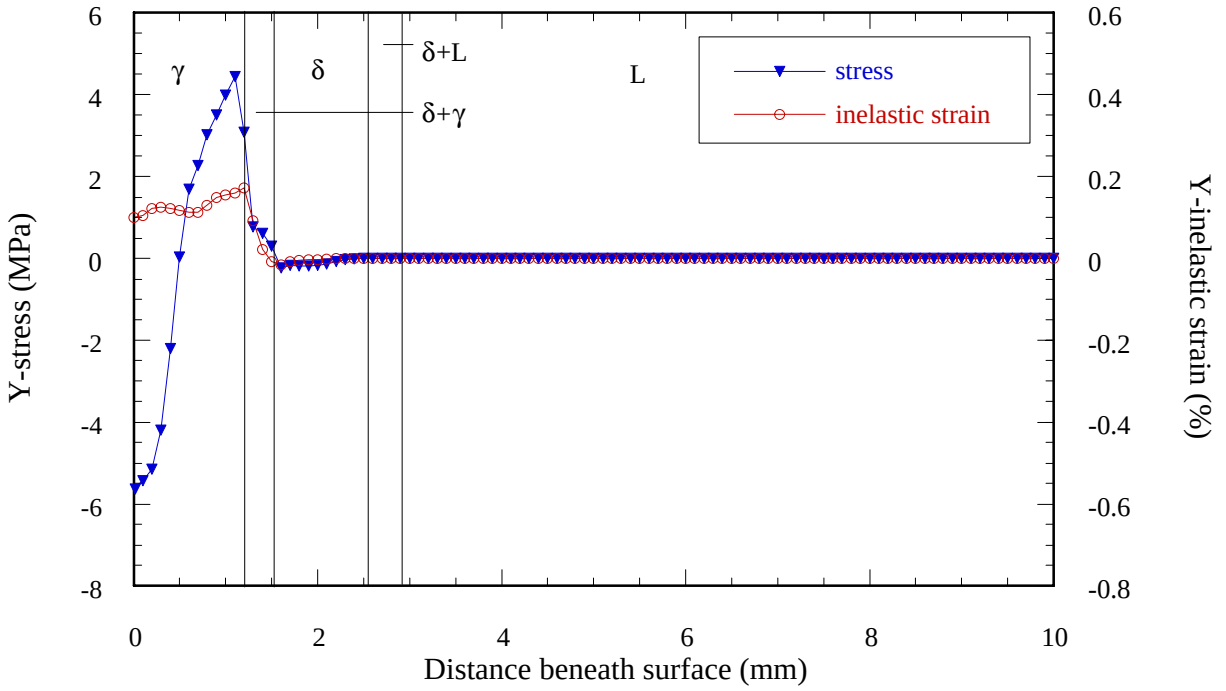

Figure 6.5. Stress / strain evolution of 0.044%C with standard heat flux at 2.0 s

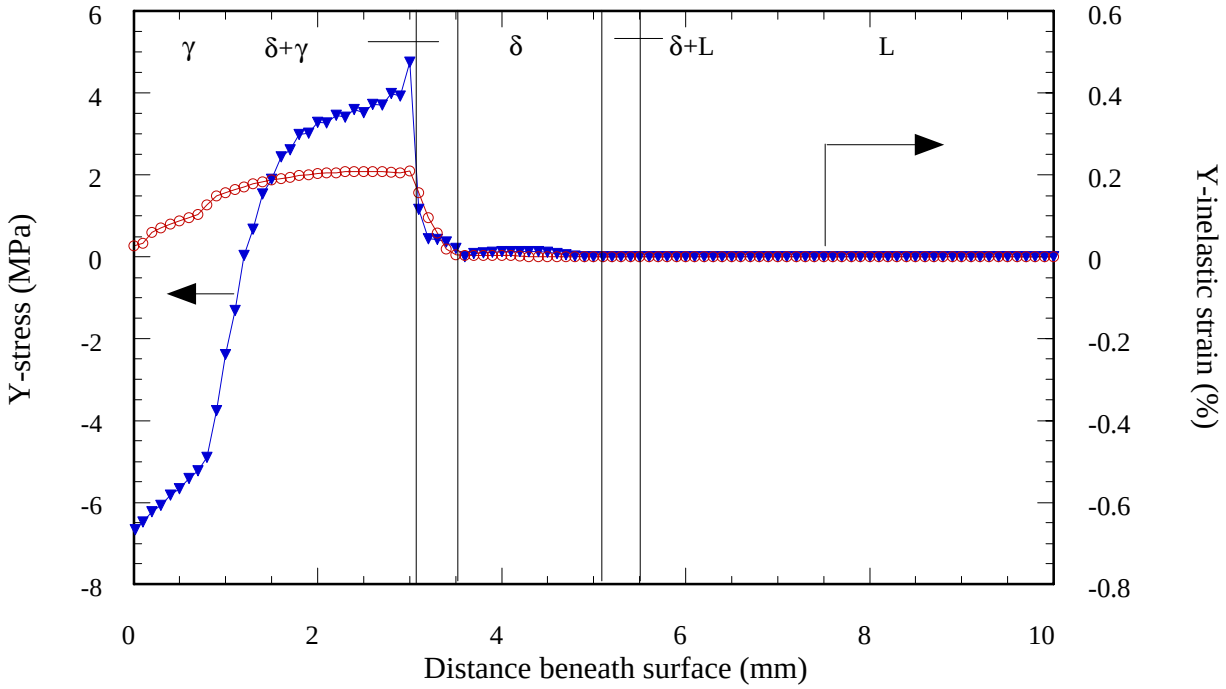

Figure 6.6. Stress / strain evolution of 0.044%C with standard heat flux at 5.0 s

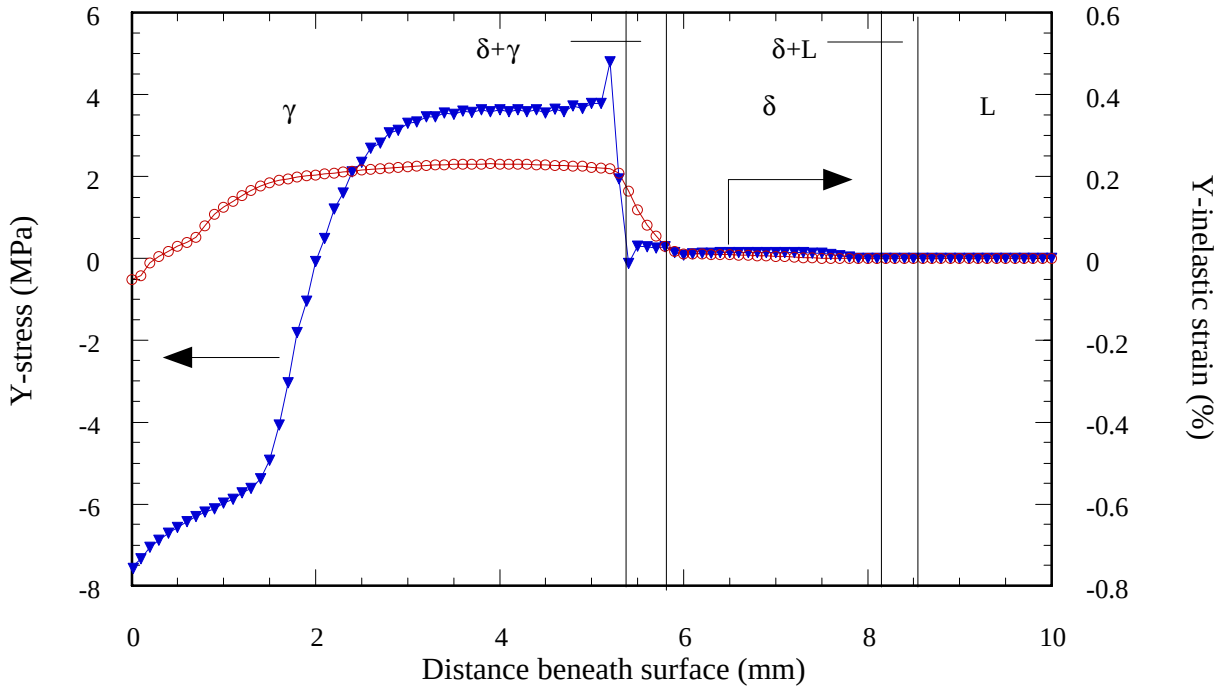

Figure 6.7. Stress / strain evolution of 0.044%C with standard heat flux at 10.0 s

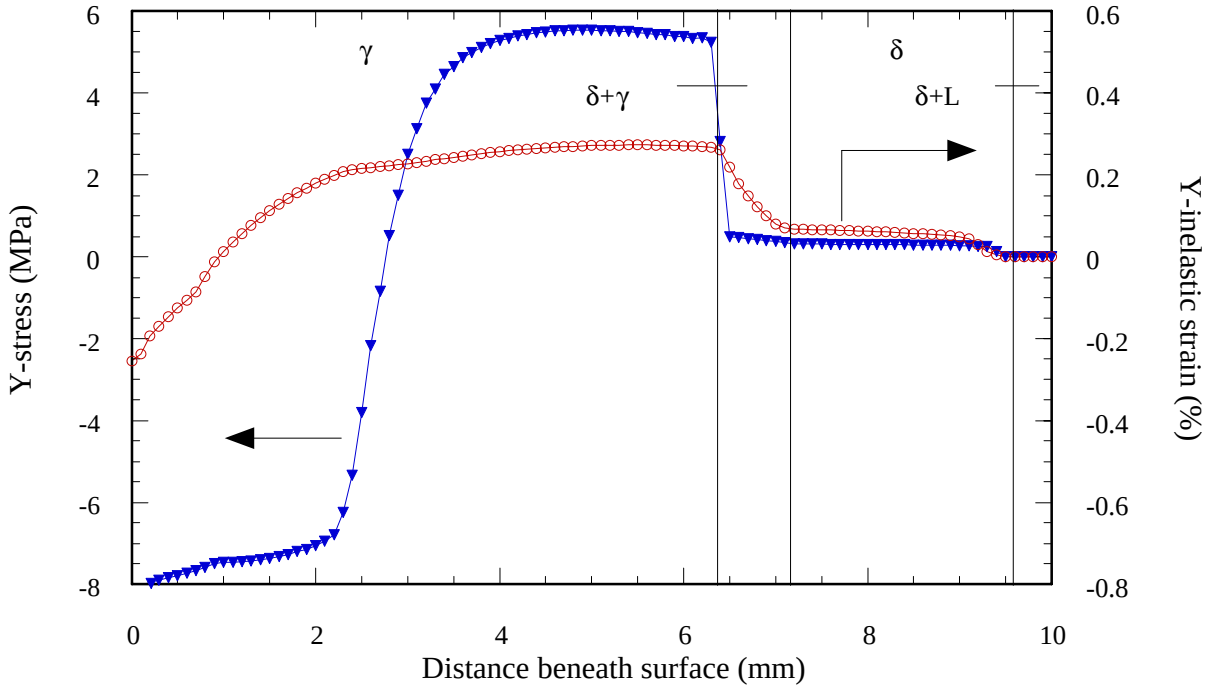

Figure 6.8. Stress / strain evolution of 0.044%C with standard heat flux at 13.0 s

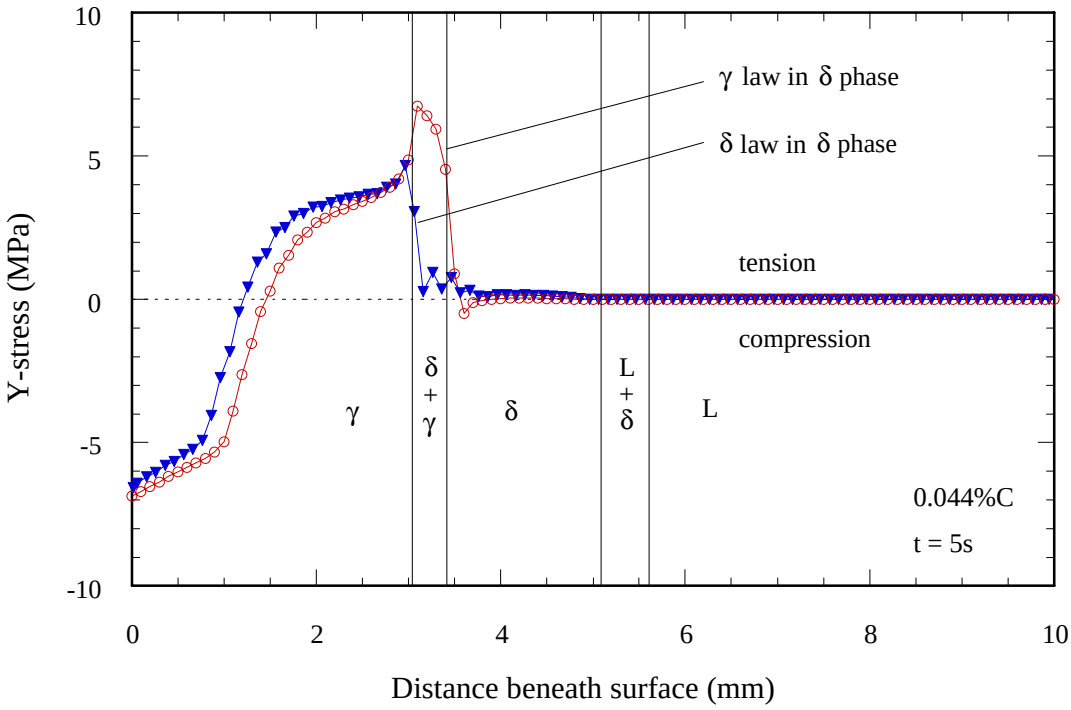

Figure 6.9. Comparison of δ-law constitutive equation on stress / strain development

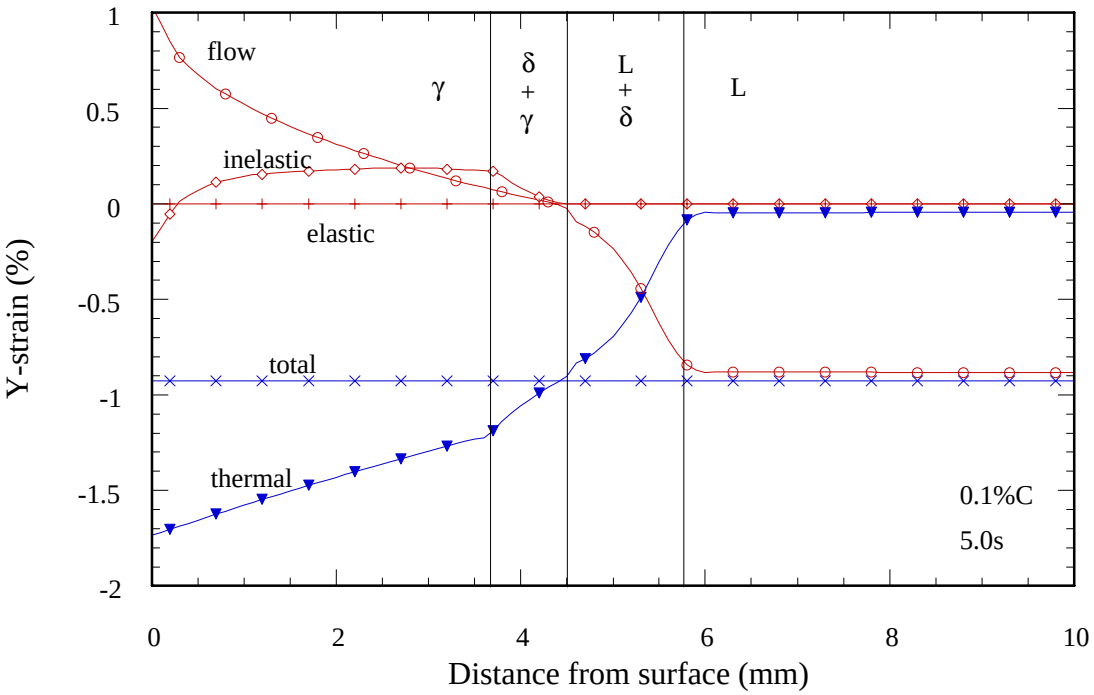

Figure 6.10. Typical strain distributions through shell thickness (0.1%C at 5 s below meniscus)

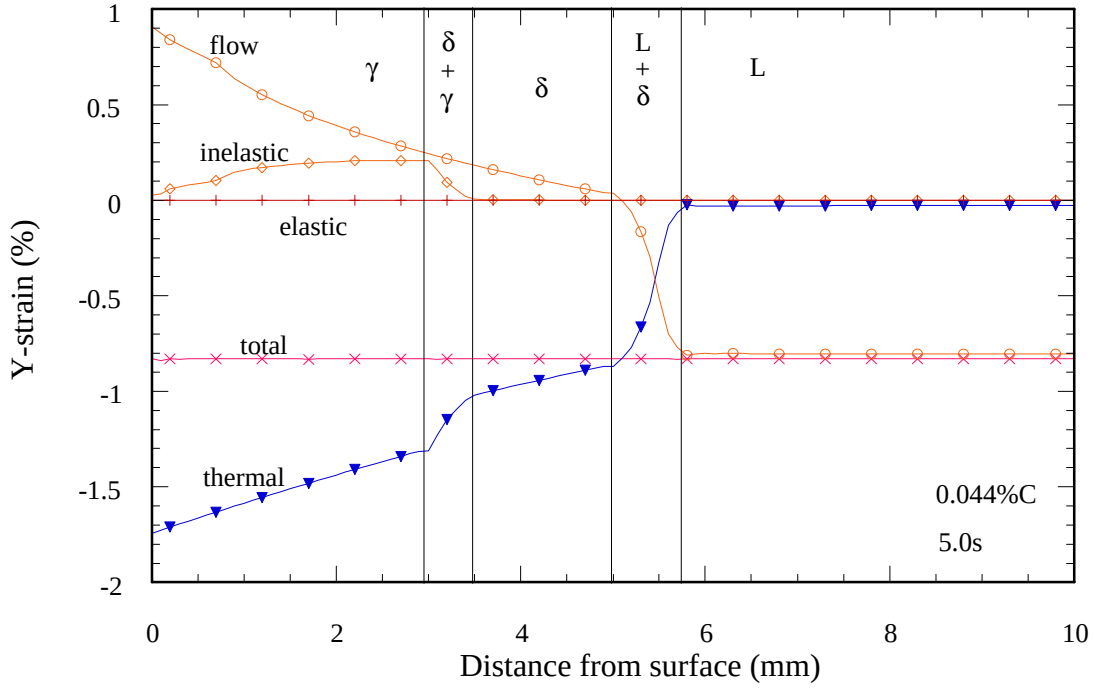

Figure 6.11. Typical strain distributions through shell thickness (0.044%C at 5 s below meniscus)

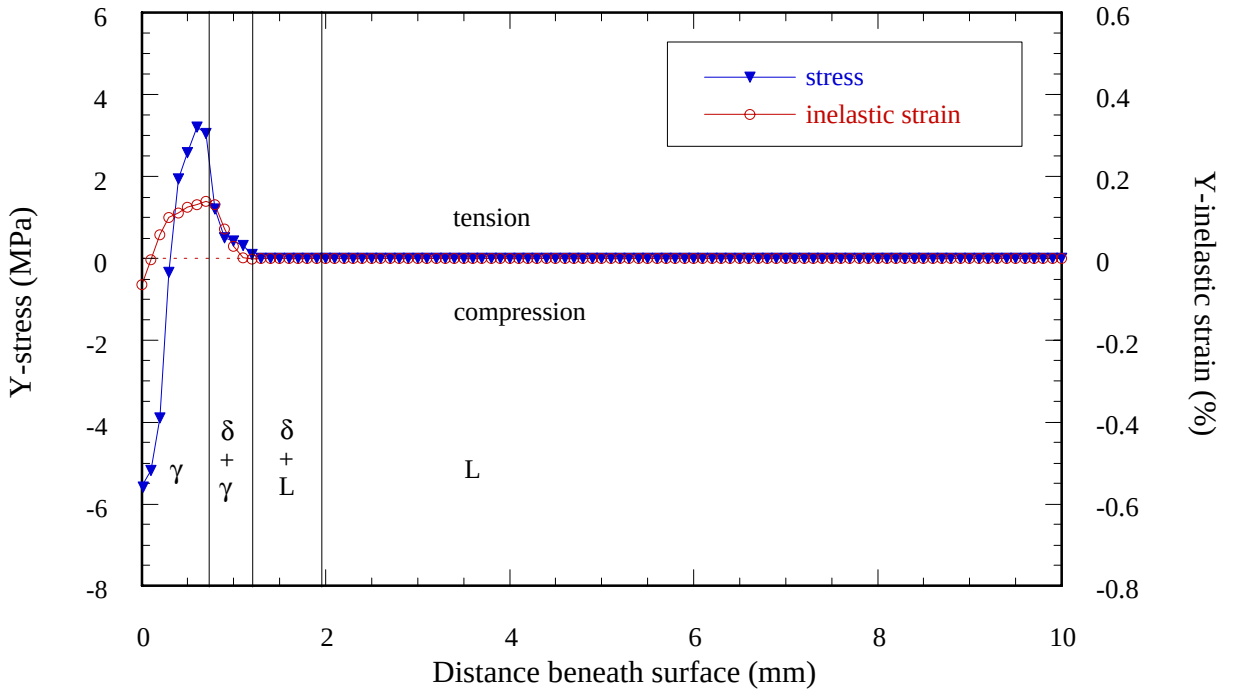

Figure 6.12. Stress / strain evolution of 0.1%C with standard heat flux at 1.0 s

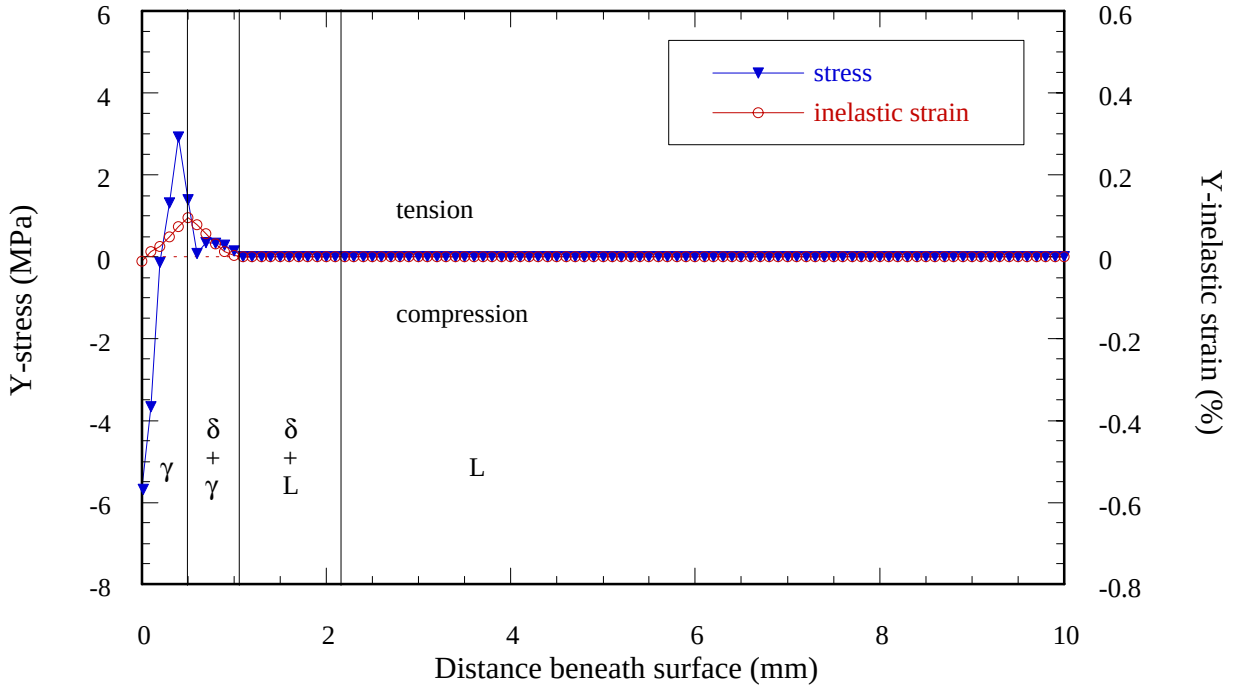

Figure 6.13. Stress / strain evolution of 0.1%C with low heat flux at 1.5 s

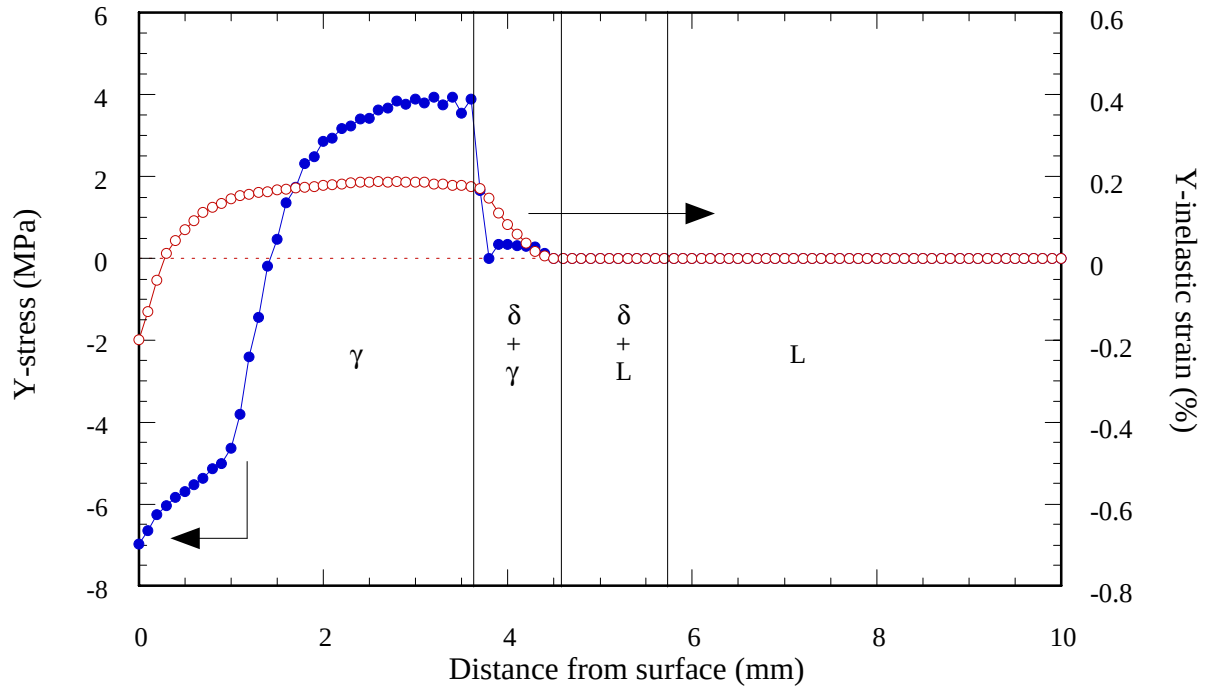

Figure 6.14. Stress / strain evolution of 0.1%C with standard heat flux at 5.0 s

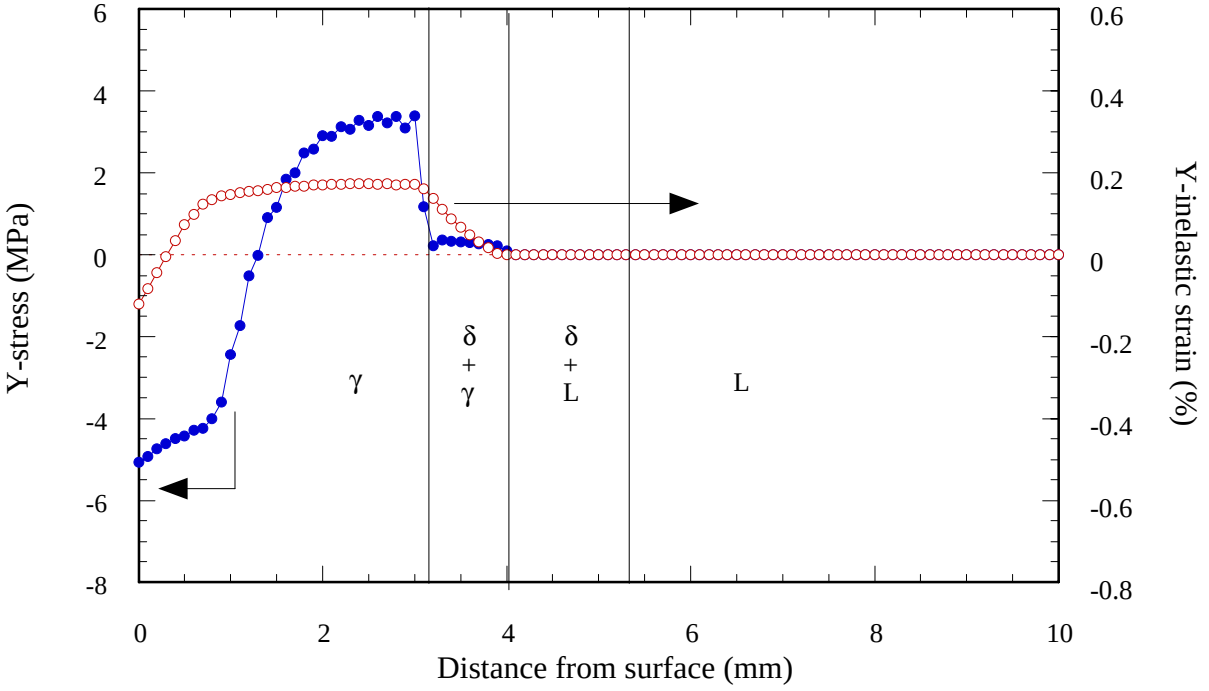

Figure 6.15. Stress / strain evolution of 0.1%C with low heat flux at 6.0 s

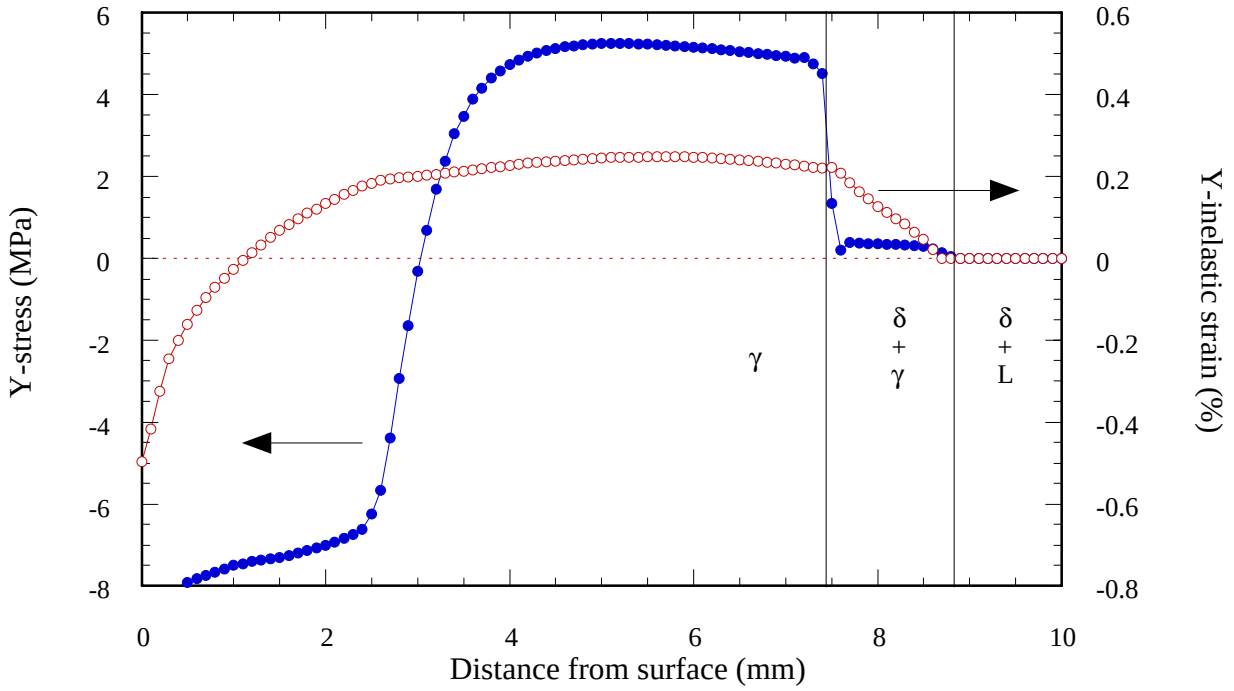

Figure 6.16. Stress / strain evolution of 0.1%C with standard heat flux at 13.0 s

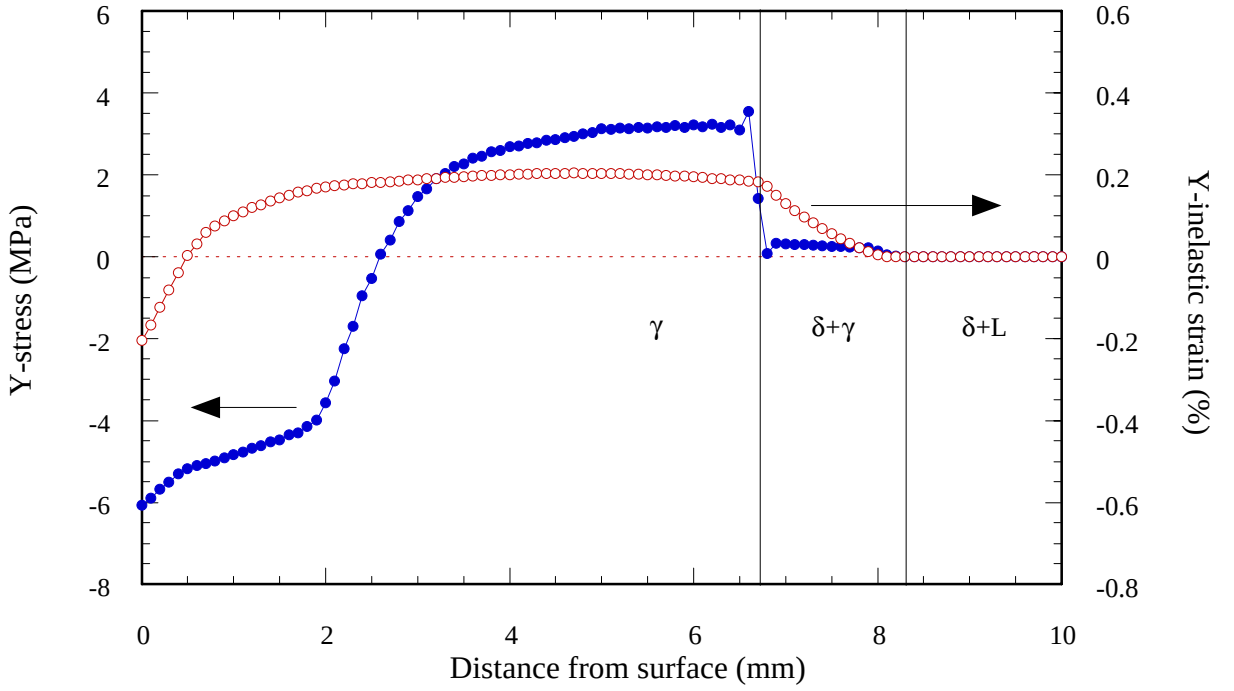

Figure 6.17. Stress / strain evolution of 0.1%C with low heat flux at 15.0 s

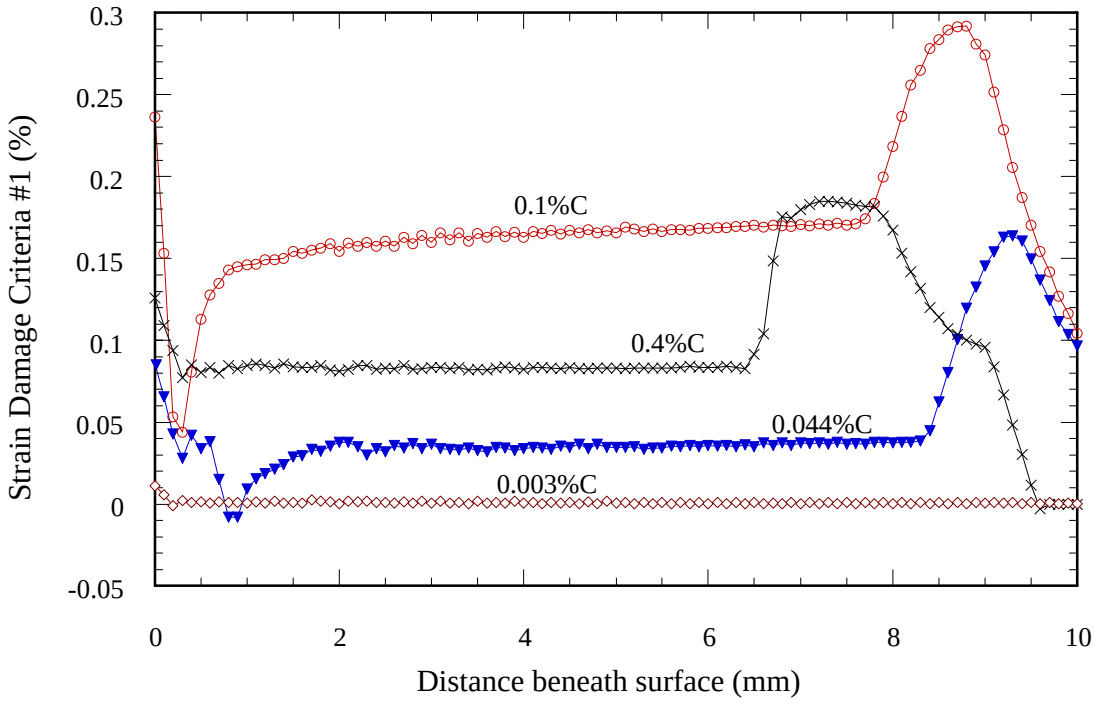

Figure 6.18. Strain damage criteria #1 for various %C with standard heat flux

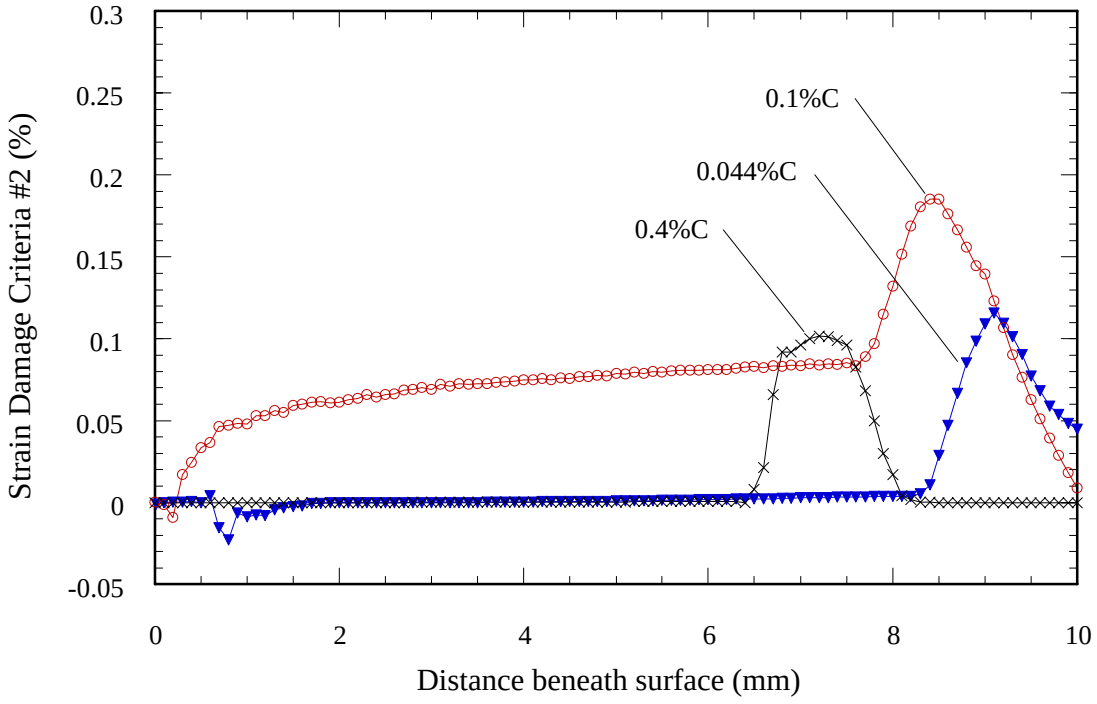

Figure 6.19. Strain damage criteria #2 for various %C with standard heat flux

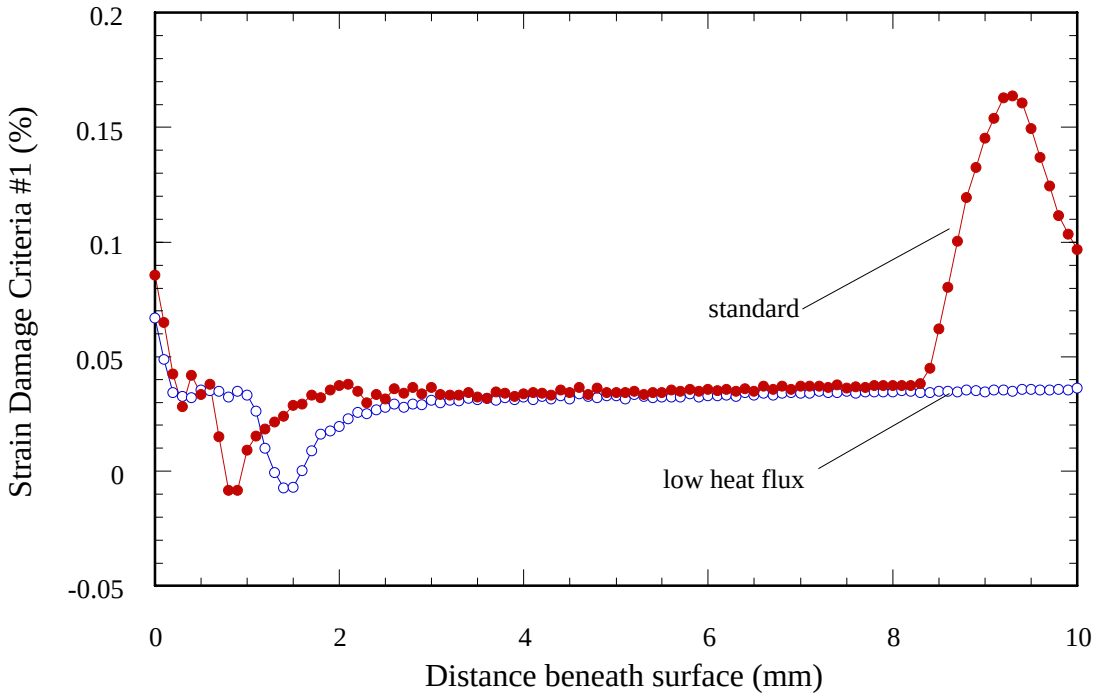

Figure 6.20. Comparison of heat flux on strain damage criteria #1 for 0.044%C

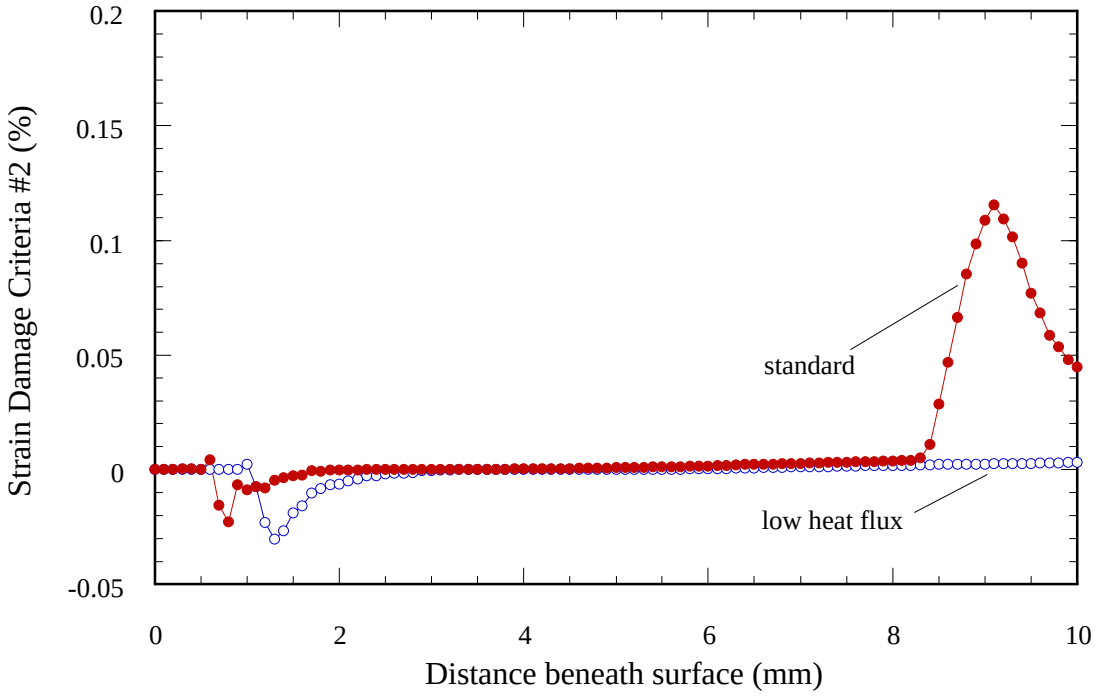

Figure 6.21. Comparison of heat flux on strain damage criteria #2 for 0.044%C

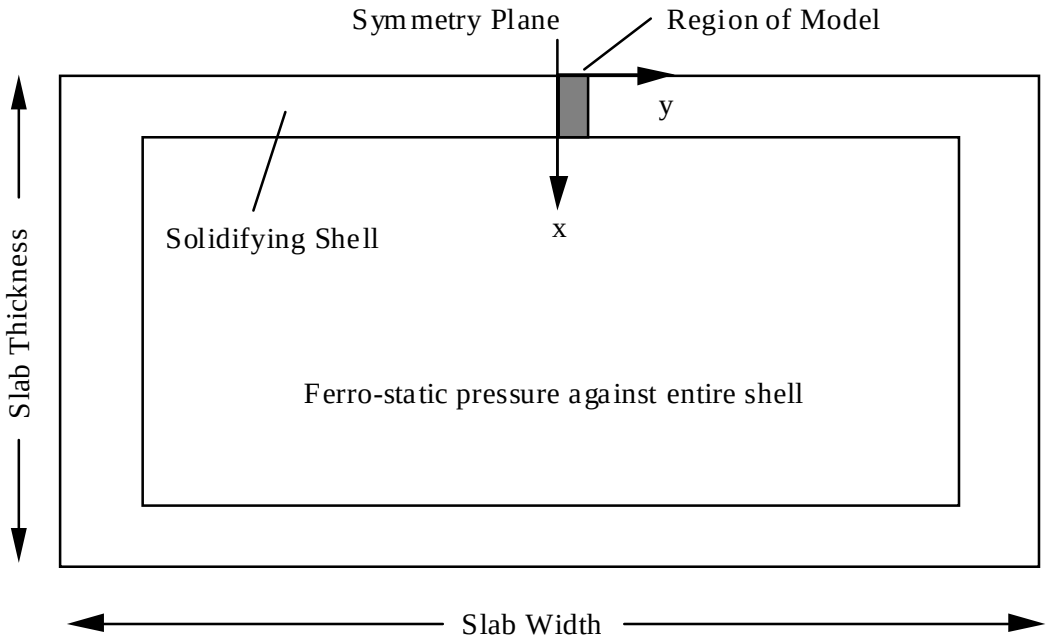

Figure 6.22. Relation of modeled region to continuous cast steel shell

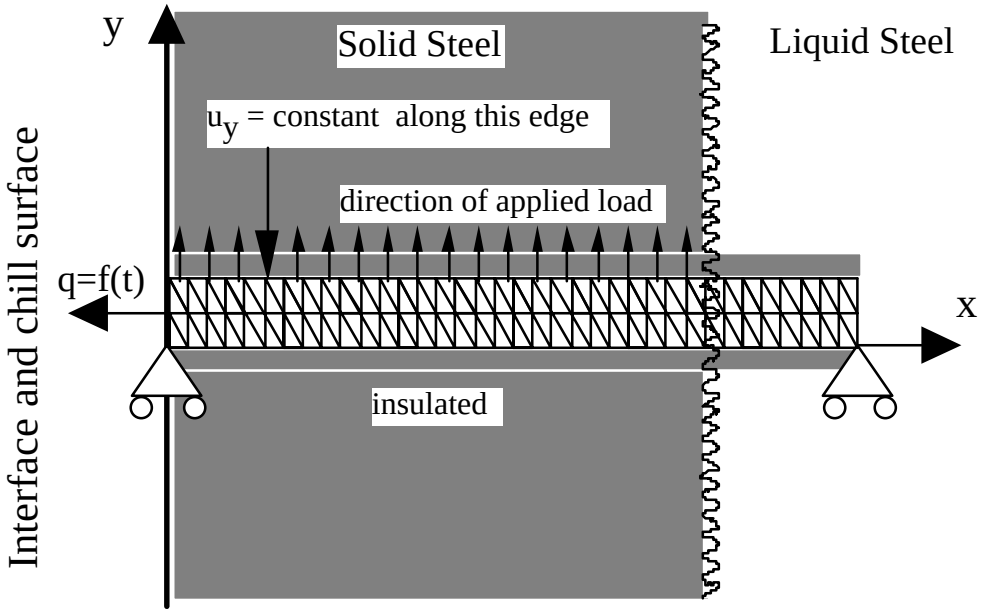

Figure 6.23. Schematic of thin mesh showing boundary conditions and applied load

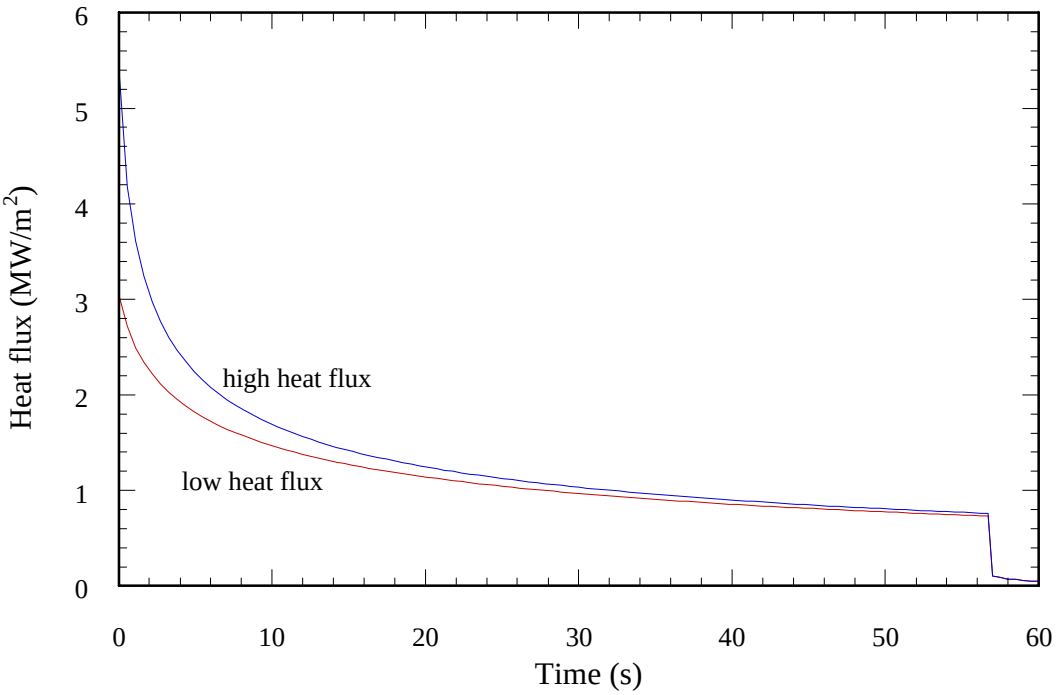

Figure 6.24. Heat flux input curves from CON1D used in taper predictions

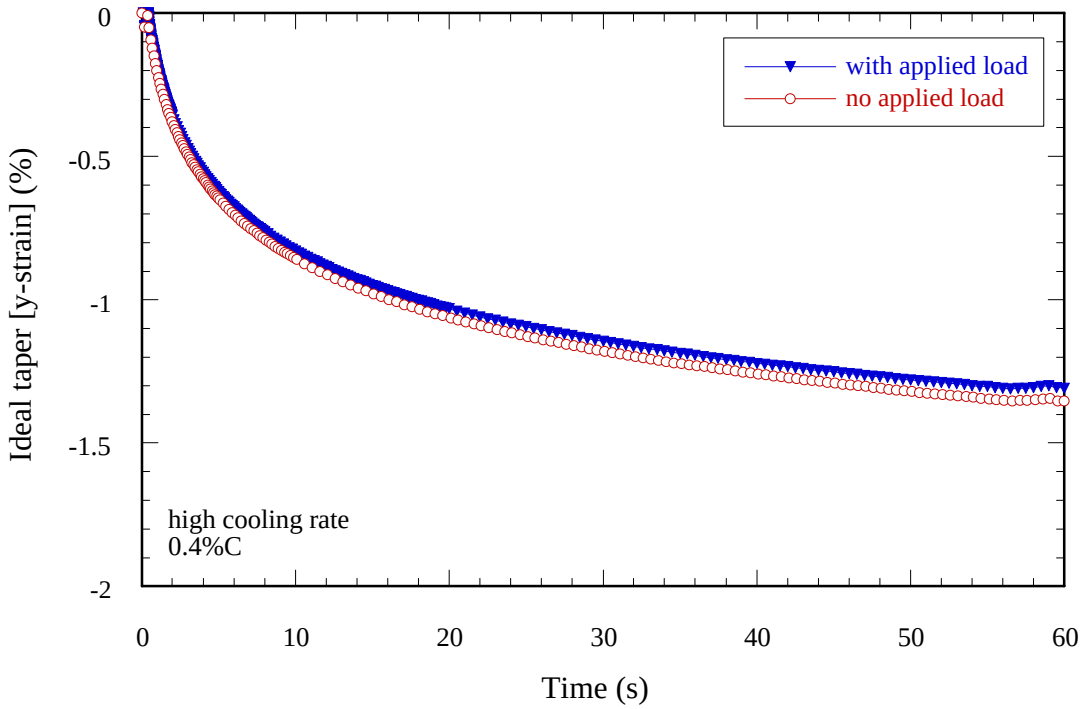

Figure 6.25. Taper calculations comparing effect of resulting ferrostatic pressure

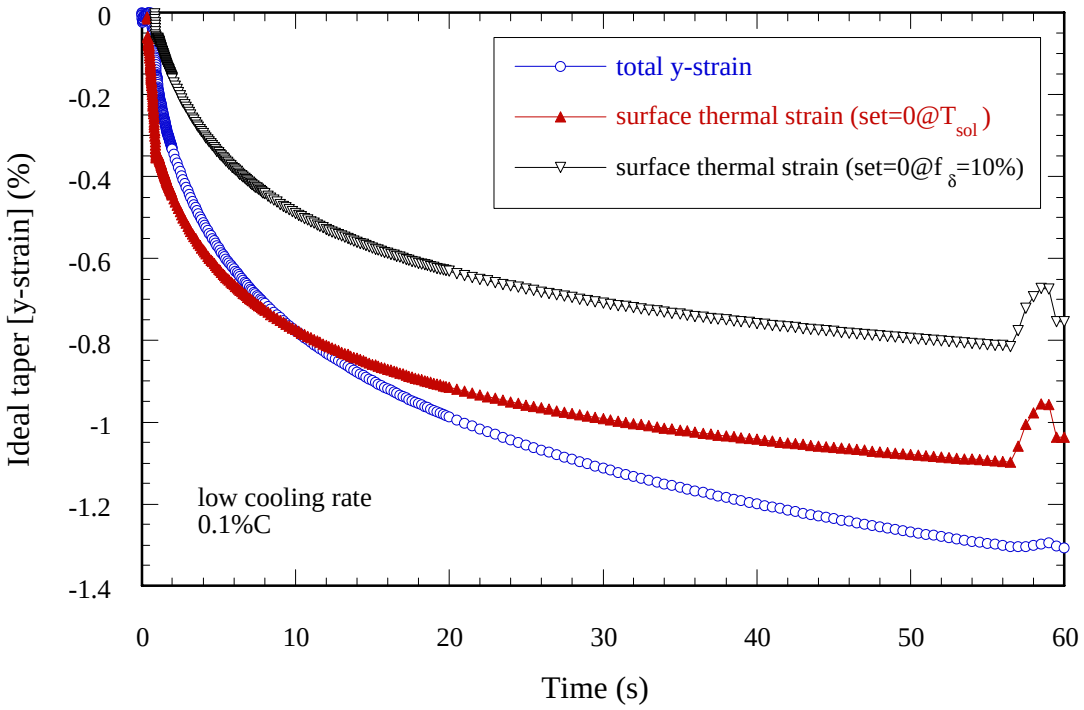

Figure 6.26. Graph displaying taper predictions comparing total and thermal strain

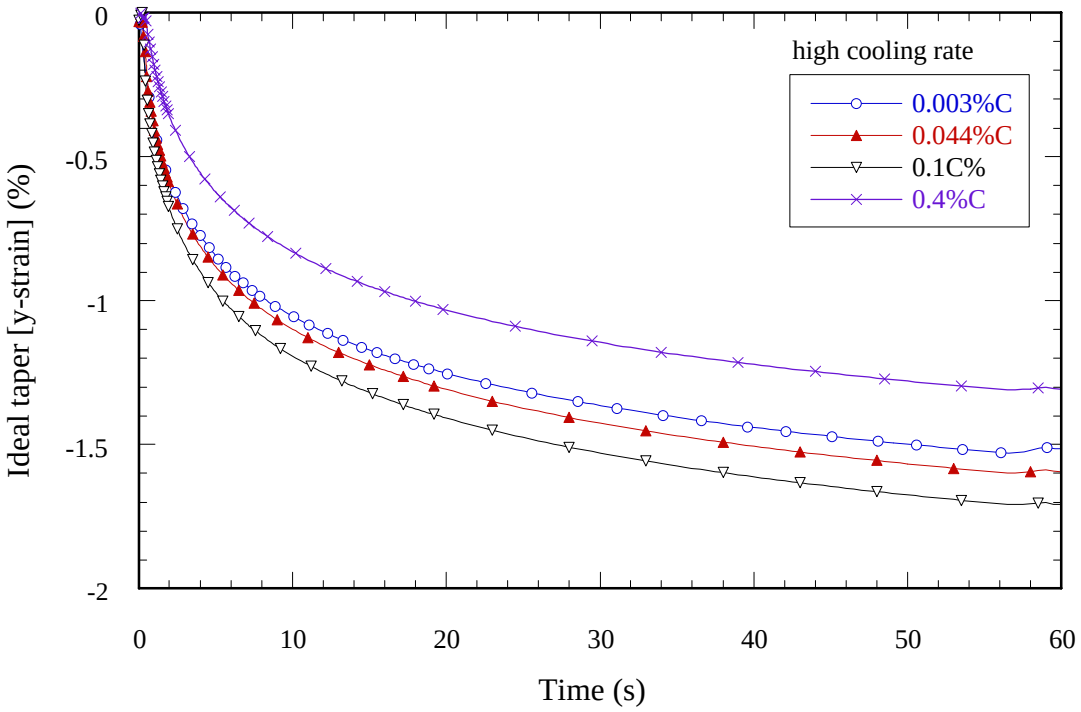

Figure 6.27. Ideal taper predictions with high cooling rate for various carbon content

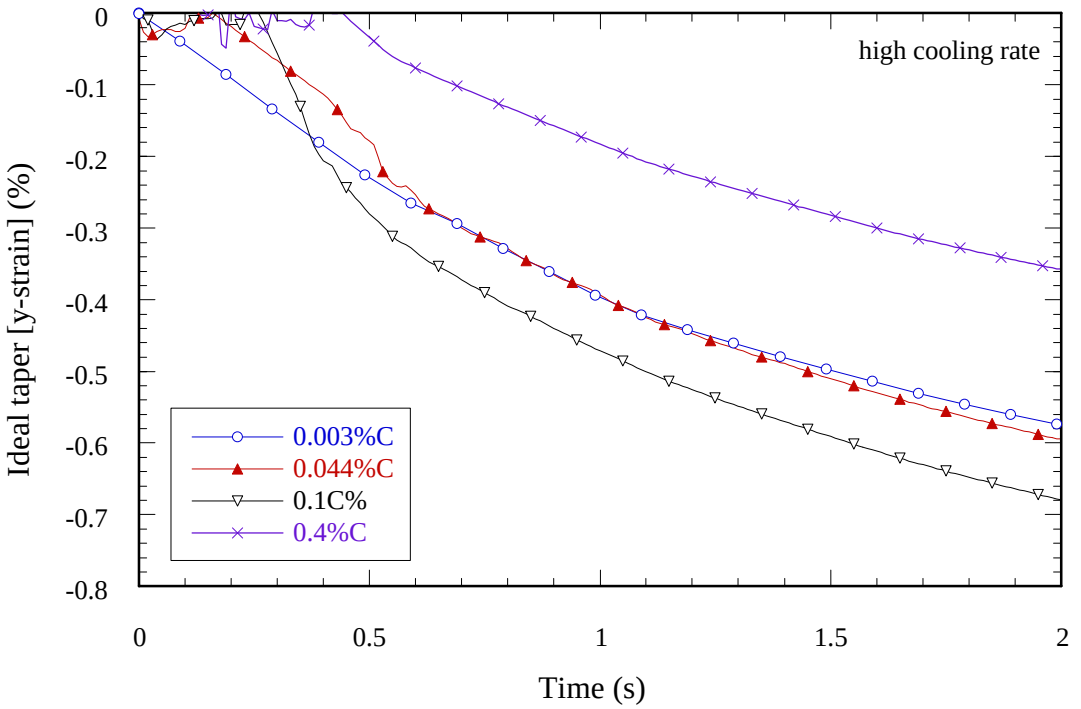

Figure 6.28. Detail of initial taper predictions with high cooling rate

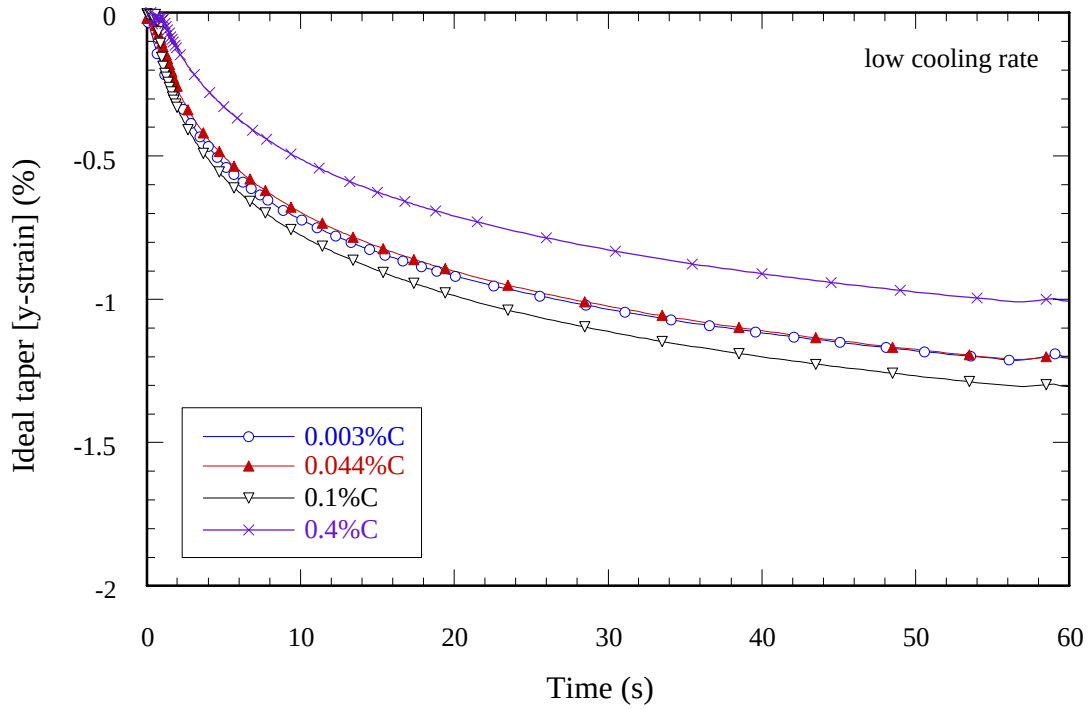

Figure 6.29. Ideal taper predictions with low cooling rate for various carbon content

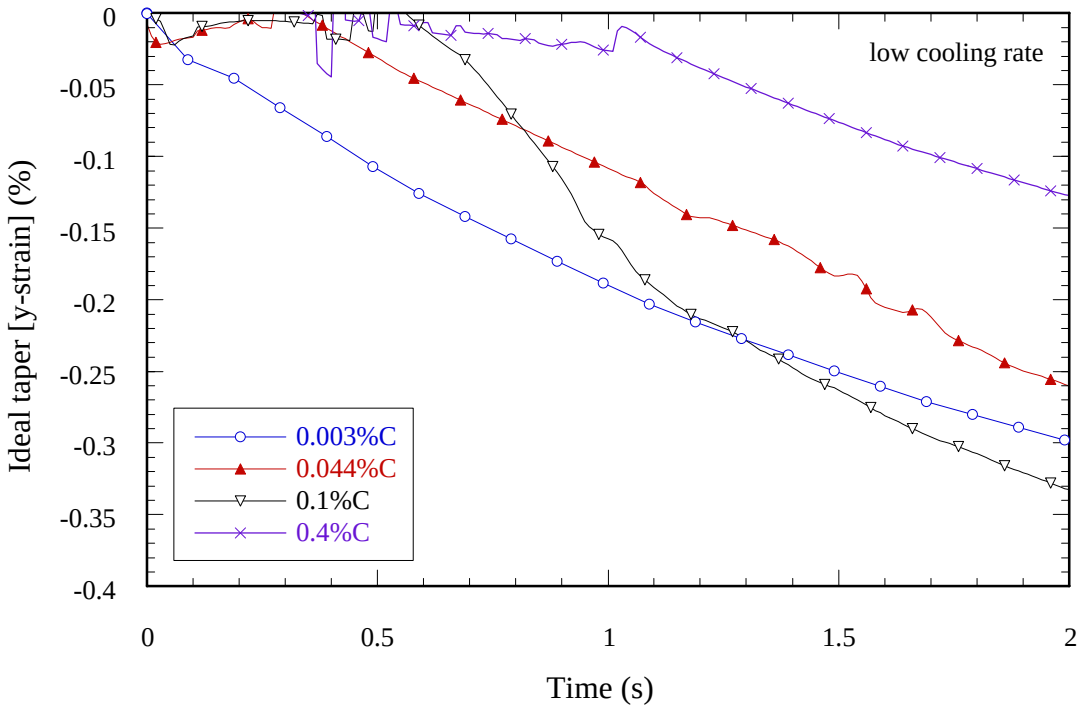

Figure 6.30. Detail of initial taper predictions with low cooling rate

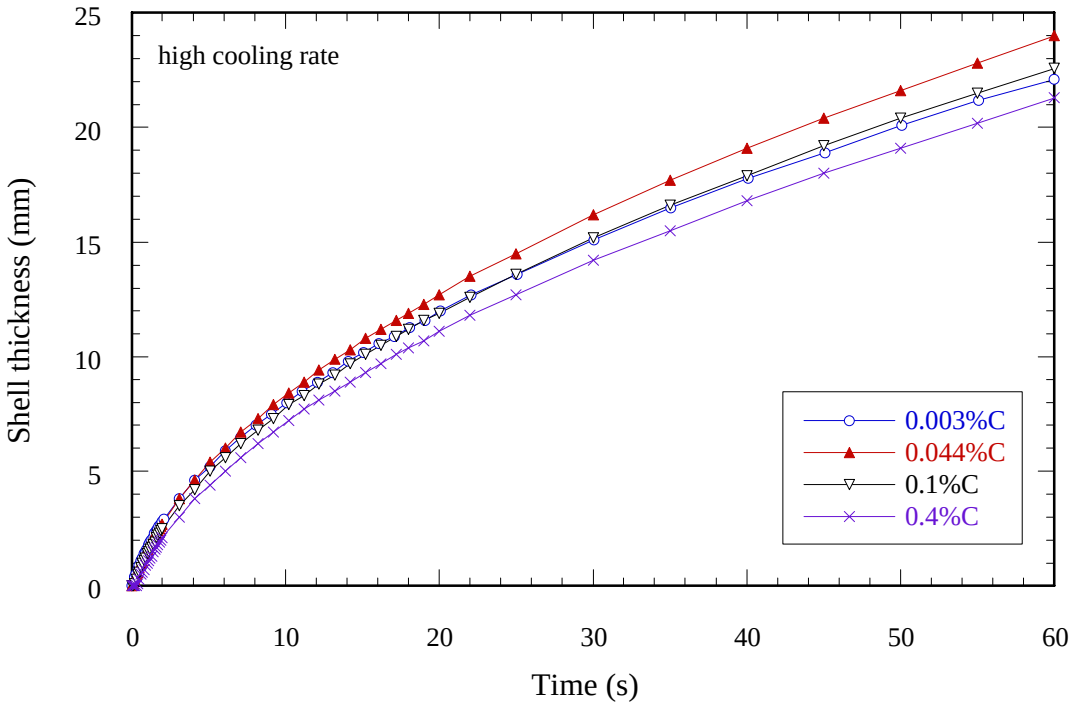

Figure 6.31. Shell growth for various carbon with high cooling rate

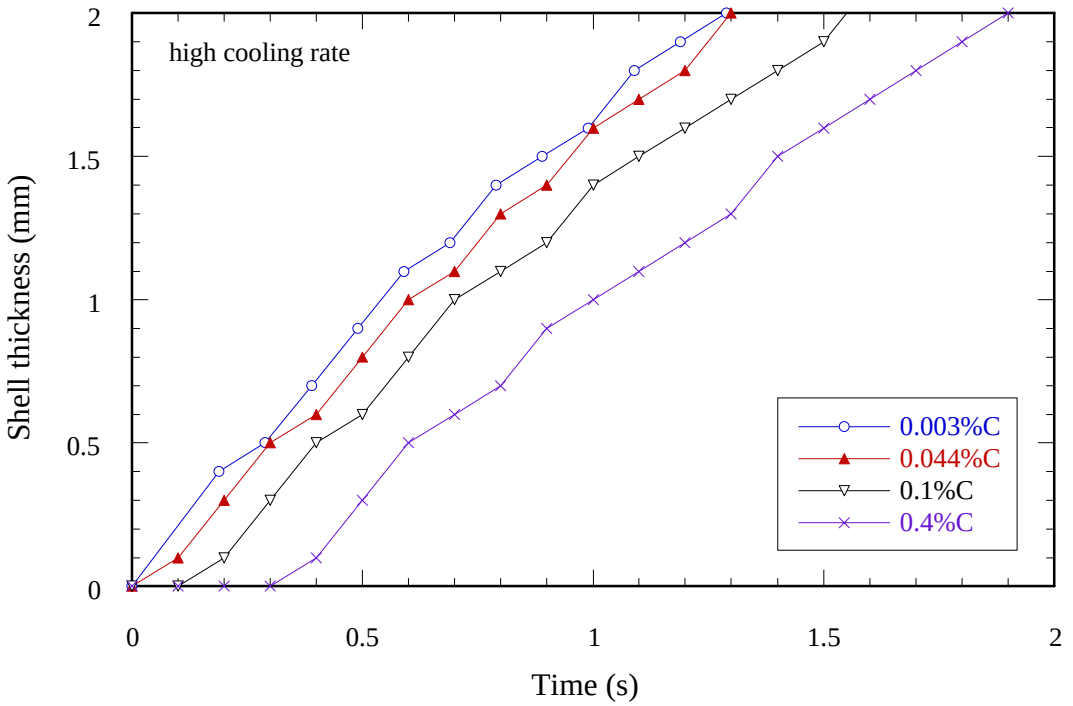

Figure 6.32. Detail of initial shell growth with high cooling rate

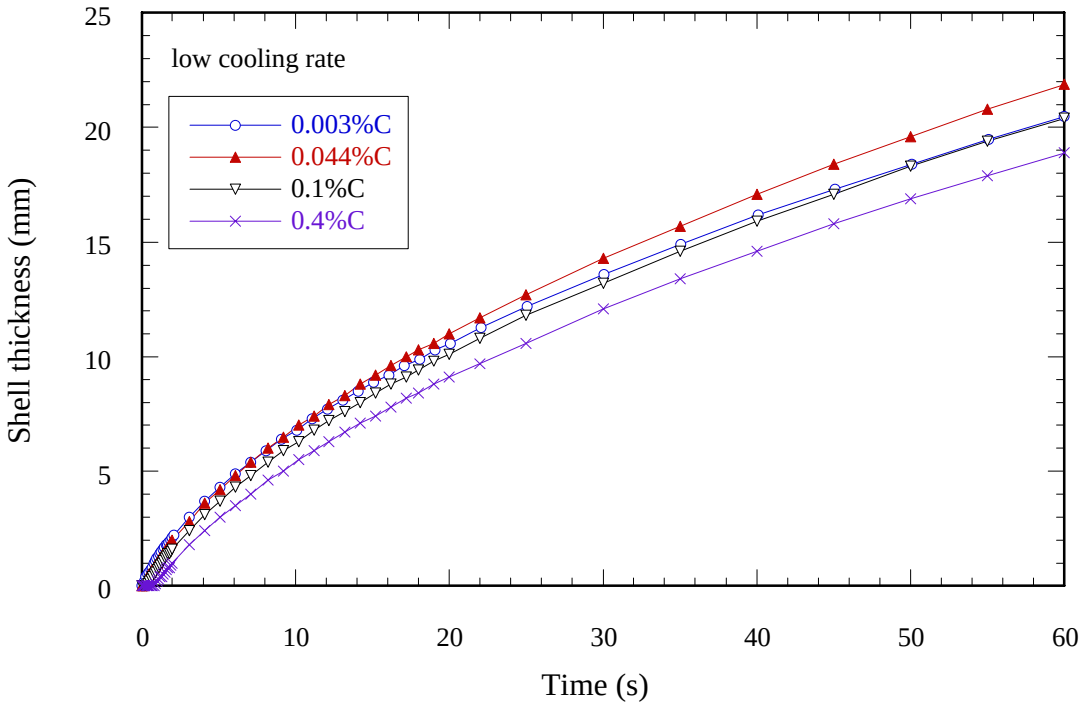

Figure 6.33. Shell growth for various carbon with low cooling rate

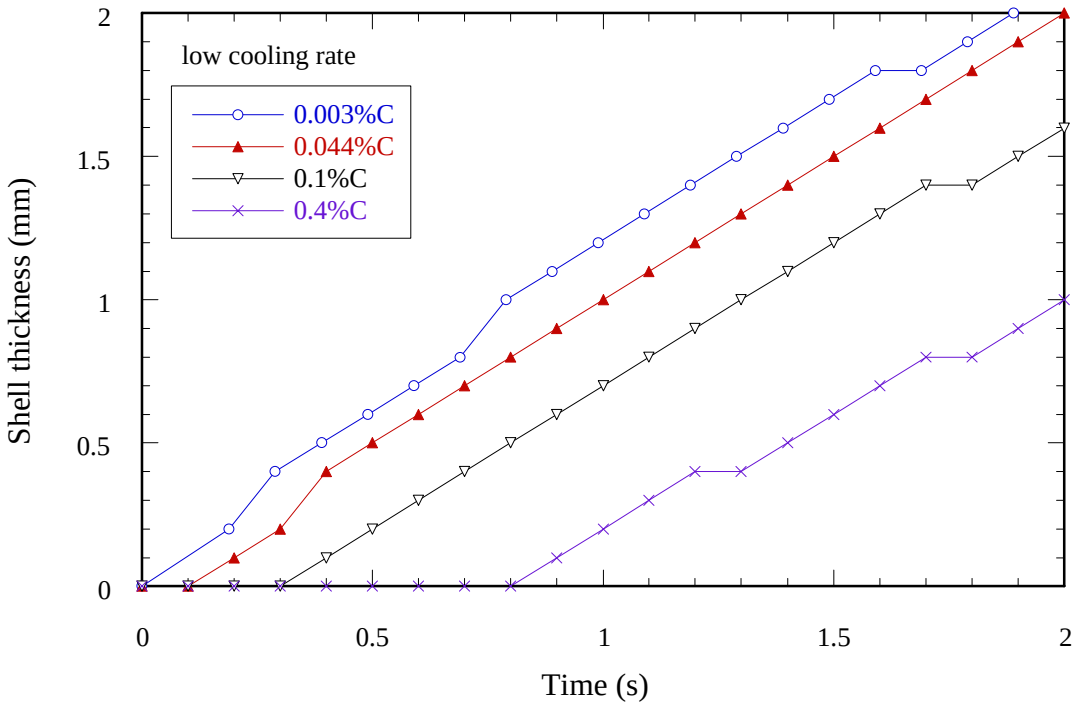

Figure 6.34. Detail of initial shell growth with low cooling rate

7 Summary and Conclusions

A numerically efficient transient thermal-mechanical finite-element model, CON2D [1] has been developed to simulate thermal and mechanical behavior of the solidifying shell during the continuous casting of steel. The robustness of the model makes it ideal for examining early shell solidification. Based on this investigation, the following conclusions can be made:

1) The model contains accurate material property data for all phases of steel based on carbon content and temperature.
2) Accurate temperature dependent elastic-viscoplastic constitutive models have been implemented into CON2D. The models accurately match experimental data for high temperature steel in both the delta and gamma ferrite phases.
3) The model utilizes the bounded Newton-Raphson method to accurately and efficiently integrate the nonlinear visco-elastic-plastic constitutive equations.
4) The model has been validated with a benchmark test problem for thermal-mechanical analysis of solidification with a known analytical solution. This test problem is ideal to evaluate finite-element models for solving mechanical problems with solidification.
5) An extensive amount of work went into the simulation of liquid steel droplets solidifying against a cooled chill. As a first attempt in predicting the final shape of steel droplets the results are very positive. While the results of the droplet experiments and those of the simulations quantitatively vary, the simulation does well in qualitatively predicting the deformation behavior of the droplet as a function of carbon content .
6) Without sticking and with steady cooling conditions, the shell surface goes into compression within 1 second after solidification. Surface cracks grow only if these conditions are not met. The sensitivity of cracks to carbon content and initial cooling rate appears more related to the formation of the non-uniform shell than to direct changes in stress and strain evolution. In the absence of friction, the solid shell contracts on the

order of 1% during the first 5 seconds of solidification. The mismatch in shrinkage generates inelastic strains at the solidification front on the order of 0.1%, which should not be enough for it to cause cracks. Thus, stress concentration and strain localization are required for cracks to form.

7) The δ-ferrite portion of the shell creeps very rapidly, which relaxes all of its stress. Thus, strain in this weak portion of the shell is controlled by the strength of the austenite portion. Creep strain in the weak δ-ferrite and mushy portions of the shell is relatively small, because it is only needed to replace the elastic strain lost by stress relaxation.

7.1 Future Work

A majority of the work in this investigation has been completed in order to validate the techniques and models used within CON2D. Future work should include applying the model to parametric studies on crack, slab width, and taper predictions. The model is also capable of simulating a vertical section domain, which can be used to evaluate transverse phenomena including the effects of meniscus liquid level fluctuations. Future work should also include continuous improvement to the model. Such improvements may include the addition of more accurate constitutive equations and or the addition of property models allowing for the simulation of other grades.

References

1. Thomas, B.G., University of Illinois at Urbana-Champaign, "CON2D User's Manual," (1994).

2. Zhu, H., "Coupled Thermal-Mechanical Fixed-Grid Finite-Element Model with Application to Initial Solidification," Ph.D Thesis, University of Illinois at Urbana-Champaign (1997).

3. Moitra, A., "Thermo-mechanical model of Steel Shell Behavior in Continuous Casting," Ph.D. Thesis, University of Illinois at Urbana-Champaign (1993).

4. Singh, S.N. and K.E. Blazek, "Heat Transfer and Skin Formation in a Continuous Casting Mold as a Function of Steel Carbon Content." J. Metals, 1974. 26: p. 17-27.

5. Grill, A., J.K. Brimacombe, and F. Weinberg, "Mathematical Analysis of Stresses in Continuous Casting of Steel." Ironmaking Steelmaking, 1976. 3(1): p. 38-47.

6. Saeki, T., et al., "Effect of Irregularity in Solidified Shell Thickness on Longitudinal Surface Cracks in CC Slabs." Tetsu to Hagane, 1982. 68(13): p. 1773-1782.

7. Suzuki, T., K.H. Tacke, K. Wunnenberg, and K. Schwerdtfeger, "Creep Properties of Steel at Continuous Casting Temperatures." Ironmaking Steelmaking, 1988. 15(2): p. 90-100.

8. Ye, C.H., M. Suzuki, H. Shibata, and T. Emi, "Simulation of Crack Formation on Solidifying Steel Sheel in Continuous Casting Mold." ISIJ Internat., 1996. 36: p. S159-S162.

9. Thomas, B.G. and J.T. Parkman. "Simulation of Thermal Mechanical Behavior During Initial Solidification," in Thermec 97 Internat. Conf. on Thermomechanical Processing of Steel and Other Materials. 1997. Wollongong, Australia: TMS.

10. Wolf, M. and W. Kurz, "The Effect of Carbon Content on Solidification of Steel in the Continuous Casting Mold." Metall. Trans. B, 1981. 12B(3): p. 85-93.

11. Mahapatra, R.B., J.K. Brimacombe, and I.V. Samarasekera, "Mold Behavior and its Influence on Product Quality in the Continuous Casting of Slabs: Part II. Mold Heat Transfer, Mold Flux Behavior, Formation of Oscillation Marks, Longitudinal Off-corner Depressions, and Subsurface Cracks." Metallurgical Transactions B, 1991. 22B(December): p. 875-888.

12. Cramb, A.W. and F.J. Mannion, "The measurements of meniscus marks at Bethlehem Steel's Burns Harbor slab caster,", in Steelmaking Proceedings. 1985, Iron and Steel Society: Warrendale, PA. p. 349-359.

13. Thomas, B.G., D. Lui, and B. Ho, "Effect of Transverse and Oscillation Marks on Heat Transfer in the Continuous Casting Mold,", in Applications of Sensors in Materials Processing, V. Viswanathan, Editor. 1997, TMS, Warrendale, PA: Orlando, FL. p. 117-142.

14. Suzuki, M., et al., "Origin of Heat Transfer Anomaly and Solidifying Shell Deformation of Peritectic Steels in Continuous Casting." ISIJ Internat., 1996. 36: p. S171-S174.

15. Bennett, T. and D. Poulikakos, "Heat Transfer Aspects of Splat-quench Solidification: Modeling and Experiment." Journal of Materials Science, 1994. 29: p. 2025-2039.

16. Trapaga, G., E.F. Matthys, J.J. Valencia, and J. Szekely, "Fluid Flow, Heat Transfer, and Solidification of Molten Melal Droplets Impinging on Substrates: Comparison of Numerical and Experimental Results." Metallurgical Transactions B, 1992. 23B: p. 701-718.

17. Liu, W., G.X. Wang, and E.F. Matthys, "Thermal Analysis and Measurements for a Molten Metal Drop Impacting On a Substrate: Cooling, Solidification and Heat Transfer Coefficient." Int. J. Heat Mass Transfer, 1995. 38(8): p. 1387-1395.

18. Wang, G.X. and E.F. Matthys, "Experimental Investigation of Interfacial Thermal Conductance for Molten Metal Solidification on a Substrate." J. Heat Transfer, 1996. 118(Feb.): p. 157-163.

19. Wang, G.X. and E.F. Matthys, "Modeling of Heat Transfer and Solidification During Splat Cooling: Effect of Splat Thickness and Splat/Substrate Thermal Contact." International Journal of Rapid Solidification, 1991. 6: p. 141-174.

20. Dong, S., E. Niyama, and K. Anzai, "Free Deformation of Initial Solid Shell of Fe-C Alloys." ISIJ Internat., 1995. 35(6): p. 730-736.

21. Todoroki, H., R. Lertarom, T. Suzuki, and A. Cramb. "Heat Transfer Behavior of Pure Iron and Nickel against a Water Cooled Copper Mold During Initial Stage of Solidification," in Steelmaking Proceedings. 1997. Chicago, IL: Iron and Steel Society.

22. Mizukami, H., S. Hiraki, M. Kawamoto, and T. Watanabe, "Initial Solidification Behavior of Ultra Low, Low and Middle Carbon Steel." ISIJ International, 1999. 39(12): p. 1262-1269.

23. Bernhard, C., H. Hiebler, and M. Wolf, "Simulation of Shell Strength Properties by the SSCT Test." ISIJ Internat., 1996. 36: p. S163-S166.

24. Suzuki, M., M. Suzuki, C. Yu, and T. Emi, "In-Situ Measurement of Fracture Strength of Solidifying Steel Shells to Predict Upper Limit of Casting Speed in Continuous Caster with Oscillating Mold." ISIJ International, 1997. 37(4).

25. Moitra, A., B.G. Thomas, and W. Storkman. "Thermo-mechanical model of Steel Shell Behavior in the Continuous Casting Mold," in Proceedings of TMS Annual Meeting. 1992. San Diego, CA: The Minerals, Metals, and Materials Society, Warrendale, PA.

26. Thomas, B.G., "Mathematical Modeling of the Continuous Slab Casting Mold: a State of the Art Review,", in Mold Operation for Quality and Productivity, A. Cramb, Editor. 1991, Warrendale, PA: Iron and Steel Society. p. 69-82.

27. Samarasekera, I.V. and J.K. Brimacombe, "Application of Mathematical Models for Improvement of Billet Quality,", in Steelmaking Conference. 1991, Iron and Steel Society: Warrendale, PA. p. 91-103.

28. Puhringer, O.M., "Strand Mechanics for Continuous Slab Casting Plants." Stahl Eisen, 1976. 96(6): p. 279-284.

29. Grill, A. and K. Schwerdtfeger, "Finite-element analysis of Bulging Produced by Creep in Continuously Cast Steel Slabs." Ironmaking Steelmaking, 1979. 6(3): p. 131-135.

30. Barber, B., B.A. Lewis, and B.M. Leckenby, "Finite-element Analysis of Strand Deformation and Strain Distribution in Solidifying Shell During Continuous Slab Casting." Ironmaking Steelmaking, 1985. 12(4): p. 171-175.

31. Dalin, J.B. and J.L. Chenot, "Finite element computation of bulging in continuously cast steel with a viscoplastic model." Int. J. for Num. Meth. in Eng., 1988. 25: p. 147-163.

32. Okamura, K. and H. Kawashima, "Three-dimensional Elasto-Plastic and Creep Analysis of Bulging in Continuously Cast Slabs." ISIJ International, 1989. 29(8): p. 666-672.

33. Kinoshita, K., T. Emi, and M. Kasai, "Thermal Elasto-plastic Stress Analysis of Solidifying Shell in Continuous Casting Mold." 1979. 65(9): p. 40-49.

34. Rammerstorfer, F.G., C. Jaquemar, D.F. Fisher, and H. Wiesinger. "Temperature fields, solidification progress and stress development in the strand during a continuous casting process of steel," in Numerical Methods in Thermal Problems. 1979. Pineridge Press Limited, Swansea, U.K.

35. Kinoshita, K., T. Emi, and e. al, Kawasaki Steel Corp., Japan, "Numerical Analysis of Heat Transfer and Stress in Solidifying Shell within the Mold of Continuous Casting," (1980).

36. Kinoshita, K., H. Kitaoka, and T. Emi, "Influence of Casting Conditions on the Solidification of Steel Melt in Continuous Casting Mold." Tetsu-to-Hagane, 1981. 67(1): p. 93-102.

37. Sorimachi, K., M. Shiraishi, and K. Kinoshita. "Continuous Casting of High Carbon Steel Slabs at Chiba Works," in 2nd Process Tech. Div. Conference. 1981. Chicago, IL:

38. Ohnaka, I. and Y. Yashima. "Stress Analysis of Steel Shell Solidifying in Continuous Casting Mold," in Modeling of Casting and Welding Processes IV. 1988. Palm Coast, FL: Engineering Foundation Conference Proceedings.

39. Storkman, W.R. and B.G. Thomas. "Mathematical Models of Continuous Slab Casting to Optimize Mold Taper," in Modeling of Casting and Welding Processes. 1988. Palm Coast, FL: Engineering Foundation.

40. Thomas, B.G., "Application of Mathematical Models to the Continuous Slab Casting Mold." ISS Trans., 1989. 16(12): p. 53-66.

41. Storkman, W.R., "Optimization of Mold Taper Design Using Mathematical Models of Continuous Steel Slab Casting," Masters Thesis, University of Illinois (1990).

42. Thomas, B.G., A. Moitra, and W.R. Storkman, "Optimizing Taper in Continuous Slab Casting Molds Using Mathematical Models,", in Proceedings, 6th International Iron and Steel Congress. 1990, Iron & Steel Inst. Japan, Tokyo: Nagoya, Japan. p. 348-355.

43. Kristiansson, J.O., "Thermal stresses in the early stage of solidification of steel." J. of Thermal Stresses, 1982. 5: p. 315-330.

44. Kristiansson, J.O., "Thermomechanical Behavior of the Solidifying Shell Within Continuous-Casting Billet Molds - A Numerical Approach." J. of Thermal Stresses, 1984. 7: p. 209-226.

45. Kozlowski, P., "Simple, Unified Constitutive Equations for Plain Carbon Steel Under Continuous Casting Conditions," Masters Thesis, University of Illinois at Urbana-Champaign (1991).

46. Kozlowski, P., B.G. Thomas, J. Azzi, and H. Wang, "Simple Constitutive Equations for Steel at High Temperature." Metall. Trans. A, 1992. 23A(March): p. 903-918.

47. Thomas, B.G., I.V. Samarasekera, and J.K. Brimacombe, "Comparison of Numerical Modeling Techniques for Complex, Two-Dimensional, Transient Heat Conduction Problems." Metall. Trans., 1984. 15B: p. 307-318.

48. Lemmon, E.C., "Multidimensional Integral Phase Change Approximations for Finite Element Conduction Codes,", in Numerical Methods in Heat Transfer, R. Lewis, Editor. 1981, John Wiley and Sons Ltd.: New York, NY. p. 201-213.

49. DuPont, T., G. Fairweather, and J. Johnson, "Three-level Galerkin Mehtods for Parabolic Equations." SIAM Journal of Numerical Analysis, 1974. 11: p. 392-410.

50. Forsythe, G. and C. Moler, "Computer Solution of Linear Algebraic Systems". 1967, Englewood Cliffs, NJ: Prentice Hall.

51. Mendelson, A., "Plasticity - Theory and Applications". 1983, Malabar, FL: R.E. Krieger Publishing. 213-215.

52. Fiaer, H.G. and A. Mo, "ALSPEN - A Mathematical Model for Thermal Stresses in DC-Cast Al Billets." Metall. Trans., 1990. 21B(6): p. 1049-1061.

53. Smelser, R.E. and O. Richmond. "Constitutive model effects on stresses and deformations in a solidifying circular cylinder," in Modeling of Casting and Welding Processes IV. 1988. Palm Coast, FL: The Minerals, Metals & Materials Society, Warrendale, PA.

54. Brown, S., K. Kim, and L. Anand, "An Internal Variable Constitutive Model for Hot Working of Metals." Int. J. Plast., 1989. 5(2): p. 95-130.

55. Anand, L., "Constitutive Equations for the Rate Dependent Deformation of Metals at Elevated Temperatures." Trans. ASME, J. Eng. Mat. and Tech., 1982. 104(Jan): p. 12-17.

56. Glowinski, R. and P.L.Tallee, "Augmented Lagrangian and Operator-Splitting Methods in Non-linear Mechanics, Studies in Applied Mathematics." SIAM, 1989. 9.

57. Lush, A.M., G. Weber, and L. Anand, "An Implicit Time-integration Procedure for A Set of Internal Variable Constitutive Equations for Isotropic Elastic-Viscoplasticity." Int. J. Plasticity, 1989. 5: p. 521-549.

58. Harste, K., A. Jablonka, and K. Schwerdtfeger. "Shrinkage and Formation of Mechanical Stresses during Solidification of Round Steel Strands," in 4th Int. Conf. on Continuous Casting. 1988. Centres de Recherches Metallurgiques and Verein Deutscher Eisenhuttenleute: Stahl und Eisen, Brussels.

59. Jablonka, A., K. Harste, and K. Schwerdtfeger, "Thermomechanical Properties of Iron and Iron-Carbon Alloys: Density and Thermal Contraction." Steel Research, 1991. 62(1): p. 24-33.

60. Jimbo, I. and A. Cramb, "The density of liquid iron-carbon alloys." Metall. Trans. B, 1993. 24B: p. 5-10.

61. Mizukami, H., K. Murakami, and Y. Miyashita, "Mechanical Properties of Continuously Cast Steels at High Temperatures." Tetsu-to-Hagane, 1977. 63(146): p. S 652.

62. Weiner, J.H. and B.A. Boley, "Elasto-Plastic Thermal Stresses in a Solidifying Body." J. Mech. Phys. Solids, 1963. 11: p. 145-154.

63. Wray, P.J., "Effect of Carbon Content on the Plastic Flow of Plain Carbon Steels at Elevated Temperatures." Metall. Trans. A, 1982. 13A(1): p. 125-134.

64. Maehara, Y., H. Tomono, and Y. Ohmori, "Stress Relaxation during Hot Deformation of Austenite." Trans. Iron Steel Inst. Jpn., 1987. 27: p. 499-505.

65. Liu, W., G.X. Wang, and E.F. Matthys, "Thermal Analysis and Measurement For a Molten Metal Drop Impacting On a Substrate: Cooling, Solidification and Heat Transfer Coefficient." Int. J. Heat Mass Transfer, 1995. 38: p. 1387-1395.

66. Todoroki, H., et al. "Evaluation of the Initiation of Solidification of Iron against a Water Cooled Copper Mold," in Electric Furnace Conference Proceedings. 1996. Dallas:

67. Mizukami, H., T. Suzuki, T. Umeda, and W. Kurz, "Initial stage of rapid solidification of 18-8 stainless steel." Mat. Sci. & Eng., 1993. A173: p. 363-366.

68. Dong, S., E. Niyama, K. Anzai, and N. Matsumoto, "Free Deformation of the Initial Solid Layer of Some Non-ferrous Alloys." 1995. .

69. Boley, B.A. and J.H. Weiner, "Theory of Thermal Stresses". 1960, John Wiley, Inc.

70. Clyne, T.W. and A. Garcia, "The Application of a New Soldification Heat Flow Model to Splat Cooling." Journal of Materials Science, 1981. 16: p. 1643-1653.

71. Poirier, D.R. and G.H. Geiger, "Transport Phenomena in Materials Processing". 1994, Warrendale, Pennsylvania: The Minearls, Metals & Materials Society. 306-310.

72. Thomas, B.G., B. Ho, and G. Li, University of Illinois at Urbana-Champaign, "CON1D User's Manual," (1994).

73. Nakai, K., et al., "Improvement of Surface Quality of Continuously Cast Slab by Reducing Heat Flux Density in Mould,", in Continuous Casting '85 Proceedings. 1985, Institute of Metals: London, UK. p. paper 71.

74. Wolf, M.M., "Mold Heat Transfer and Lubrication Control - Two Major Functions of Caster Productivity and Quality Assurance,", in PTD Conference Proceedings. 1995, Iron and Steel Society: Warrendale, PA. p. 99-117.

75. Brimacombe, J.K., F. Weinberg, and E.B. Hawbolt, "Formation of Longitudinal, Midface Cracks in Continuously-Cast Slabs." Metal. Trans. B, 1979. 10B: p. 279-292.

76. Yamanaka, A., K. Nakajima, and K. Okamura, "Critical Strain for Internal Crack Formation in Continuous Casting." Ironmaking Steelmaking, 1995. 22(6): p. 508-512.